Implantable Low-Noise Fiberless Optoelectrodes for Optogenetic Control of Distinct Neural Populations

by

Komal K. Kampasi

A dissertation submitted in partial fulfillment
of the requirements for the degree of
Doctor of Philosophy
(Biomedical Engineering)
in The University of Michigan
2017

Doctoral Committee:

Professor Euisik Yoon, Chair
Assistant Professor Cynthia A. Chestek
Assistant Research Scientist John P. Seymour
Professor Herbert G. Winful
Professor Emeritus Kensall D. Wise

Komal Kampasi

kkomal@umich.edu

ORCID ID: 0000-0002-3751-2398

Dedicated to my family.

Acknowledgments

As I am concluding my graduate school at University of Michigan, it takes me back to the dreams that I had arrived with six years ago. The most thriving of them was to be a part of the exemplary Michigan engineering community and to contribute to its innovations. I have been fortunate enough to realize my dream; I would like to take this opportunity to thank everyone who has made it possible.

First and foremost, I thank my advisor, Professor Euisik Yoon. I am extremely grateful to him for welcoming me into his research group in my third year and making my transition from Neural Engineering Lab to Yoon Lab as easy as possible. His mentoring inspired me to be creative, dynamic and to push myself beyond what I thought that I could do. He always gave me the freedom to explore new ideas, present at conferences and workshops and lead discussions and collaborations. These experiences have taught me how to be a better engineer and researcher while developing my overall professional skillset. I sincerely thank him for his continuous support and guidance.

I deeply acknowledge the contribution from my other dissertation committee members. Dr. John Seymour has helped me immensely in developing my research and analytical skills. From being an early mentor at Neural Engineering Lab to a co-advisor at Yoon Lab, his guidance and encouragement have been instrumental to my graduate career. I am indebted to Professor Herbert Winful for guiding me through fundamentals of optics and helping me integrate the knowledge in my thesis work. His passion for both

research and arts alike is truly inspiring. Professor Ken Wise has been an exceptional role model. His innovations in the field of MEMS and neurotechnology have inspired my research in many ways. It has been a privilege to be a part of his “Michigan probe” family and to be able to share ideas with him. Dr. Cindy Chestek has helped me understand the practical requirements of neural technology from both an engineer’s and neuroscientist’s perspective, I thank her for her time and valuable feedback. I have also gained valuable insights from our collaborators from multidisciplinary fields. Professor György Buzsáki, Dr. Eran Stark and other members of Buzsaki Lab at New York University have made significant contribution to my research work. Their enthusiasm and knowledge for implementing novel technologies has always been a guiding force for Michigan probe innovations. Other research collaborations with Dr. Gina Poe’s group at Michigan and Dr. Bryan McLaughlin’s team at Draper Labs have helped me broaden my knowledge and skillset.

The work described in this thesis would not have been complete without the support of the entire staff at Lurie Nanofabrication Facility. I highly appreciate the help from Brian Armstrong, Anthony Sebastian, Pillar Herrera-Fierro, Steven Sostrom and Nadine Wang on various tools and processes. My exceptional cleanroom mentors - Kyounghwan Na, John Seymour and Fan Wu have taught me intricacies of microfabrication. I thank John Nees for sharing his knowledge on optoelectronics and lasers and Kent Pruss for always willing to experiment at the machine shop. Chris Solis from Finetech has been a great help in setting up Finetech’s Lambda flipchipper bonder technology at Michigan, which was extensively used for device assembly in Chapter 5. I acknowledge the technical assistance from the staff at ULAM Pathology Department and

Microscopy and Imaging Lab in the immunohistology work presented in Chapter 6. I appreciate Meng Ting Chung's help with diffractive grating simulations in Appendix A. Lastly but not the least, I am thankful to all past and present members of Yoon group, especially the members of Advanced Neurotech group, for their active feedback on my research and continuous support; I will cherish the times that we spent together.

I would also like to thank the members of Dr. Daryl Kipke's Neural Engineering Lab who mentored me during early years of my PhD program. Daryl's enthusiasm for neurotechnology was contagious and got me excited to pursue research in this field. Azadeh Yazdan, Colin Stoetzner and Andre Snellings helped me to develop my research skills. I am thankful to all lab members including Paras Patel, Karen Schroeder and Amanda Perez for their academic and research mentorship and camaraderie.

I am grateful to the staff of Biomedical Engineering (BME) and Electrical Engineering and Computer Science (EECS) department at University of Michigan for their administrative support. I thank Rackham Graduate School for Rackham International Award and BME department for BME fellowship for providing full financial support during first half of my graduate studies. I acknowledge NIH BRAIN Initiative for funding major part of my research at Yoon Lab.

I extend my thanks to my wonderful friends who have made my stay at Ann Arbor truly memorable. To my friends - Deval Shah, Pratik Agarwal, Shaizeen Aga, Apeksha Shenoy, Rahul Jha, Girish Kulkarni, Yu-Ju Lin, John Seymour, Neel Desai, Santosh Telang, Vineet Raichur, thank you for all the fun activities and conversations that we enjoyed together. I also thank all my dancing friends at Leilah Belly Dancing, BollyFit and Michigan Argentine Tango for keeping the dancer within me alive and happy.

Finally, my deepest gratitude and most heartfelt thanks to my long-distance family - my grandparents, parents, cousins and their families and my friends for their constant love and support. A special mention to Megha Kampasi, Mikhil Bhosle, Vipin Kampasi, Shreya Pandita, Priyanka Sud, Deval Shah, Advitiya Sharma, Shanthan Pamulapatli, Amod Samant, and Pratik Agarwal; thank you for always lending a listening ear and a helping hand and visiting me often at Ann Arbor. Finally, and most importantly, I thank my Grandmom, Mom, Dad, Brother and Arpit. You have taught me how to work hard for something I am passionate about and to never ever, under any circumstance, give up. The physical distance has been hard but I have always felt your love, encouragement and pride by my side. I cannot thank you enough for it. Love you all.

Table of Contents

List of Figures

List of Tables

List of Appendices

Abstract

The mammalian brain is often compared to an electrical circuit, and its dynamics are governed by communication across different types of neural cells called neurons. To treat many neurological disorders like Alzheimer's and Parkinson's, which are characterized by inhibition or amplification of neural activity in a particular region or lack of communication between different regions of the brain, there is a need to troubleshoot neural networks at cellular or local circuit level.

Though optogenetics has proven to be the most powerful means of cell-type specific neural circuit control in recent years, a long-standing question in neuroscience has been whether it is possible to achieve independent control of two or more distinct neural populations simultaneously. In this work, we introduce a novel implantable optoelectrode that can, for the first time, manipulate more than one neuron type at a single site, independently and simultaneously. The optoelectrode can deliver multi-color light from a scalable optical waveguide mixer at precise spatial locations. We report design, micro-fabrication and optoelectronic packaging of a fiber-less, multicolor optoelectrode that is also modular and minimally invasive. Our technology addresses the limitations of all available optoelectrodes, which often rely on mechanically invasive and bulky devices and/or can control only one neuron type via mono-color light at a single site; and hence have limited function and control.

We present, for the first time, the integration of coupling lensing mechanism for

a neural optoelectrode design. The compact four-shank optoelectrode design consists of 7 μm-thick and 30 μm-wide dielectric optical waveguide mixers, which are monolithically integrated on a 22 μm-thick four-shank silicon neural probe. The waveguide mixers are coupled to eight side-emitting injection laser diodes (ILDs) via eight gradient-index (GRIN) lenses assembled on the probe backend. GRINs enable efficient optical coupling with large alignment tolerance to provide wide optical power range (10 to 3000 mW/mm^2 irradiance) at stimulation ports. They also keep thermal dissipation and electromagnetic interference generated by light sources sufficiently far from the sensitive neural signals, allowing thermal and electrical noise management on a multilayer printed circuit board.

We demonstrate device validation and verification to study the densely populated CA1 pyramidal layer of rodent hippocampus in both anesthetized and awake animals. The packaged devices were used to manipulate variety of multi-opsin preparations *in vivo* expressing different combinations of Channelrhodopsin-2, Archaerhodopsin and ChrimsonR in pyramidal cells and parvalbumin interneuron cells. We show effective stimulation and recording of neural spikes with less than 100 μV stimulation-locked transients on the recording channels, demonstrating potential use of this technology in the functional dissection of neural circuits.

Finally, we discuss diagnostic techniques and studies to better understand the device-tissue interaction that can help in engineering of next-generation reliable neural interfaces.

Chapter 1

Exploring the Brain

1.1 Brain organization and function

As it was succinctly put by the British philosopher, Emerson Pugh, “If the human brain were so simple that we could understand it, we would be so simple that we couldn’t.”

The brain is what makes us who we are. It is responsible for each individual's personality, memories, movements, and how we sense the world. But as central as the brain is to our existence, we understand very little about how it actually works. Understanding human brain’s mind-boggling complexity is not easy. Weighing at only 1.5 kilograms, it consists of some 100 billion nerve cells, each with 1,000 connections that not only put together thoughts and highly coordinated physical actions but regulate our unconscious body processes, such as digestion and breathing. The basic unit of brain is nerve cell called neuron. The neurons transmit and gather electrochemical signals via synaptic connections connecting a network of millions of neurons (**Figure 1-1a**) responsible for a single function. **Figure 1-1b** captures the essence of one such signal, a synaptic millisecond, with a labyrinth of neurons in the background.

Here, a pre-synaptic neuron is captured as it prepares to transmit neurotransmitters to its post-synaptic target. As the neurotransmitters bind to the ion

channels on the target neuron, they open its ion channels giving rise to an action potential (**Figure 1-2a**). Action potential marks electrical depolarization of a nerve membrane and is responsible for flow of information from one neuron to another.

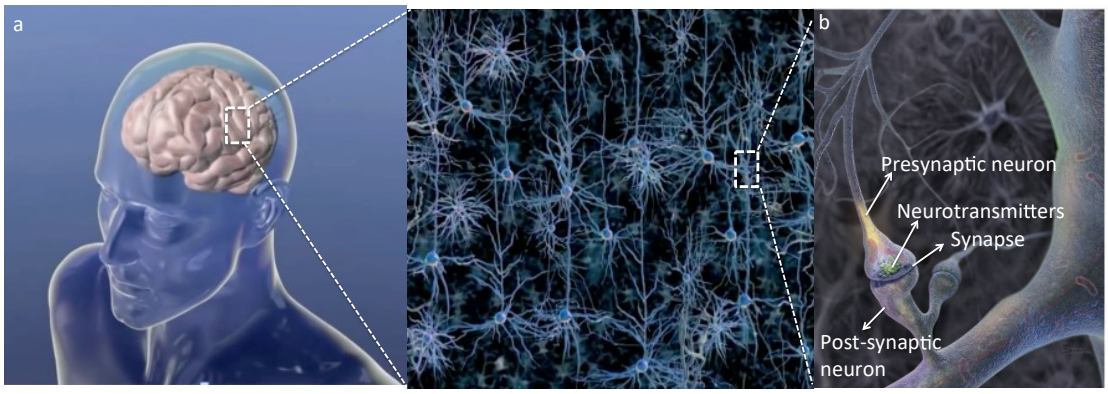

Figure 1-1. (a) Diagrammatic inside view of the human brain showing highly dense network of different neuron types. [Courtesy: Ed Boyden, MIT Media Lab] (b) A synaptic connection between two neurons that facilitates the flow of information between neurons in the form of action potentials [1].

However, the generation of action potential is not as straightforward as each neuron connects with numerous other neurons, often receiving multiple impulses, not one, from them. These impulses can be excitatory postsynaptic potential (EPSP) from excitatory group of neurons or inhibitory postsynaptic potential (IPSP) from inhibitory group of neurons (**Figure 1-2b**). IPSPs can cancel out EPSPs and vice versa; and the net change in postsynaptic membrane voltage determines whether the postsynaptic cell has reached its threshold of excitation needed to fire an action potential. If the neuron receives as many inhibitory as excitatory impulses, the inhibition cancels out the excitation and the nerve impulse will stop there. Hence the resulting action potential is the temporal or spatial summation of these impulses at the axon hillock. Both excitatory (e.g.: pyramidal) and inhibitory (e.g.: interneurons) neurons, together with synaptic summation and the threshold for excitation, play a

crucial role in transmitting important information and filtering out random noise. The amount of synchrony required for effective transmission depends on the strength and the delay between the excitatory and the inhibitory signals. These neural signals when transmitted by groups of nerve cells in recurrent networks, from layer to layer and structure to structure; facilitate co-ordination between different parts of the brain and their function.

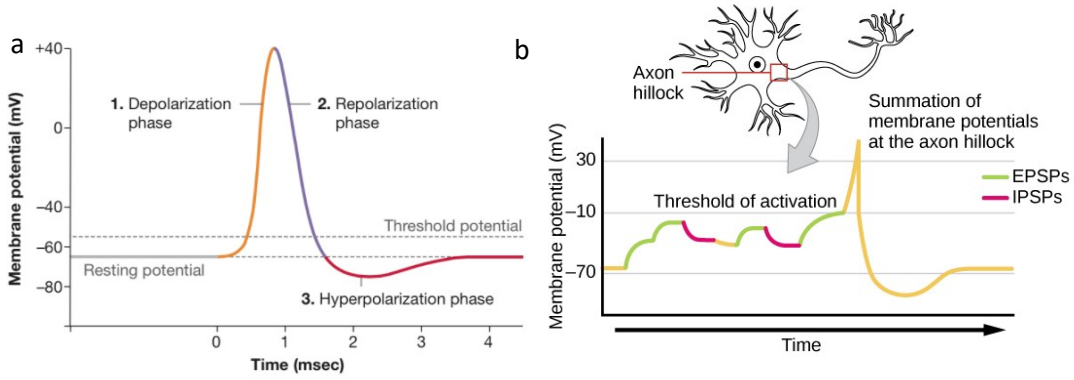

Figure 1-2. (a) Plot of a typical action potential showing various stages as the potential passes a point on a cell membrane. The membrane potential always rests at -70 mV until a stimulus is applied, following which the membrane potential first rapidly rises to a peak potential of +40 mV, then drops and overshoots and finally settles back down. (b) A single neuron can receive both excitatory and inhibitory inputs from multiple neurons, resulting in local membrane depolarization (EPSP input) and hyperpolarization (IPSP input). A neuron only fires when the summation of potentials crosses the threshold for excitation [2].

1.2 Neuroscience research goals

Last few decades have been incredible for advances in neuroscience that help us better understand the structure and function of the brain. Apart from satisfying our curiosity, the major motivation behind neuroscience research is to understand and treat brain circuits that go awry leading to mental disorders. Brain disorders represent the biggest unmet medical need, with many disorders being untreatable, and most treatments presenting serious side effects. The two major research fields in

neuroscience, clinical neuroscience and systems neuroscience, are being explored in parallel by researchers. While clinical neuroscience aims at developing novel treatments for brain disorders, systems neuroscience studies neural network organization and function.

1.2.1 Clinical neuroscience

Clinical neuroscience focuses more on the fundamental mechanisms that underlie brain abnormalities and developing new ways of diagnosing such disorders. The focus of much of the current research in clinical neuroscience is to develop reliable chronic brain implants. The goal is to establish a long-term biomedical neural interface circumventing areas in the brain that have become dysfunctional after a stroke, head injuries or diseases such as Parkinson's or Alzheimer's. Over the last few decades, electrophysiological recording and electrical stimulation techniques have tremendously improved our understanding of brain structure and function [3]–[7]. Technologies are being continuously developed to better understand brain function and for rehabilitation of nervous system injuries. Brain Machine Interfaces (BMIs) are being widely researched to actuate prosthetic limbs in patients suffering from paraplegia or quadripalegia [8]–[10]. In parallel, many pharmaceutical drugs are being discovered and tested to treat mental illnesses like schizophrenia, epilepsy, depression, anxiety and psychosis [11]–[13].

1.2.2 Systems neuroscience

Systems neuroscience studies the function of neural circuits and systems, encompassing a number of areas of study concerned with how nerve cells behave when connected together to form neural networks. The scientists around the globe

have taken on the challenge to understand brain function from its intricate anatomy and structure. Rather than attempting to fully reconstruct the whole brain or a particular brain region, the solution seems to lie in realistic computational modeling of parts of the brain. This approach has inspired large multidisciplinary projects, and has challenged scientists from all fields to rethink some of the most fundamental aspects of their work and to innovate. Scientists are discovering design principles for novel neuromodulation therapies and inventing a variety of genetic, molecular, pharmacological, optical, and electrical tools to correct neural circuits that go awry within the brain. Classical modulation methods such as deep brain stimulation (DBS) and novel neurotechnologies are being used alike to modulate the function of neural circuits establish causal links between neural dynamics and behavior.

1.3 Optogenetics

1.3.1 Background

While the exploration of brain networks is moving ahead, a relatively new toolset called optogenetics has come forward to enable precise identification and manipulation of circuit components. In 1999, Francis Crick suggested that the major challenge facing neuroscience was the need to control one type of cell in the brain while leaving others unaltered [14]. As electrodes cannot be used to precisely target defined cells and drugs act much too slowly, Crick later speculated that light might have the properties to serve as a control tool. But it was not until 2005 that a distinct single-component approach involving microbial opsin genes was developed into the controlled technology of optoegentics as it is known today.

Understanding how different kinds of neuron in the brain work together to

implement sensations, feelings, thoughts, and movements, and how deficits in specific kinds of neuron result in brain diseases, has long been a priority in basic and clinical neuroscience. “Optogenetic” tools are genetically encoded molecules that, when targeted to specific neurons in the brain, enable their activity to be driven or silenced by light. These molecules are microbial opsins, transmembrane proteins adapted from organisms found throughout the world, which react to light by transporting ions across the lipid membranes of cells in which they are genetically expressed. The first of these neuronal switches used were channelrhodopsin-2 (ChR2) [15], [16]. When expressed in a neuron and exposed to blue light, this nonselective cation channel immediately depolarizes the neuron and triggers a spike (**Figure 1-3**). Several variants of ChR2 have been developed. ChETA (channelrhodopsin-2 mutant E12ET) mutants were engineered to spike neurons at frequencies greater than 40 Hz [17]. The step function opsins, or SFO variants, are slower versions of ChR2 that can induce prolonged stable excitable states in neurons upon exposure to blue light and then be reversed upon exposure to green light [18]. Channelrhodopsin-1 (VChR1) acts similarly to ChR2 but is activated by red-shifted light [19]. Light stimulation of halorhodopsin (NpHR), a chloride pump, silences (hyperpolarizes) neurons in response to yellow light [20] (**Figure 1-3**). Recent variants (eNpHR2.0 and eNpHR3.0) exhibit improved membrane targeting in mammalian cells [21]. Light-driven proton pumps such as archaerhodopsin-3 (Arch), Mac, bacteriorhodopsin (eBR) and rhodopsin-3 (GtR3) can also be used to hyperpolarize neurons and block signaling [21]–[23] (**Figure 1-3**). **Figure 1-4** shows the diagrammatic representation of blue light modulating a group of genetically-modified basket cells in a given brain

region. These tools are enabling the causal assessment of the roles that different sets of neurons play within neural circuits, and are accordingly being used to reveal how

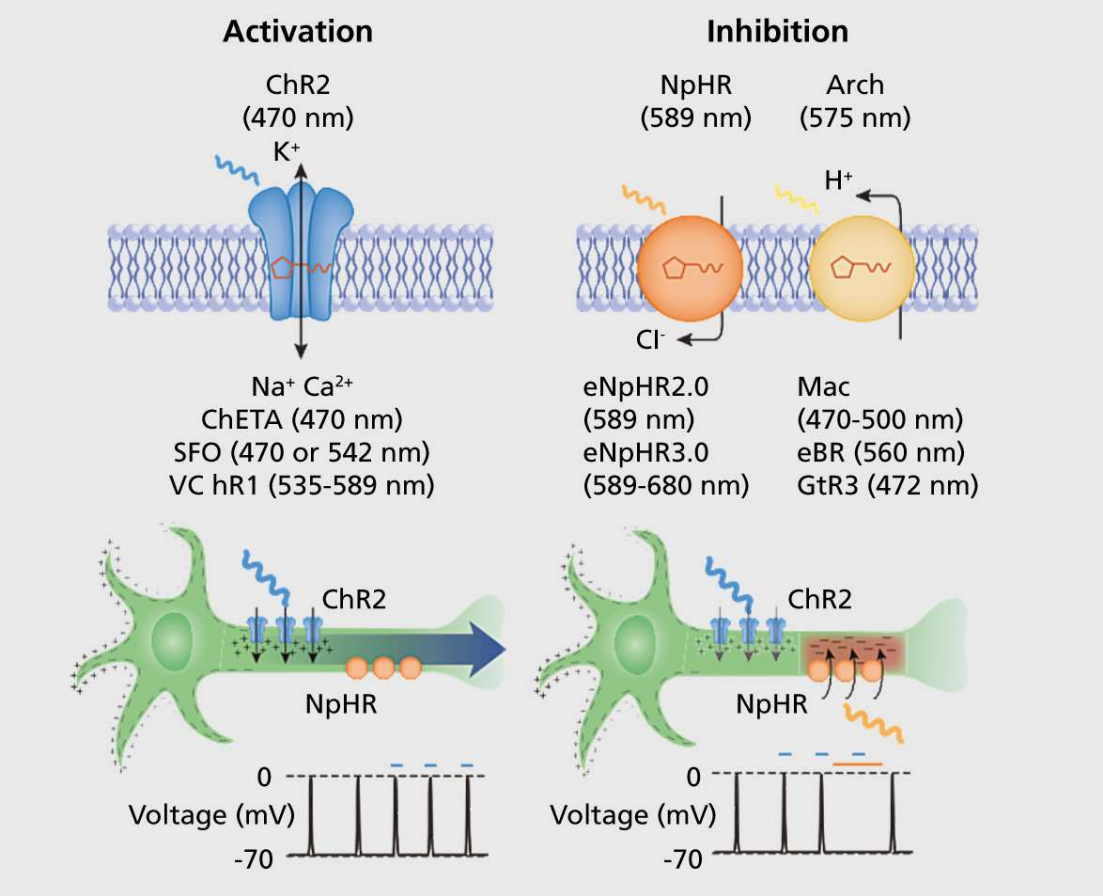

Figure 1-3. Optogenetic tools for modulating membrane voltage potential. Stimulating the neurons expressing the nonselective cation channel Channelrhodopsin-2 (ChR2) using blue light depolarizes the neuron and triggers an action potential. Light stimulation of halorhodopsin (NpHR) variants, which are chloride pumps, hyperpolarizes neurons and inhibits spikes in response to yellow light. Light-driven proton pumps such as archaerhodopsin-3 (Arch), Mac, bacteriorhodopsin (eBR), and rhodopsin-3 (GtR3) can also be used to hyperpolarize neurons and block signaling. Ca2+, calcium; ChETA, channelrhodopsin-2 mutant E12ET; mV, millivolts; Na+, sodium; nm, nanometer; SFO, step-function opsin; VChR1, Volvox-derived channelrhodopsin-1 [24].

different sets of neurons contribute to the emergent computational and behavioral functions of the brain. These tools are also being explored as components of prototype neural control prosthetics capable of correcting neural circuit computations that skew off in brain disorders.

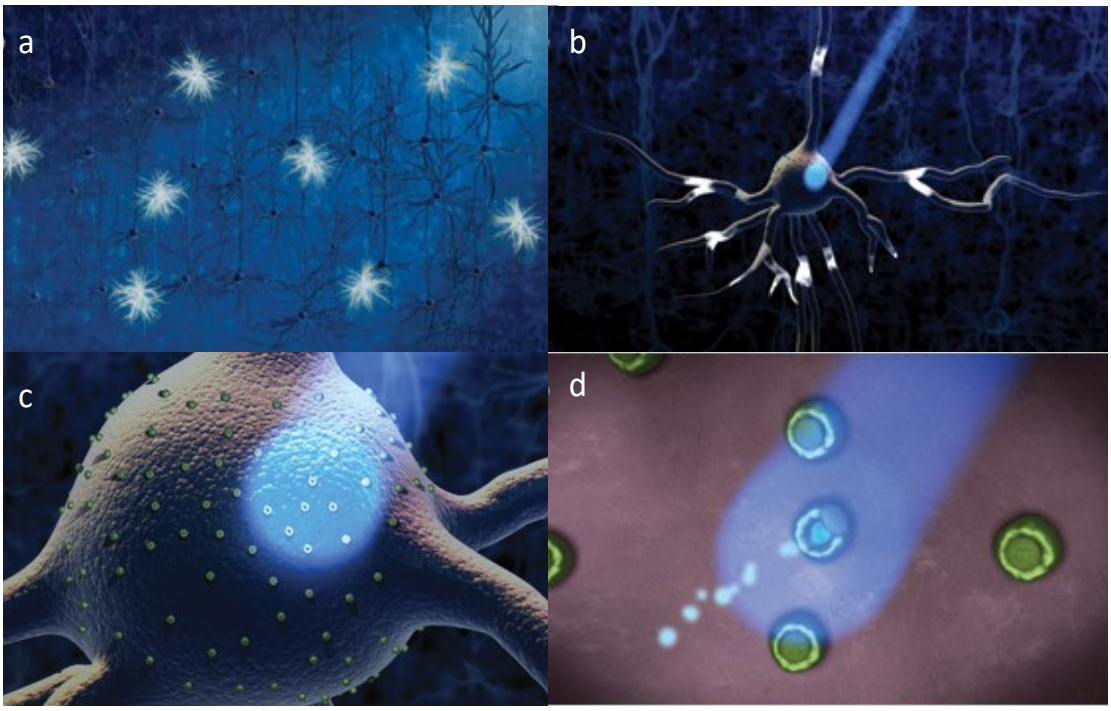

Figure 1-4. (a) Network level to (d) ion-channel level diagrammatic view of how blue light modulates a genetically modified neuron expressing an opsin called Channelrhodopsin-2 (ChR2) in its ion channels (green dots). A brief pulse of light (ms long) opens ChR2-expressing channels, causing an influx of positively charged ions and an action potential. This makes the cells expressing ChR2 fire (white flashes in a and b) while not modulating the activity of other cells [Courtesy: Ed Boyden, MIT McGovern Institute].

1.3.2 Major advances

The emerging field of optogenetics is allowing scientists to control and map brain circuits with cell-type specificity at high spatial and temporal precision [15], [25], [26]. Continuously developing novel opsins display a wide range of spectral sensitivity, allowing precision interrogation of neural circuit computation [27], [28]. Opsins can be used to activate (depolarize) or silence (hyperpolarize) the targeted neurons, with the aim of understanding neural computation [29]–[31] (**Figure 1-5**). For example, Channelrhodopsin-2 (ChR2), responds to ~470 nm light and depolarizes the targeted cells [15], [32], [33]. Other opsins like Archaerhodopsin (Arch) [22], [23]

and Halorhodopsins (NpHr) [34], [35], when illuminated with ~590 nm light, induce hyperpolarization. Multiple opsins can be expressed in the same cell [34], [21] or in different cell types [31], [36], [37] to specifically target and manipulate local circuit elements.

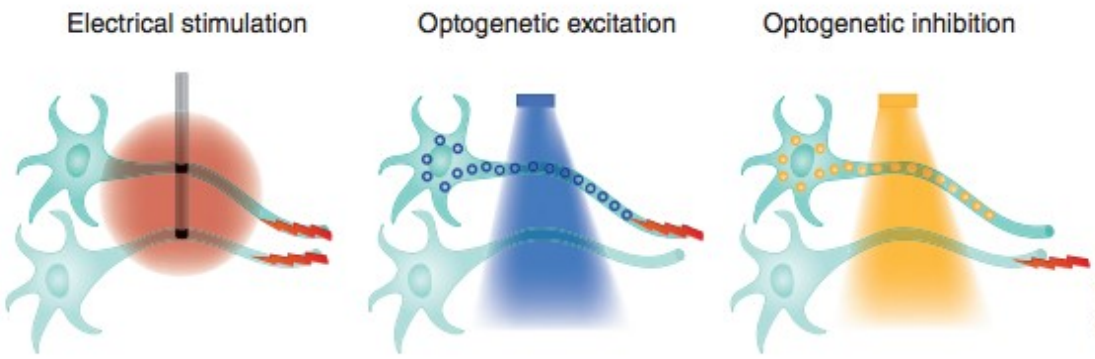

Figure 1-5. The comparison of electrical stimulation with optogenetics. Optogenetics can be used to modulate different neuron types with different colors of light, achieving cell specificity that is not possible with electrical stimulation. [25]

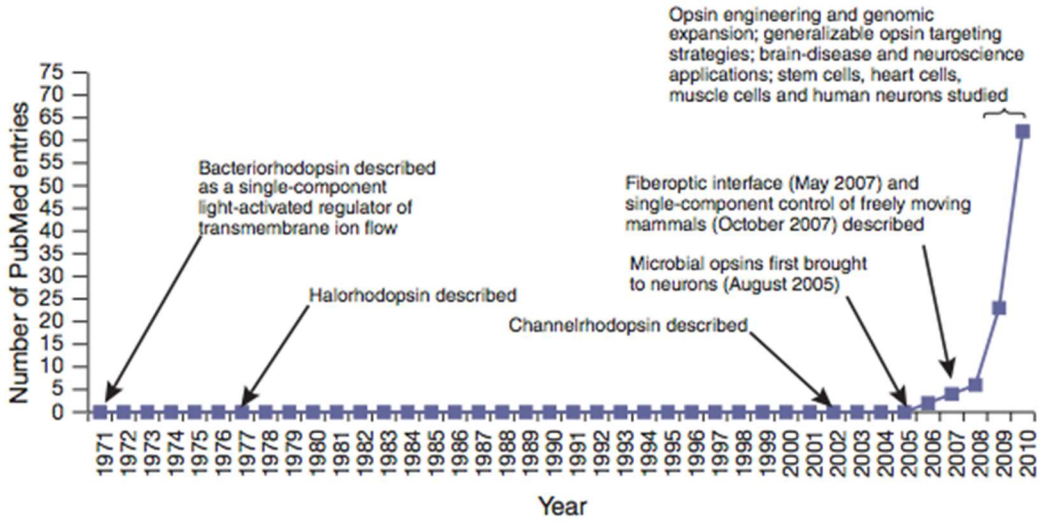

Figure 1-6. Evolving field of optogenetics since last few decades [25]. Optogenetics was named as the Nature Method of the Year in 2010.

The advances in this twelve-year-old field (**Figure 1-6)** have solved controversies in molecular neural biology that have been going on for many years.

Introducing these proteins into cultured cells or the brains of live animals allows investigation of the structure and function of neural networks (**Figure 1-7**). What excites neuroscientists about optogenetics is control over defined events within

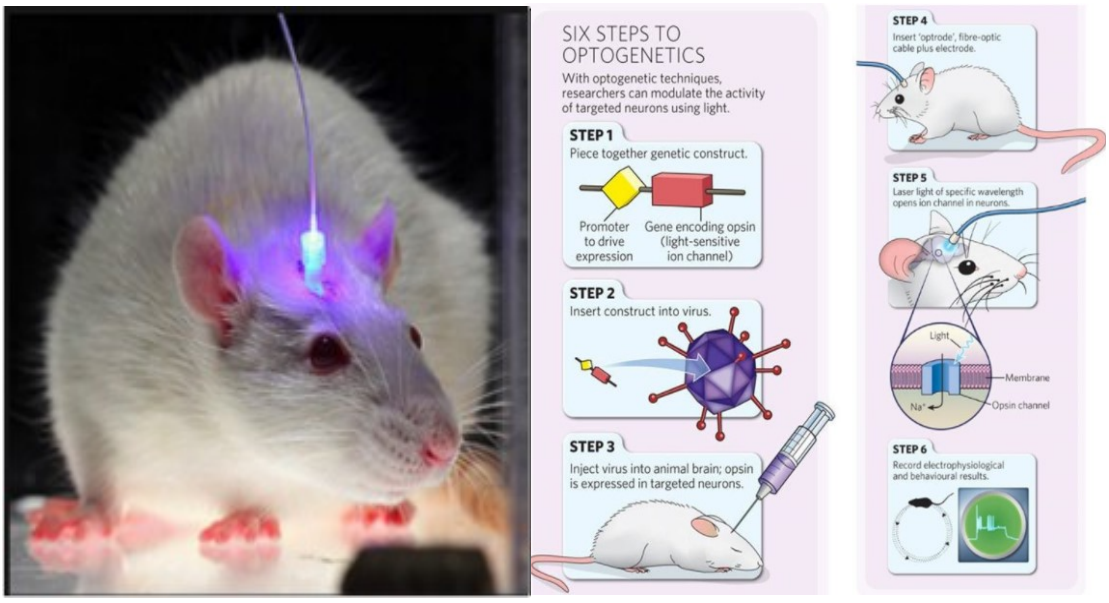

Figure 1-7. Step-wise guide of optogenetics technique. [38]

defined cell types at defined times—a level of precision that is most likely crucial to biological understanding even beyond neuroscience. The significance of any event in a cell has full meaning only in the context of the other events occurring around it in the rest of the tissue, the whole organism or even the larger environment. Even a shift of a few milliseconds in the timing of a neuron's firing, for example, can sometimes completely reverse the effect of its signal on the rest of the nervous system.

1.3.3 Applications

Optogenetics has two major advantages for neuronal circuit analysis. First, it allows specificity for the identification of genetically targeted cell types, whose activity patterns can then be correlated with both behavior and patterns of brain activity. Second, their targeted activations can alter circuit performance possibly at

single cell resolution and, therefore, facilitate to formulate causal hypotheses about their role in computation and behavior. The currently available optogenetic actuators allow for the accurate temporal control, either excitation or inhibition with millisecond precision. Therefore, experiments can now be devised where the light can be used as the ultimate intervention tool to induce or inhibit a particular oscillatory event in the brain or a particular behavior. This kind of approach can be specifically applied to study distinct high frequency oscillatory events in a part of a brain called hippocampus. Sharp waves and ripple complexes (SWR) in mammalian brain are thought to play an important role in memory formation, memory consolidation and in spatial memory that enables navigation. These events can be readily detected by following the oscillatory cycles of the on-line recorded local field potential. In this way, the onset of the event can be used as a trigger signal for a light flash that is guided back into the hippocampus to inhibit neurons specifically during the SWRs and also to optogenetically inhibit the oscillation itself. These kinds of "closed-loop" experiments are useful to study SWR complexes and their role in memory.

1.4 Summary and outline

In this chapter, we explained the basics of information flow within brain. We discussed major research goals of neuroscience, introduced the revolutionary technique of Optogenetics and discussed its vast potential to contribute to brain science. In Chapter 2, we provide a literature review of the neural interfacing tools starting from their early development as electrical interfaces to more recent optoelectrodes. As optogenetics is gaining momentum, optoelectrode technologies are growing at a fast pace. In recent years, many novel technologies have been proposed

for building robust electrical-optical interfacing with the brain. However, the available optoelectrodes are still incapable of manipulating more than one neuron type independently at precise spatial locations in brain. This capability is fundamental to our understanding of how neural circuits perform at circuit level to govern computation. In Chapter 2, we discuss more about the limitations of available technologies and explore design solutions for a perfect optoelectrode for local neural circuit analysis. In Chapter 3, we introduce a novel optoelectrode that can serve as a fundamental tool to manipulate distinct neural populations at precise waveguide ports, addressing the challenges of conventional optical stimulation technologies. Chapter 4 discusses the issue of noise artifacts in optoelectrodes. We present system-level electrical design strategies to enable low-noise neural recording. In Chapter 5, we demonstrate design and implementation of a fully implantable, multi-shank, low-noise optoelectrode. Chapter 6 discusses possible design solutions to mitigate and detect neural interface failure *in vivo*. Chapter 7 presents summary of the work presented in this thesis and suggests the direction of future work.

References

[1] C. Gramling, "The synapse revealed," *Science*, vol. 309, no. 5743, pp. 1990–1990, 2005.

[2] Openstax, "How neurons communicate," 2013 [Online]. Available: https://cnx.org/contents/cs_Pb-GW@8/How-Neurons-Communicate.

[3] A. Hodgkin, A. Huxley, and B. Katz, "Measurement of current-voltage relations in the membrane of the giant axon of Loligo," *J. Physiol.*, vol. 116, no. 4, pp. 424–48, 1952.

[4] O. P. Hamill, A. Marty, E. Neher, B. Sakmann, and F. J. Sigworth, "Improved patch-clamp techniques for high-resolution current recording from cells and cell-free membrane patches," *Pflugers Arch. Eur. J. Physiol.*, vol. 391, pp. 85–100, 1981.

[5] M. G. Blanton, J. J. Lo Turco, and A. R. Kriegstein, "Whole cell recording from neurons in slices of reptilian and mammalian cerebral cortex," *J. Neurosci. Methods*, vol. 30, pp. 203–210, 1989.

[6] Y. Jimbo and A. Kawana, "Electrical stimulation and recording from cultured neurons using a planar electrode array," *Bioelectrochemistry Bioenerg.*, vol. 29, pp. 193–204, 1992.

[7] N. K. Logothetis, M. Augath, Y. Murayama, A. Rauch, F. Sultan, J. Goense, A. Oeltermann, and H. Merkle, "The effects of electrical microstimulation on cortical signal propagation.," *Nat. Neurosci.*, vol. 13, pp. 1283–1291, 2010.

[8] L. R. Hochberg, M. D. Serruya, G. M. Friehs, J. A. Mukand, M. Saleh, A. H. Caplan, A. Branner, D. Chen, R. D. Penn, and J. P. Donoghue, "Neuronal ensemble control of prosthetic devices by a human with tetraplegia," *Nature*, vol. 442, no. 7099, pp. 164–71, 2006.

[9] L. R. Hochberg, D. Bacher, B. Jarosiewicz, N. Y. Masse, J. D. Simeral, J. Vogel, S. Haddadin, J. Liu, S. S. Cash, P. van der Smagt, and J. P. Donoghue, "Reach and grasp by people with tetraplegia using a neurally controlled robotic arm," *Nature*, vol. 485, no. 7398, pp. 372–375, 2012.

[10] M. Velliste, S. Perel, M. C. Spalding, a S. Whitford, and a B. Schwartz, "Cortical control of a robotic arm for self-feeding," *Nature*, vol. 453, no. June, pp. 1098–1101, 2008.

[11] L. S., C. A., S. G., S. L., R. F., O. D., L. C., G. J., H. J., and B. C., "Multiple-treatments meta-analysis on the efficacy, acceptability and tolerability of 15 antipsychotics drugs in schizophrenia," *Schizophrenia Research*, vol. 136. p. S75, 2012.

[12] D. Schmidt and S. C. Schachter, “Drug treatment of epilepsy in adults,” *BMJ*, vol. 348, p. g254, 2014.

[13] R. S. Doody, R. G. Thomas, M. Farlow, T. Iwatsubo, B. Vellas, S. Joffe, K. Kieburtz, R. Raman, X. Sun, P. S. Aisen, E. Siemers, H. Liu-Seifert, and R. Mohs, “Phase 3 trials of solanezumab for mild-to-moderate Alzheimer’s disease.,” *N. Engl. J. Med.*, vol. 370, no. 4, pp. 311–21, 2014.

[14] F. Crick, “The impact of molecular biology on neuroscience.,” *Philos. Trans. R. Soc. Lond. B. Biol. Sci.*, vol. 354, no. 1392, pp. 2021–5, 1999.

[15] E. S. Boyden, F. Zhang, E. Bamberg, G. Nagel, and K. Deisseroth, “Millisecond-timescale, genetically targeted optical control of neural activity.,” *Nat. Neurosci.*, vol. 8, no. 9, pp. 1263–8, Sep. 2005.

[16] G. Nagel, T. Szellas, W. Huhn, S. Kateriya, N. Adeishvili, P. Berthold, D. Ollig, P. Hegemann, and E. Bamberg, “Channelrhodopsin-2, a directly light-gated cation-selective membrane channel.,” *Proc. Natl. Acad. Sci. U. S. A.*, vol. 100, no. 24, pp. 13940–5, 2003.

[17] L. A. Gunaydin, O. Yizhar, A. Berndt, V. S. Sohal, K. Deisseroth, and P. Hegemann, “Ultrafast optogenetic control.,” *Nat. Neurosci.*, vol. 13, no. 3, pp. 387–392, Mar. 2010.

[18] I. Diester, M. T. Kaufman, M. Mogri, R. Pashaie, W. Goo, O. Yizhar, C. Ramakrishnan, K. Deisseroth, and K. V Shenoy, “An optogenetic toolbox designed for primates,” *Nat. Neurosci.*, vol. 14, no. 3, pp. 387–397, 2011.

[19] F. Zhang, M. Prigge, F. Beyrière, S. P. Tsunoda, J. Mattis, O. Yizhar, P. Hegemann, and K. Deisseroth, “Red-shifted optogenetic excitation: a tool for fast neural control derived from Volvox carteri.,” *Nat. Neurosci.*, vol. 11, no. 6, pp. 631–3, 2008.

[20] V. Gradinaru, K. R. Thompson, and K. Deisseroth, “eNpHR: A Natronomonas halorhodopsin enhanced for optogenetic applications,” *Brain Cell Biol.*, vol. 36, no. 1–4, pp. 129–139, Aug. 2008.

[21] V. Gradinaru, F. Zhang, C. Ramakrishnan, J. Mattis, R. Prakash, I. Diester, I. Goshen, K. R. Thompson, and K. Deisseroth, “Molecular and Cellular Approaches for Diversifying and Extending Optogenetics,” *Cell*, vol. 141, no. 1, pp. 154–165, 2010.

[22] B. Y. Chow, X. Han, A. S. Dobry, X. Qian, A. S. Chuong, M. Li, M. A. Henninger, G. M. Belfort, Y. Lin, P. E. Monahan, and E. S. Boyden, “High-performance genetically targetable optical neural silencing by light-driven proton pumps.,” *Nature*, vol. 463, no. 7277, pp. 98–102, Jan. 2010.

[23] X. Han, B. Y. Chow, H. Zhou, N. C. Klapoetke, A. Chuong, R. Rajimehr, A.

Yang, M. V Baratta, J. Winkle, R. Desimone, and E. S. Boyden, “A high-light sensitivity optical neural silencer: development and application to optogenetic control of non-human primate cortex.,” *Front. Syst. Neurosci.*, vol. 5, pp. 1–8, 2011.

[24] E. Pastrana, “Optogenetics: controlling cell function with light,” *Nat. Methods*, vol. 8, no. 1, pp. 24–25, 2011.

[25] K. Deisseroth, “Optogenetics.,” *Nat. Methods*, vol. 8, no. 1, pp. 26–9, Jan. 2011.

[26] L. Madisen, T. Mao, H. Koch, J. Zhuo, A. Berenyi, S. Fujisawa, Y.-W. A. Hsu, A. J. Garcia, X. Gu, S. Zanella, J. Kidney, H. Gu, Y. Mao, B. M. Hooks, E. S. Boyden, G. Buzsáki, J. M. Ramirez, A. R. Jones, K. Svoboda, X. Han, E. E. Turner, and H. Zeng, “A toolbox of Cre-dependent optogenetic transgenic mice for light-induced activation and silencing.,” *Nat. Neurosci.*, vol. 15, no. 5, pp. 793–802, May 2012.

[27] N. C. Klapoetke, Y. Murata, S. S. Kim, S. R. Pulver, A. Birdsey-benson, Y. K. Cho, T. K. Morimoto, E. J. Carpenter, Z. Tian, J. Wang, Y. Xie, Z. Yan, Y. Zhang, B. Y. Chow, B. Surek, M. Melkonian, V. Jayaraman, M. Constantine-paton, G. K. Wong, E. S. Boyden, S. N. Group, C. Sciences, and C. Biocenter, “Independent Optical Excitation of Distinct Neural Populations,” vol. 11, no. 3, pp. 338–346, 2014.

[28] G. Buzsáki, E. Stark, A. Berényi, D. Khodagholy, D. R. Kipke, E. Yoon, and K. D. Wise, “Tools for probing local circuits: High-density silicon probes combined with optogenetics,” *Neuron*, vol. 86, no. 1, pp. 92–105, 2015.

[29] S.-H. Lee, A. C. Kwan, S. Zhang, V. Phoumthipphavong, J. G. Flannery, S. C. Masmanidis, H. Taniguchi, Z. J. Huang, F. Zhang, E. S. Boyden, K. Deisseroth, and Y. Dan, “Activation of specific interneurons improves V1 feature selectivity and visual perception,” *Nature*, vol. 488, no. 7411. pp. 379–383, 2012.

[30] C. K. Pfeffer, M. Xue, M. He, Z. J. Huang, and M. Scanziani, “Inhibition of inhibition in visual cortex: the logic of connections between molecularly distinct interneurons.,” *Nat. Neurosci.*, vol. 16, no. 8, pp. 1068–76, 2013.

[31] E. Stark, L. Roux, R. Eichler, Y. Senzai, S. Royer, and G. Buzsáki, “Pyramidal cell-interneuron interactions underlie hippocampal ripple oscillations,” *Neuron*, vol. 83, no. 2, pp. 467–480, 2014.

[32] G. Nagel, M. Brauner, J. F. Liewald, N. Adeishvili, E. Bamberg, and A. Gottschalk, “Light activation of Channelrhodopsin-2 in excitable cells of caenorhabditis elegans triggers rapid behavioral responses,” *Curr. Biol.*, vol. 15, no. 24, pp. 2279–2284, 2005.

[33] T. Ishizuka, M. Kakuda, R. Araki, and H. Yawo, “Kinetic evaluation of photosensitivity in genetically engineered neurons expressing green algae light-

gated channels," *Neurosci. Res.*, vol. 54, no. 2, pp. 85–94, 2006.

[34] X. Han and E. S. Boyden, "Multilpe-color optical activation, silencing, and desynchronization of neural activity, with single-spike temporal resolution," *PLoS One*, vol. 2, no. 3, 2007.

[35] F. Zhang, L.-P. Wang, M. Brauner, J. F. Liewald, K. Kay, N. Watzke, P. G. Wood, E. Bamberg, G. Nagel, A. Gottschalk, and K. Deisseroth, "Multimodal fast optical interrogation of neural circuitry.," *Nature*, vol. 446, no. 7136, pp. 633–9, 2007.

[36] V. S. Sohal, F. Zhang, O. Yizhar, and K. Deisseroth, "Parvalbumin neurons and gamma rhythms enhance cortical circuit performance.," *Nature*, vol. 459, no. 7247, pp. 698–702, 2009.

[37] O. Yizhar, L. E. Fenno, M. Prigge, F. Schneider, T. J. Davidson, D. J. O'Shea, V. S. Sohal, I. Goshen, J. Finkelstein, J. T. Paz, K. Stehfest, R. Fudim, C. Ramakrishnan, J. R. Huguenard, P. Hegemann, and K. Deisseroth, "Neocortical excitation/inhibition balance in information processing and social dysfunction.," *Nature*, vol. 477, no. 7363, pp. 171–178, 2011.

[38] L. Buchen, "Neuroscience: Illuminating the brain.," *Nature*, vol. 465, no. 7294, pp. 26–28, 2010.

Chapter 2

Neurotechnology for Neuroscience

2.1 Introduction

Designing neurotechnology is difficult because of the complex properties of the brain: its inaccessibility, heterogeneity, fragility, anatomical richness, and high speed of operation. Many non-invasive and invasive neural interface technologies have been

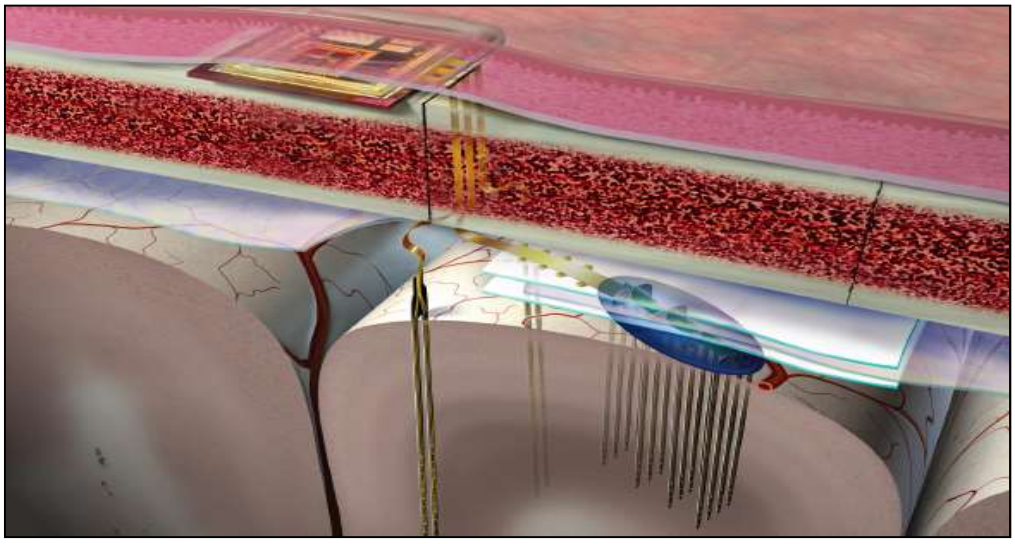

Figure 2-1. A neural microsystem consisting of 2-D/3-D arrays of cortically implanted penetrating electrodes [6].

developed over the last few decades to help advance our understanding of brain circuits. Electroencephalography (EEG) employs surface electrodes on scalp to sense neuronal signal changes associated with brain disorders like epilepsy and depression [1], [2]. Electrocorticography (ECoG) is more invasive than EEG and involves

placement of electrodes on brain surface. As a result of its proximity to brain surface, ECoG signals are less noisy with higher spatial resolution [3], [4]. Penetrating electrodes (**Figure 2-1**) are implanted deep inside the brain regions and offer the best insight into neuron-to-neuron interactions [5]–[7]. These offer highest spatial resolution offering microelectrode designs with smallest sizes. Early microelectrode wires are still widely used owing to their simple designs, easy availability, low cost and ability to be arranged in multiple 3-D geometries [5], [8]. However, the tetrode pitch limits the electrode density of such designs. In recent decades, advanced microelectromechanical systems (MEMS) technologies have enabled the design of

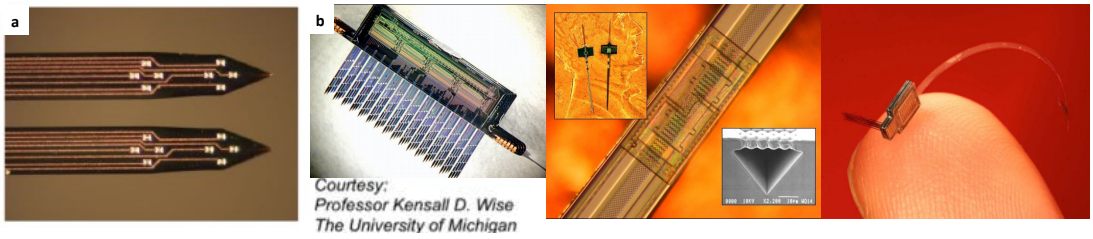

Figure 2-2. (a) Planar Michigan probe shanks with patterned electrodes. (b) Development of Michigan probes over the last decade [6], [9], [10].

penetrating electrodes with micron/sub-micron scale features. Michigan probe technology, pioneered by Kensall Wise, is continuously advancing the toolset for brain mapping. Many novel electrical probe designs with high-density recording have been developed by Wise group in the past [6], [9]–[11] (**Figure 2-2)**. Michigan probe has a planar structure with an array of stimulating/recording electrodes photo-lithographically defined on the pointed probe tip. The design can be scaled up to have high-density electrodes on a single shank, which can be made as long as required to target even the deepest brain structures [12]–[16]. This electrode style has been used wide range of applications from recording chronic neural activity to pH detection and

drug delivery [15]–[21]. Utah array technology presents a 3-D array of needle-shaped shanks with one electrode site per shank [7], [22], [23] (**Figure 2-3**). The Utah Array consists of a grid design with 100 individual recording shanks, conical in shape, with

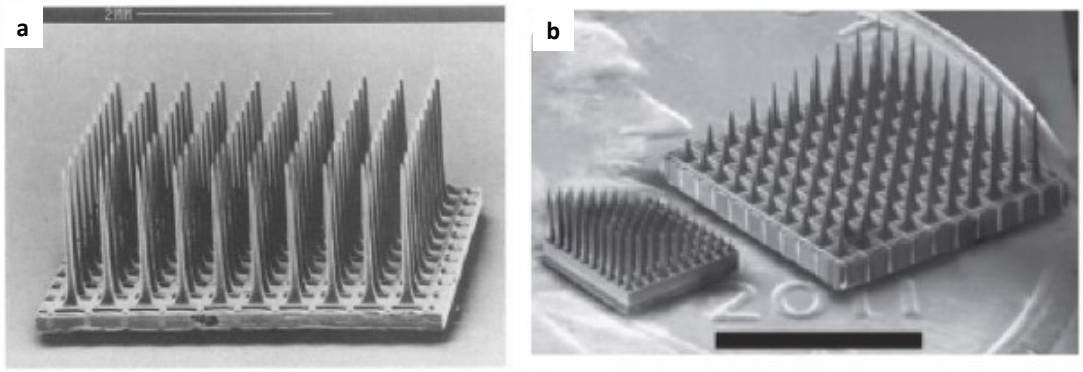

Figure 2-3. (a) A 3-D Utah array [22]. (b) Utah array with variable shank lengths [23].

the recording site at the tip. These arrays have been used as vision prosthesis [7], [22] and motor prosthesis [26], [27]. Their more recent design versions offer lower site impedances and higher shank densities [23], [28], [29].

2.2 Optoelectrodes for combined light delivery and electrical recording

In addition to the electrical recording capability of the technologies discussed above, optogenetic applications require simultaneous light delivery from the same implantable device. Combining precise optogenetic control with reliable electrophysiological readout is a technological challenge, but essential for understanding neural circuit dynamics. Early solutions to deliver light to deep brain structures while simultaneously recording from neurons involved manual assembly of commercially available optical and recording components, resulting in bulky device assemblies (**Figure 2-4a**) [24], [30]. Moreover, stimulation through relatively large light sources placed on the surface of the brain [31] or large fibers (core diameter, ~200 μm) placed in the brain parenchyma [32], [33], inevitably activates many un-

monitored neurons. This called for the integration of thinned optical fibers (**Figure 2-4b)** and monolithic waveguides (**Figure 2-5a-b**) on multielectrode silicon probes [25], [34], [35]. Most of the fiber coupled approaches use confined light (473 nm) from a DPSS (diode-pumped solid-state) laser delivered through a fiber to the waveguide on the neural probe. This approach is not scalable since applying light at multiple brain sites independently would require multiple external fibered-light sources, which would constrain animal movement. More recent advances have led to the integration of laser diode modules on the probe backend [36], [37] (**Figure 2-5c-d**) or μLED light sources on the silicon shank proving high-spatial resolution for optogenetic stimulation [38], [39] (**Figure 2-5e-f**).

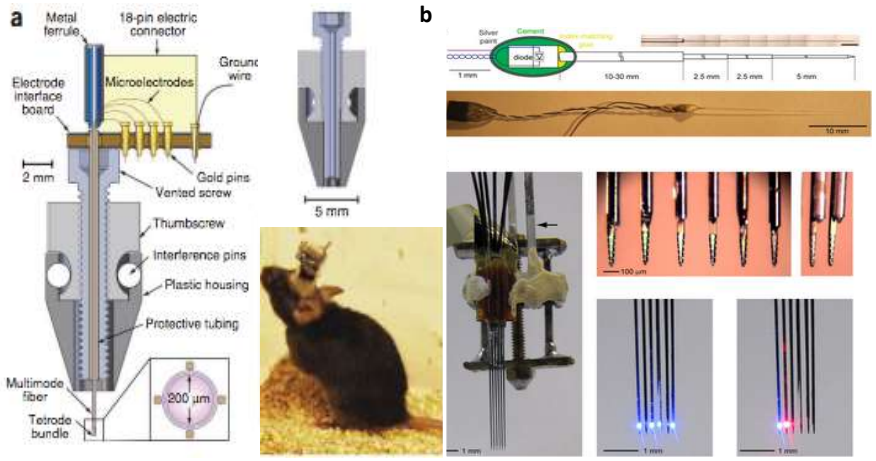

Figure 2-4. Manually assembled optoelectrodes. (a) 200 μm multimode fiber attached to tetrodes and mounted on a mechanical drive [24]. (b) Optical fibers attached to 6-shank Neuronexus probes [25].

Yet none of the current technologies provide a scalable multi-color optogenetic tool, which is fundamental to explore full depth of the optogenetics as discussed in Chapter 1. The only multi-color optical stimulation system (using LED chips and/or laser diode can mounts) reported in the past had optical fibers manually attached to

wire tetrodes or commercial silicon recording probes **Figure 2-4b)** [25]. However, multicolor light delivery could not be achieved at a common site affecting spatial resolution, plus the assembly procedure is manual, hence labor-intensive and prone to inaccuracies. Realizing this unmet technological need, our research goal was to come up with an ultimate optoelectrode solution that combines all the merits of existing state-of-art technologies and provides a multicolor stimulation capability at precise single sites.

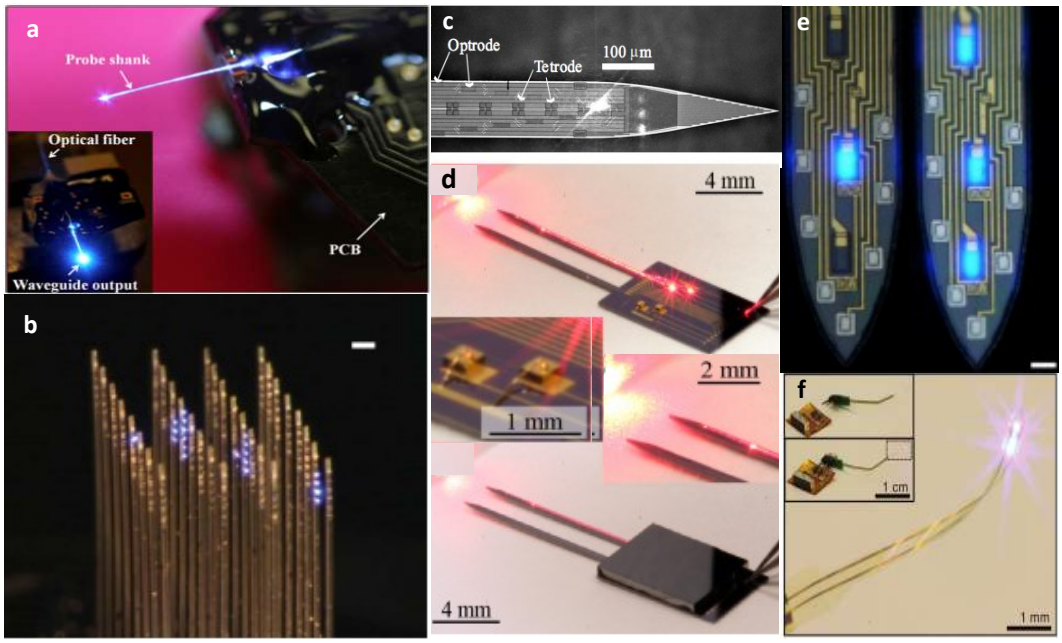

Figure 2-5. Optoelectrodes with integrated light guides or light sources. (a) Optical fiber coupled waveguide probe [35]. (b) Optical fiber coupled 3-D waveguide array [40]. (c, d) Laser diode coupled waveguide probes [36], [37] (e) Monolithic integration of GaN µLEDs on silicon substrate [38]. (f) Hybrid integration of GaN µLED on polymer substrate [39].

2.3 Waveguide designs for fiberless multicolor optoelectrodes

Waveguides provide an attractive design solution for optogenetic stimulation for many reasons. Waveguide materials can be deposited and patterned into thin adjacent channels on a probe shank to create multipoint light delivery probes.

Waveguide designs can be coupled to different colored sources at the device backend to facilitate multicolor light emission. Waveguides can reach deep brain structures such as hippocampus (> 5 mm deep in rodent brains) and illuminate a tissue depth of up to 200 μm easily. Moreover, waveguide designs allow for sources to be located far away from the implant site in the tissue, minimizing tissue heating and electrical noise coupling. If coupled to on-board optical sources, waveguide optoelectrodes can be made fiber-less, i.e. without an in-coupled fiber-optic cable. A fiber-less local photo stimulation is desirable as it permits fast optogenetic manipulations in behaving animals with as many independently controlled light sources, as there are electrodes, without limiting free movement of the animal.

For the design of our waveguide optoelectrodes, we explored various design options with coupled-LEDs (light-emitting diodes) and -ILDs (injection laser diodes). Preliminary studies were done by designing ray tracing models and testing their ability to efficiently couple and guide light. Simulation models were generated in optical modeling software, Zemax (Zemax LLC, Kirkland, WA, USA), followed by design, fabrication and pilot testing. Zemax is an optical design program that can be used to model, analyze and assist in the design of illumination and imaging optical systems. It is a physical optics tool that works by the principle of ray tracing. Zemax applies Snell's Law equations, combined with material properties and boundary conditions to perform complex ray optics analysis with great accuracy and minimum ray tracing time. We used Zemax to characterize source-waveguide coupling and light transmission into the waveguide. A waveguide can accept only those light rays, which are contained within a cone defined by the waveguide's Numerical Aperture (NA).

For optimum coupling efficiency, one needs to match the source diameter-NA product to the fiber core diameter-NA product. **Figure 2-6** shows Zemax design

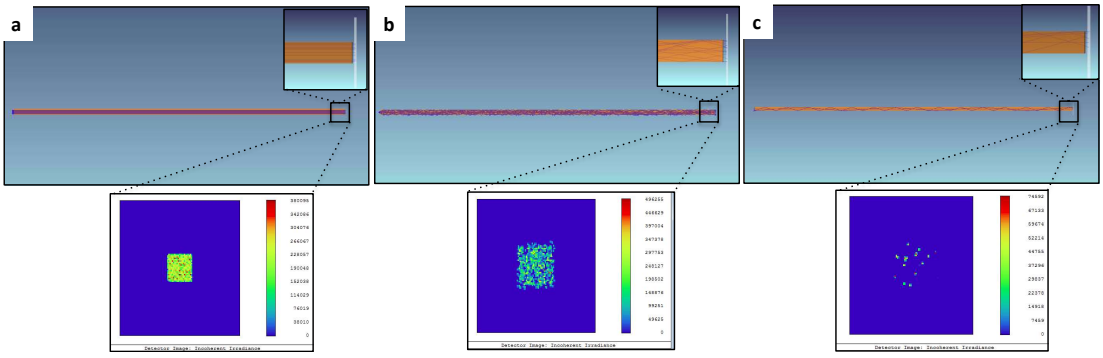

Figure 2-6. Non-sequential mode ray tracing model developed in Zemax. The model consists of a source: (a) Directional multi-mode fiber, (b) ILD, (c) LED, parallel end-butt coupled to a 5mm waveguide with optical output projected on the detector window. The closeup view of waveguide sections show the characteristic ray paths inside the waveguide. The simulation results show a total efficiency of 90.7%, 88.9% and 1.5% for (a), (b) and (c) respectively.

model for a 15µm x 15µm waveguide parallel end-butt coupled to different kinds of light sources: 10 µm core optical fiber (**Figure 2-6a**), 300 µm x 100 µm x 90 µm side-emitting ILD chip with an emission area of 2 µm x 500 nm (**Figure 2-6b**) and 320 µm x 240 µm x 50 µm LED (**Figure 2-6c**). The results displayed at the detector demonstrate how total power and distribution of the collected rays at the output varies as a function of source diameter-NA product and directionality of source. To integrate different light sources in a functional waveguide optoelectrode, following design approaches have been explored.

2.3.1 LED-elliptical reflector coupled waveguide

The first stage design is a modular optical waveguide design using low-cost LEDs (**Figure 2-7a**) and elliptical reflectors (**Figure 2-7b**). The principle of elliptical reflectors [41]–[44] is used for optimal collection of light from an LED. LED is

placed at one focal point to steer the light to reflect and converge into the other focal point. The reflector is tapered to guide the light from the converged focal point [45]–[48].

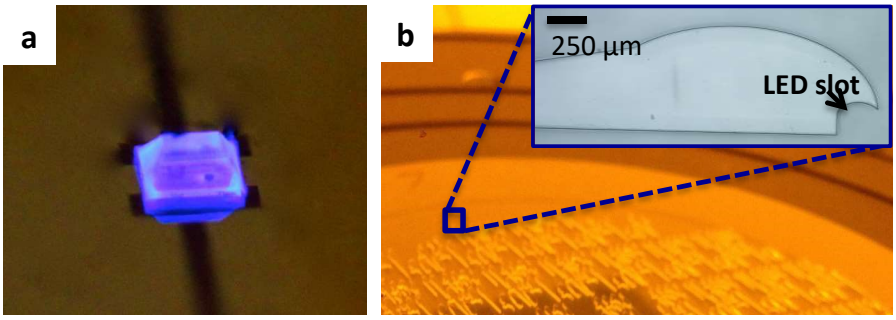

Figure 2-7. (a) CREE DA2432 blue LED (150mW available power from all surfaces). (b) Fabricated elliptical reflectors on glass wafer; inset shows the top view of the reflector with LED slot at the ellipse focus.

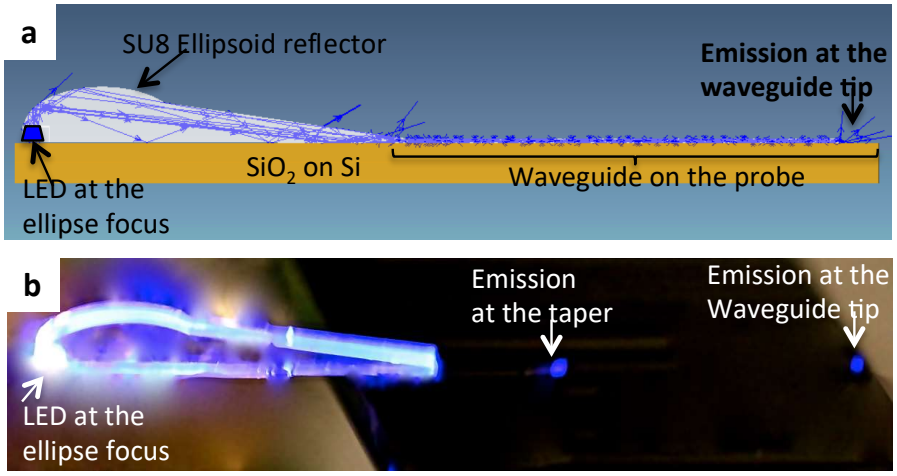

Figure 2-8. (a) Zemax model of an elliptical reflector coupled to a 5mm long 50x50 µm waveguide with one taper. Only rays collected at detector are shown. (b) Actual prototyped system at low power. First and second emission points are at the taper and waveguide tip. Power at tip of 50 x 50 µm waveguide was 0.20 % total efficiency, which is 46 % of the ray-trace model (0.43 %) and 21 % of the theoretical limit.

This approach is innovative because we can effectively collect most of illuminating light from the LED surface, which is typically in Lambertian profile with a large solid emission angle. Since the plane of the ellipse is orthogonal to the plane of the

waveguide, simple planar waveguide fabrication can be applied. This idea allows us to place the LEDs onto the printed circuit board (PCB) has many important repercussions. It moves the electromagnetic interference sufficiently far from the sensitive neural signals and allows us to manage electrical design on a multilayer PCB and also manages heat efficiently and protects the tissue. The specific version of the reflector tested was based on a 2 mm x 1 mm ellipse and tapered at 8°. Ray tracing in Zemax predicted an efficiency of 3.8 % at its output (300 μm x 50 μm) and we measured 1.5 % output. For a 50 μm x 50 μm waveguide, the ray tracing predicted 0.43 % (**Figure 2-8a**) and we measured 0.2 % (4.4 mW/mm^2) (**Figure 2-8b**). Although, the achieved intensity was adequate to stimulate nearby neurons for optogenetics, it was not high enough to stimulate deeper tissue depths or larger tissue volumes. Hence, we explored the methods explained below to achieve higher coupling efficiency from LED to the waveguide.

2.3.2 LED-/ILD-grating coupled waveguide

In order to enhance light collection from the LED, we also simulated an LED-diffractive grating coupler [49]–[51]. We designed a radial grating pattern and a Bragg reflector to couple and then reflect the LED light into an in-plane dielectric waveguide (**Figure 2-9**) [50], [52]**.** The simulation results demonstrated increase in efficiency as compared to elliptical reflector design, bringing up the total system efficiency to 0.45 % for 465 nm for 0.4 μm x 20 μm waveguide output. If the LED light source (67.5^o incident angle) is replaced by an ILD light source (30^o incident angle), the system efficiency can be increased up to 30-50% **(Appendix A)**. Some recent studies have shown integration of gratings on the neural probe [37], [53].

However, such designs (whether coupled to fiber, LED or ILD) can be fairly sensitive to source-grating separation distance in range of nanometers, making device packaging very challenging when scaling up. If the source is an optical fiber [53], it can further increase the challenge of scaling up. Also, the design of grating couplers requires nano-fabrication techniques, bringing up the cost of production.

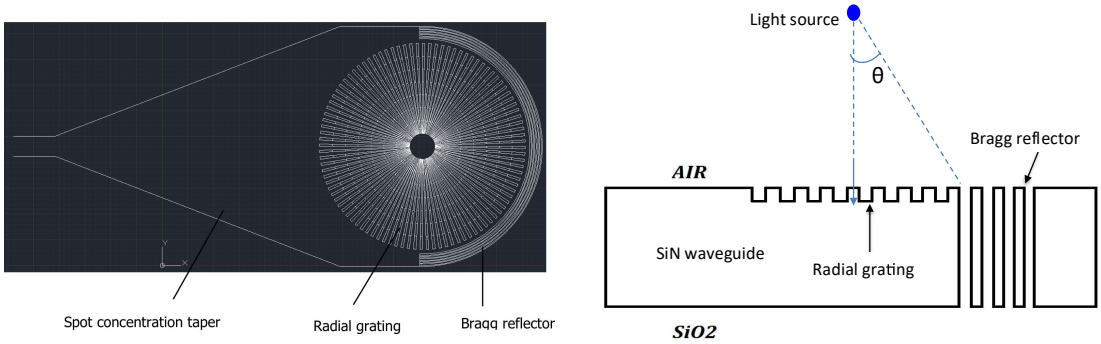

Figure 2-9. (a) Radial grating design with Bragg reflector to couple light from a light source. (a) Top-view. (b) Side view showing a source in perpendicular plane with incident angle of light, θ.

2.3.3 ILD-GRIN coupled waveguide

Laser coupled waveguide systems are most efficient and compact systems to couple and guide light (**Figure 2-6b**). The only port of optical loss for a multimodal laser-waveguide system could be the coupling junction between the laser and the waveguide. The optical loss at this coupling joint could either occur due to angular diffraction of ILD emission or due to misalignment between ILD and waveguide. The angular diffraction exhibited by ILDs can cause considerable optical loss when coupling light into small symmetrical elements such as optical waveguides. To optimize coupling efficiency between a divergent laser beam and a step-graded waveguide, we implemented a collimation-focusing mechanism between side emitting ILDs and waveguides using a GRIN lens [54]–[56]. Since a GRIN lens has a

continuous change of the refractive index (RI) within the lens material, light rays can be continuously bent within the lens until they are finally focused on a spot. GRIN-based optical coupling requires exact, design-specific spacing between the coupled components (ILD, GRIN and waveguide), which can be reliably achieved using micro-electro-mechanical systems (MEMS) fabrication.

Table 2.1. Characteristics offered by various optoelectrode designs.

Waveguide Design	**High optical efficiency**	**Scalability**	**Multiple color generation**	**Fiber-less**	**Effective thermal/electrical packaging**
Fiber-coupled waveguides		✓	✓		✓
Integrated light sources on shank		✓		✓	✓
LED-elliptical reflector coupled waveguides		✓	✓	✓	✓
LED-diffractive grating coupled waveguides		✓	✓	✓	
ILD-GRIN coupled waveguides	✓	✓	✓	✓	✓

The Zemax model for ILD-GRIN coupled dielectric waveguide demonstrates coupling efficiency of ~60% (highest amongst all of the tested designs) for 405 nm wavelength at 30μm x 15μm output port of a 5mm long waveguide. The design was further modified in Zemax to implement an optical mixer design [57] and optimized to minimize alignment errors. The optical model details are described in Chapter 3. **Table 2.1** provides a comparison between optoelectrode characteristics offered by the

discussed design stages in this section when compared to other state-of-art technologies.

2.4 Discussion

The development of novel brain tools has the potential to fill up crucial missing links in exploring the full depth of neuroscience studies. As optogenetics is gaining unprecedented momentum and optoelectrode technologies are being developed at frenetic pace. Together, they are revolutionizing the face of neuroscience studies, giving us a chance now to ask questions that we did not even know were worth asking few years ago. The optoelectrode technology has come a long way from the implementation of crude bulky optical fibers to the development of scalable micro-technology with integrated light sources. Both LEDs and ILDs provide attractive solutions for integrated micro-optics but come with their respective limitations. While LEDs have numerous advantages like compactness, easy availability in a larger color gamut, low cost and a longer lifetime, they suffer from an important disadvantage: the optical power per unit of etendue (luminance) of an LED is significantly lower. Because of this and the etendue limitation of the waveguide (small collection area, limited NA), the system collection efficiency of an LED coupled system is significantly low for high optical power applications and less efficiency tolerant optical systems. ILDs, unlike LEDs, exhibit highly directional nature of the emitted light. Moreover, an ILD can be a side-emitting device, unlike an LED, which emits from top and sides and exhibits high spectral purity. The only limiting factor for implementation of visible range ILDs in integrated micro-optic systems is their limited availability in commercial market. Low-wavelength ILDs (400-600 nm) are a

relatively new semiconductor technology than LEDs, and hence are difficult to find in bare chip form in the current market. They are usually sold in packaged dies (like 3-legged TO cans with 3.8 mm smallest diameter), which cannot be integrated into micro-systems due to their larger size. Although, as the semiconductor industry expands further in coming years, ILD chips are likely to become more available in multiple colors for commercial sale.

References

[1] S. J. M. Smith, "EEG in the diagnosis, classification, and management of patients with epilepsy.," *J. Neurol. Neurosurg. Psychiatry*, vol. 76 Suppl 2, p. ii2-7, 2005.

[2] A. Steiger and M. Kimura, "Wake and sleep EEG provide biomarkers in depression," *Journal of Psychiatric Research*, vol. 44, no. 4. pp. 242–252, 2010.

[3] D. Khodagholy, J. N. Gelinas, T. Thesen, W. Doyle, O. Devinsky, G. G. Malliaras, and G. Buzsaki, "NeuroGrid: recording action potentials from the surface of the brain," *Nat Neurosci*, vol. 18, pp. 310–315, 2015.

[4] C. A. Chestek, V. Gilja, C. H. Blabe, B. L. Foster, K. V Shenoy, J. Parvizi, and J. M. Henderson, "Hand posture classification using electrocorticography signals in the gamma band over human sensorimotor brain areas.," *J. Neural Eng.*, vol. 10, no. 26002, 2013.

[5] J. C. Williams, R. L. Rennaker, and D. R. Kipke, "Long-term neural recording characteristics of wire microelectrode arrays implanted in cerebral cortex," *Brain Res. Protoc.*, vol. 4, no. 3, pp. 303–313, 1999.

[6] K. D. Wise, A. M. Sodagar, Y. Yao, M. N. Gulari, G. E. Perlin, and K. Najafi, "Microelectrodes, microelectronics, and implantable neural microsystems," *Proc. IEEE*, vol. 96, no. 7, pp. 1184–1202, Jul. 2008.

[7] P. K. Campbell, K. E. Jones, R. J. Huber, K. W. Horch, and R. a Normann, "A silicon-based, 3-dimensional neural interface - manufacturing processes for an intracortical electrode array," *IEEE Trans. Biomed. Eng.*, vol. 38, no. 8, pp. 758–768, 1991.

[8] W. T. Tseng, C. T. Yen, and M. L. Tsai, "A bundled microwire array for long-term chronic single-unit recording in deep brain regions of behaving rats," *J. Neurosci. Methods*, vol. 201, no. 2, pp. 368–376, 2011.

[9] K. D. Wise, "Silicon microsystems for neuroscience and neural prostheses," *IEEE Eng. Med. Biol. Mag.*, vol. 24, no. 5, pp. 22–29, Sep. 2005.

[10] G. E. Perlin and K. D. Wise, "An ultra compact integrated front end for wireless neural recording microsystems," *J. Microelectromechanical Syst.*, vol. 19, no. 6, pp. 1409–1421, 2010.

[11] J. Csicsvari, D. A. Henze, B. Jamieson, K. D. Harris, A. Sirota, and K. D. Wise, "Massively Parallel Recording of Unit and Local Field Potentials With Silicon-Based Electrodes," *Journal of Neurophysiology*, vol. 90, pp. 1314-1323, 2003.

[12] K. D. Wise, D. J. Anderson, J. F. Hetke, D. R. Kipke, and K. Najafi, "Wireless implantable microsystems: High-density electronic interfaces to the nervous system," in *Proceedings of the IEEE*, 2004, vol. 92, no. 1, pp. 76–97.

[13] K. D. Wise and J. B. Angell, "A low capacitance multielectrode probe for use in extracellular neurophysiology," *IEEE Transactions on Biomedical Engineering*, vol. BME-22, no. 3. pp. 212–220, 1975.

[14] K. Najafi, K. D. Wise, and T. Mochizuki, "A high-yield IC-compatible multichannel Recording Array," *Electron Devices IEEE Trans.*, vol. 32, no. 7, pp. 1206–1211, 1985.

[15] D. R. Kipke, R. J. Vetter, J. C. Williams, and J. F. Hetke, "Silicon-substrate intracortical microelectrode arrays for long-term recording of neuronal spike activity in cerebral cortex," *IEEE Trans. Neural Syst. Rehabil. Eng.*, vol. 11, no. 2, pp. 151–155, 2003.

[16] R. J. Vetter, J. C. Williams, J. F. Hetke, E. A. Nunamaker, and D. R. Kipke, "Chronic neural recording using silicon-substrate microelectrode arrays implanted in cerebral cortex," *IEEE Trans. Biomed. Eng.*, vol. 51, no. 6, pp. 896–904, 2004.

[17] K. a Ludwig, J. D. Uram, J. Yang, D. C. Martin, and D. R. Kipke, "Chronic neural recordings using silicon microelectrode arrays electrochemically deposited with a poly(3,4-ethylenedioxythiophene) (PEDOT) film.," *J. Neural Eng.*, vol. 3, no. 1, pp. 59–70, Mar. 2006.

[18] K. J. Otto, M. D. Johnson, and D. R. Kipke, "Voltage pulses change neural interface properties and improve unit recordings with chronically implanted microelectrodes," *IEEE Trans. Biomed. Eng.*, vol. 53, no. 2, pp. 333–340, 2006.

[19] A. Berényi, Z. Somogyvári, A. J. Nagy, L. Roux, J. D. Long, S. Fujisawa, E. Stark, A. Leonardo, T. D. Harris, and G. Buzsáki, "Large-scale, high-density (up to 512 channels) recording of local circuits in behaving animals.," *J. Neurophysiol.*, vol. 111, no. 5, pp. 1132–49, Mar. 2014.

[20] M. D. Johnson, O. E. Kao, and D. R. Kipke, "Spatiotemporal pH dynamics following insertion of neural microelectrode arrays," *J. Neurosci. Methods*, vol. 160, no. 2, pp. 276–287, 2007.

[21] P. Rohatgi, N. B. Langhals, D. R. Kipke, and P. G. Patil, "In vivo performance of a microelectrode neural probe with integrated drug delivery.," *Neurosurg. Focus*, vol. 27, no. 1, p. E8, 2009.

[22] C. T. Nordhausen, E. M. Maynard, and R. A. Normann, "Single unit recording capabilities of a 100 microelectrode array," *Brain Res.*, vol. 726, no. 1–2, pp. 129–140, 1996.

[23] H. A. C. Wark, K. S. Mathews, R. A. Normann, and E. Fernandez, "Behavioral and cellular consequences of high-electrode count Utah Arrays chronically implanted in rat sciatic nerve.," *J. Neural Eng.*, vol. 11, no. 4, p. 46027, 2014.

[24] P. Anikeeva, A. S. Andalman, I. Witten, M. Warden, I. Goshen, L. Grosenick, L. a

Gunaydin, L. M. Frank, and K. Deisseroth, “Optetrode: a multichannel readout for optogenetic control in freely moving mice,” *Nat. Neurosci.*, vol. 15, no. 1, pp. 163–170, Jan. 2011.

[25] E. Stark, T. Koos, and G. Buzsáki, “Diode probes for spatiotemporal optical control of multiple neurons in freely moving animals.,” *J. Neurophysiol.*, vol. 108, no. 1, pp. 349–63, Jul. 2012.

[26] E. M. Maynard, C. T. Nordhausen, and R. A. Normann, “The Utah Intracortical Electrode Array: A recording structure for potential brain-computer interfaces,” *Electroencephalogr. Clin. Neurophysiol.*, vol. 102, no. 3, pp. 228–239, 1997.

[27] L. R. Hochberg, D. Bacher, B. Jarosiewicz, N. Y. Masse, J. D. Simeral, J. Vogel, S. Haddadin, J. Liu, S. S. Cash, P. van der Smagt, and J. P. Donoghue, “Reach and grasp by people with tetraplegia using a neurally controlled robotic arm,” *Nature*, vol. 485, no. 7398, pp. 372–375, 2012.

[28] X. Xie, L. Rieth, S. Negi, R. Bhandari, R. Caldwell, R. Sharma, Prashant<p>Tathireddy, and F. Solzbacher, “Self-aligned tip deinsulation of atomic layer deposited Al2O3 and parylene C coated Utah electrode array based neural interfaces,” *J. Micromechanics Microengineering*, vol. 24, no. 3, p. 35003, 2014.

[29] S. Negi, R. Bhandari, L. Rieth, and F. Solzbacher, “In vitro comparison of sputtered iridium oxide and platinum-coated neural implantable microelectrode arrays,” *Biomed. Mater.*, vol. 5, no. 1, p. 15007, 2010.

[30] V. Gradinaru, K. R. Thompson, F. Zhang, M. Mogri, K. Kay, M. B. Schneider, and K. Deisseroth, “Targeting and readout strategies for fast optical neural control in vitro and in vivo.,” *J. Neurosci.*, vol. 27, no. 52, pp. 14231–14238, 2007.

[31] D. Huber, L. Petreanu, N. Ghitani, S. Ranade, T. Hromádka, Z. Mainen, and K. Svoboda, “Sparse optical microstimulation in barrel cortex drives learned behaviour in freely moving mice.,” *Nature*, vol. 451, no. 7174, pp. 61–4, Jan. 2008.

[32] A. V Kravitz, B. S. Freeze, P. R. L. Parker, K. Kay, M. T. Thwin, K. Deisseroth, and A. C. Kreitzer, “Regulation of parkinsonian motor behaviours by optogenetic control of basal ganglia circuitry.,” *Nature*, vol. 466, no. 7306, pp. 622–6, Jul. 2010.

[33] M. M. Halassa, J. H. Siegle, J. T. Ritt, J. T. Ting, G. Feng, and C. I. Moore, “Selective optical drive of thalamic reticular nucleus generates thalamic bursts and cortical spindles.,” *Nat. Neurosci.*, vol. 14, no. 9, pp. 1118–20, Sep. 2011.

[34] A. N. Zorzos, E. S. Boyden, and C. G. Fonstad, “Multiwaveguide implantable probe for light delivery to sets of distributed brain targets.,” *Opt. Lett.*, vol. 35, no. 24, pp. 4133–5, Dec. 2010.

[35] F. Wu, E. Stark, M. Im, I.-J. Cho, E.-S. Yoon, G. Buzsáki, K. D. Wise, and E. Yoon, "An implantable neural probe with monolithically integrated dielectric waveguide and recording electrodes for optogenetics applications.," *J. Neural Eng.*, vol. 10, no. 5, p. 56012, Oct. 2013.

[36] M. Schwaerzle, K. Seidl, U. T. Schwarz, O. Paul, and P. Ruther, "Ultracompact optrode with integrated laser diode chips and SU-8 waveguides for optogenetic applications," in *Proceedings of the IEEE International Conference on Micro Electro Mechanical Systems (MEMS)*, 2013, pp. 1029–1032.

[37] L. Hoffman, M. Welkenhuysen, A. Andrei, S. Musa, Z. Luo, S. Libbrecht, S. Severi, P. Soussan, V. Baekelandt, S. Haesler, G. Gielen, R. Puers, and D. Braeken, "High-density optrode-electrode neural probe using SixNy photonics for in vivo optogenetics," in *International Electron Devices Meeting, IEDM*, 2016, vol. 2, p. 29.5.1-29.5.4.

[38] F. Wu, E. Stark, P. C. Ku, K. D. Wise, G. Buzsáki, and E. Yoon, "Monolithically Integrated μLEDs on Silicon Neural Probes for High-Resolution Optogenetic Studies in Behaving Animals," *Neuron*, vol. 88, no. 6, pp. 1136–1148, 2015.

[39] T. Kim, J. G. McCall, Y. H. Jung, X. Huang, E. R. Siuda, Y. Li, J. Song, Y. M. Song, H. A. Pao, R.-H. Kim, C. Lu, S. D. Lee, I.-S. Song, G. Shin, R. Al-Hasani, S. Kim, M. P. Tan, Y. Huang, F. G. Omenetto, J. A. Rogers, and M. R. Bruchas, "Injectable, Cellular-Scale Optoelectronics with Applications for Wireless Optogenetics," *Science (80-.).*, vol. 340, no. 6129, pp. 211–216, Apr. 2013.

[40] A. N. Zorzos, J. Scholvin, E. S. Boyden, and C. G. Fonstad, "Three-dimensional multiwaveguide probe array for light delivery to distributed brain circuits.," *Opt. Lett.*, vol. 37, no. 23, pp. 4841–3, Dec. 2012.

[41] C. W. R. Carter, Robert Rhoades, "Lamp structure, having elliptical reflectors, for uniformly irradiating surfaces of optical fiber and method of use thereof," US Patent 09 885 004, Jan-2002.

[42] Z. Hou, Y. Huang, and S. T. Ho, "Physics of Curved Reflectors at Large Reflection and Divergence Angles: Analysis of Optical Beam Distortions in Ultra-Large-Angle Elliptical Curved Reflectors and Their Design and Applications for Nano-Photonic Integrated Circuits I," *Opt. Commun.*, vol. 287, pp. 106–116, Jan. 2013.

[43] H. Rehn, "Optical properties of elliptical reflectors," *Opt. Eng.*, vol. 43, p. 1480, 2004.

[44] S. R. M. Jeffrey M. Singer, David Barnett, "LED spotlight including elliptical and parabolic reflectors," US Patent 12 887 379, 2013.

[45] D. S., C. A., and S. S., "Analysis of Tapered waveguide by two approaches," *Prog. Electromagn. Res.*, vol. 64, pp. 219–238, 2006.

[46] H. Murat, A. Gielen, and H. De Smet, “Gradually tapered light pipes for illumination of LED projectors,” *J. Soc. Inf. Disp.*, vol. 15, no. 7, p. 519, 2007.

[47] O. Mitomi, K. Kasaya, and H. Miyazawa, “Design of a single-mode tapered waveguide for low-loss chip-to-fiber coupling,” *IEEE J. Quantum Electron.*, vol. 30, no. 8, pp. 1787–1793, 1994.

[48] P. G. Suchoski and R. V. Ramaswamy, “Design of single-mode step-tapered waveguide sections,” *IEEE J. Quantum Electron.*, vol. 23, no. 2, pp. 205–211, Feb. 1987.

[49] H. Ichikawa and T. Baba, “Efficiency enhancement in a light-emitting diode with a two-dimensional surface grating photonic crystal,” *Appl. Phys. Lett.*, vol. 84, no. 4, pp. 457–459, 2004.

[50] S. Siitonen, P. Laakkonen, P. Vahimaa, M. Kuittinen, and N. Tossavainen, “White LED light coupling into light guides with diffraction gratings.,” *Appl. Opt.*, vol. 45, no. 12, pp. 2623–2630, 2006.

[51] P. Laakkonen, S. Siitonen, T. Levola, and M. Kuittinen, “High efficiency diffractive incouplers for light guides,” in *Integrated Optics: Devices*, 2008, vol. 6896, p. 68960E–68960E–11.

[52] C.-S. Huang and W.-C. Wang, “SU8 inverted-rib waveguide Bragg grating filter.,” *Appl. Opt.*, vol. 52, no. 22, pp. 5545–51, Aug. 2013.

[53] E. Shim, Y. Chen, S. Masmanidis, and M. Li, “Multisite silicon neural probes with integrated silicon nitride waveguides and gratings for optogenetic applications.,” *Sci. Rep.*, vol. 6, no. February, p. 22693, 2016.

[54] M. Riedl, *Optical Design Fundamentals for Infrared Systems, Second Edition*. Bellingham, WA: SPIE Press, 2001.

[55] W. J. Smith, *Modern Optical Engineering*. Tata McGraw-Hill Education, 1966.

[56] K. Kampasi, J. Seymour, K. Na, K. D. Wise, and E. Yoon, “Fiberless multicolor optoelectrodes using Injection Laser Diodes and Gradient-index lens coupled optical waveguides,” in *Proceedings of the 18th International Conference on Solid-State Sensors, Actuators and Microsystems (TRANSDUCERS)*, 2015, pp. 273–276.

[57] K. Kampasi, E. Stark, J. Seymour, K. Na, H. G. Winful, G. Buzsáki, K. D. Wise, and E. Yoon, “Fiberless multicolor neural optoelectrode for in vivo circuit analysis,” *Sci Rep, Nat. Publ. Gr.*, vol. 6, 2016.

Chapter 3

Fiberless Multicolor Optoelectrodes Using ILD and GRIN Coupled Waveguides

3.1 Introduction

This chapter describes the design and *in vivo* validation of a novel fiber-less multicolor optoelectrode. The key design idea is the coupling of compact ILDs to a monolithic oxynitride optical mixer waveguide on a silicon probe through GRIN lenses [1]–[4]. The use of GRIN lenses [3], [5], [6] attains several merits over alternative, conventional approaches for compact optoelectronic designs. It collimates and focuses the in-coupled divergent laser beam. The flat GRIN ends facilitate efficient butt-coupling and lenses can be designed with a diameter as small as 250 μm. This simple geometry in a miniature package allows compact optical coupling and assembly for microscale optoelectronic devices. The wide misalignment tolerance range offered by the GRIN lens maintains reproducible assembly and high yield during production. Finally, GRIN lenses provide good thermal isolation between the ILDs and the silicon probe, minimizing tissue heating.

The dielectric mixer enables multicolor stimulation at a scalable common waveguide port (7 x 30 μm), providing a novel feature that allows addressing neuroscience questions requiring, for instance, independent activation (with 405 nm light) and silencing (with 635 nm light) of the cells within a given locality. The neural

probe shank tip has monolithically integrated iridium electrode sites (with 20 μm pitch) to facilitate high-density recordings from dense brain regions such as mouse hippocampus. Such a precise multicolor optogenetic tool can facilitate various combinatorial experiments, including: (i) independent activation and silencing of a single cell, (ii) independent activation of two spatially intermingled cells types, and (iii) independent silencing of two spatially intermingled cells types; none of which are possible with the current neural technologies.

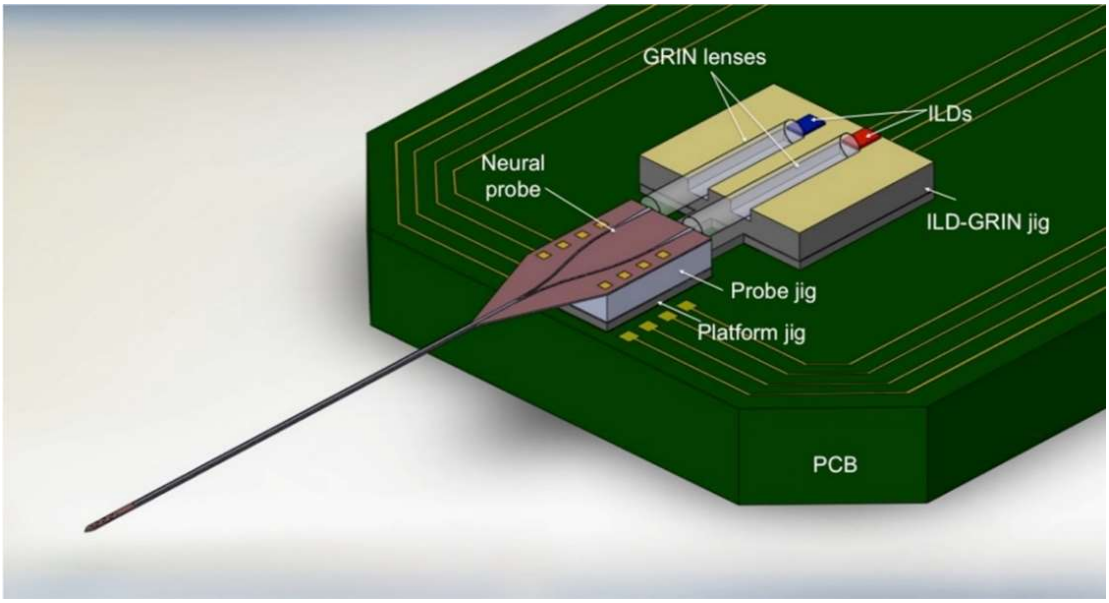

Figure 3-1: Schematic of assembled optoelectrode on a printed circuit board (PCB).

In this chapter, we present the optical and thermal device design, device fabrication and integrated micro-optic assembly. We also show validation of packaged devices in the intact brain of anesthetized mice co-expressing Channelrhodopsin-2 and Archaerhodopsin in pyramidal cells in the hippocampal CA1 region, achieving high quality recording, activation and silencing of the exact same neurons in a given local region [3].

3.2 Design

Figure 3-1 shows schematic of a GRIN-based optoelectrode showing details of different assembly components. The neural probe has a dielectric optical waveguide mixer enabling two-color stimulation at a single port. The backend of the probe hosts ILD-GRIN jig which houses ILDs and GRINs and also acts as a separate electrical and thermal housing for the light sources. The design details are described as follows.

3.2.1 Optical design

The angular diffraction exhibited by lasers can cause considerable optical loss when coupling light into small symmetrical elements such as optical waveguides. To optimize coupling efficiency between a divergent laser beam and a step-graded waveguide, we implemented a collimation-focusing mechanism using a GRIN lens [6], [7]. Since the lens has a continuous change of the refractive index (RI) within the lens material, light rays can be continuously bent within the lens until they are finally focused on a spot at the distal end. GRIN-based optical coupling requires exact, design-specific spacing between the coupled components (ILD, GRIN and waveguide), which can be reliably achieved using micro-electro-mechanical systems (MEMS) fabrication. GRIN design parameters including numerical aperture (NA), working distance, and mechanical length (Z), were optimized to achieve the desired magnification (M<1) for enhanced optical coupling. The design was then shared with the lens manufacturers (NSG, Japan, via Go!Foton lens distributors in Somerset, NJ, USA). Primary GRIN design equations are: RI at radius r, $N(r) = N_o[1-(A/2)r^2]$ [7]; mechanical length, $Z = 2\pi P/\sqrt{A}$ [7]; numerical aperture, $NA = n_o \sin\theta_a$, where N_o is the RI at the lens central axis (1.65); $\sqrt{A}$ is the designed index gradient constant

(mm^{-1}), which depends on lens material and wavelength; P is a lens pitch (fraction of a full sinusoidal period of ray path); n_o is the RI of surrounding medium around GRIN; and θ_a is the lens acceptance angle (25 degrees).

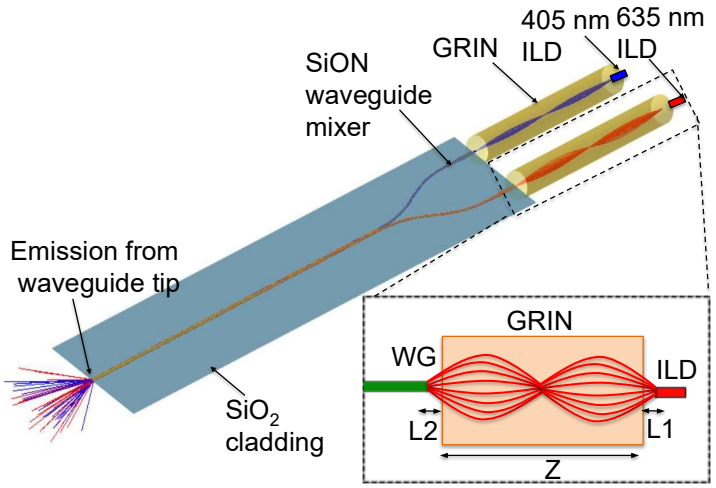

Figure 3-2. Zemax optical model of optical mixer waveguide (7.04 mm total length) coupled to ILDs to deliver multicolor output at the single waveguide port. The model consists of two ILDs (405 nm and 635 nm) coupled to two arms (each 2 mm long) of optical mixer via 405 nm (2.38 mm long) and 635 nm (2.54 mm) GRIN lenses. The schematic in the inset shows a full pitch GRIN lens collimating and focusing a divergent ILD laser beam into the waveguide mixer arm (WG). L1 and L2 denote object and image distances, respectively, that can fit well within the device fabrication and assembly precision.

For efficient coupling of the GRIN lens to the waveguide, the latter should have an NA equal or higher than the former. Then, all incoming rays from the GRIN lens can be efficiently collected by the waveguide if aligned perfectly, and the only loss occurring at the coupling interface are reflection (Fresnel) losses. Fresnel losses are given by $F_L = (n_2 - n_1 / n_2 + n_1)^2$, where n_1 and n_2 are the RIs of the first and second media, respectively. In the current implementation, the waveguide NA is 0.4228 (designed to closely match the NA of the GRIN lens, 0.4226) using $NA_{wg} = \sqrt{(n_{core}^2 - n_{clad}^2)}$, where n_{core} is the RI of the waveguide core (silicon oxynitride,

1.52) and n_{clad} is the RI of the waveguide cladding (silicon dioxide, 1.46). Using the Fresnel equation, reflective losses were calculated as 0.462 dB at the ILD-GRIN junction (assuming an intermediate medium with RI=1.56) and 0.463 dB at the GRIN-waveguide junction, yielding a total coupling loss of 0.925 dB (i.e., >80% total coupling efficiency from ILD to GRIN and GRIN to waveguide backend).

Our waveguide design is based upon parametric ray tracing models (Zemax LLC, Kirkland, WA, USA) shown in **Figure 3-2**. GRIN lenses were designed and simulated in Zemax to facilitate optimal coupling while allowing maximum misalignment tolerance between the ILDs and the waveguide. We chose a full-pitch (P=1) GRIN lens of high NA which gives a focused beam at the GRIN output as the beam travels exactly one full cycle of a sinusoidal period in that distance, achieving beam focusing on the other end (**Figure 3-2, *inset***). The focused beam enters the waveguide mixer arms, which taper down from a width of 50 μm to 30 μm and then converge into a 5 mm-long straight waveguide (cross-section: 30 μm x 7 μm). Due to optical mode distortion, radiation losses occur in the waveguide bends. These losses can be minimized by designing the bend with a large radius of curvature. However, large curvature comes at the cost of a longer light path, resulting in higher transmission losses and larger device size, which is often limited by the maximum tolerance of pitch for micro-optical assemblies (in our case, limited by the diameter of the GRIN lenses). Due to this tradeoff, we designed the mixer with maximum bend radius of 2.32 mm while maintaining a minimum pitch between GRIN lenses; and achieved simulated radiation loss within 1 dB [8], [9]. Other than coupling and radiation loss, light rays also suffer from as propagation loss, which is attenuation in

the form of scattering and absorption as they travel through the guide. Scattering losses are caused due to imperfections such as voids and contaminant atoms and usually predominate in dielectric waveguides. Absorption losses are dependent on material absorption coefficient for a particular wavelength and are significant in semiconductors and other crystalline materials. The theoretical estimation of propagation losses is difficult; but these losses are characterized experimentally in Section 3.4.2 ahead. Finally, the total optical loss of the system, L_T, is sum of all three loss-types: $L_T(dB) = L_{coupling}(dB) + L_{propagation}(dB) + L_{radiation}(dB)$.

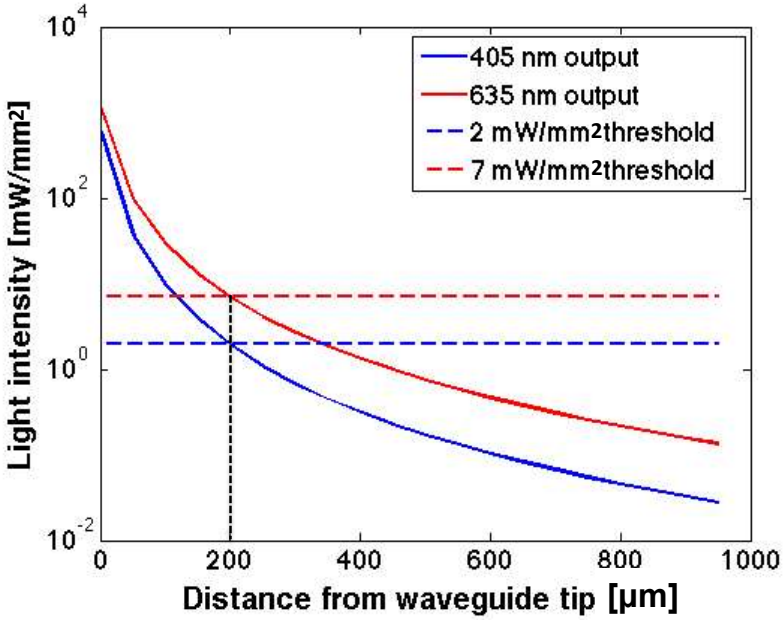

Figure 3-3. Simulated light intensity curves at waveguide tip as a function of tissue depths. When output intensity at the waveguide tip is 476 mW/mm^2 for 405 nm and 952 mW/mm^2 for 635 nm, respectively, the tissue up to 200 µm away from the waveguide tip is illuminated at supra-threshold intensity[10].

The waveguide aperture on the neural shank was positioned 55 µm away from the first recording site to minimize damage to the recorded neurons [11]–[13]. Since the recording sites span 140 µm, opsin activation thresholds must be crossed at a

distance of ~200 μm from the tip of the of 7 μm x 30 μm waveguide. The design values used were: 405 nm light, intensity of 2 mW/mm^2 for ChR2 [10], [14]; and 635 nm, intensity of 7 mW/mm^2 for Halo/Arch [15], [16]. Considering waveguide geometric losses and tissue scattering losses through brain tissue for each wavelength [10], [13], the required light intensity is achieved at a distance of 200 μm from the waveguide if the output power (intensity) at the waveguide tip exceeds 100 μW (476 mW/mm^2) for 405nm and 200 μW (952 mW/mm^2) for 635nm (**Figure 3-3**).

3.2.2 Thermal design

Although there is no established temperature threshold for safe operation of neural probes when implanted in brain tissue [17], temperature can affect neuronal activity on cellular and population level in various manners [18]–[20]. Therefore, we loosely define the design threshold as 1°C temperature rise from the baseline tissue temperature of 37°C for a conservative thermal model analysis [3], [21].

Optical power above 200 μW must be emitted at the 7 x 30 μm waveguide tip to achieve optogenetic activation in tissue as far as 200 μm away (**Figure 3-3**). Due to the high optical efficiency provided by the GRIN-based design, this can be achieved using low-power ILDs and driving them just above their stimulated emission threshold, at an input electrical power of ~80 mW. For conservative modeling, we assumed all electrical input power is dissipated as heat. We used a computerized heat transfer model (COMSOL Multiphysics, Burlington, MA, USA) to simulate the temperature rise of the electro-optical components and the tissue around the GRIN-based optoelectrode (**Figure 3-4a**). The model design was also compared to a conventional butt-coupled design where ILD was directly coupled to the waveguides

without using an intermediate GRIN lens. The simulation results (**Figure 3-5**) indicate that for GRIN-coupled design, both ILDs can be driven continuously for 190 seconds

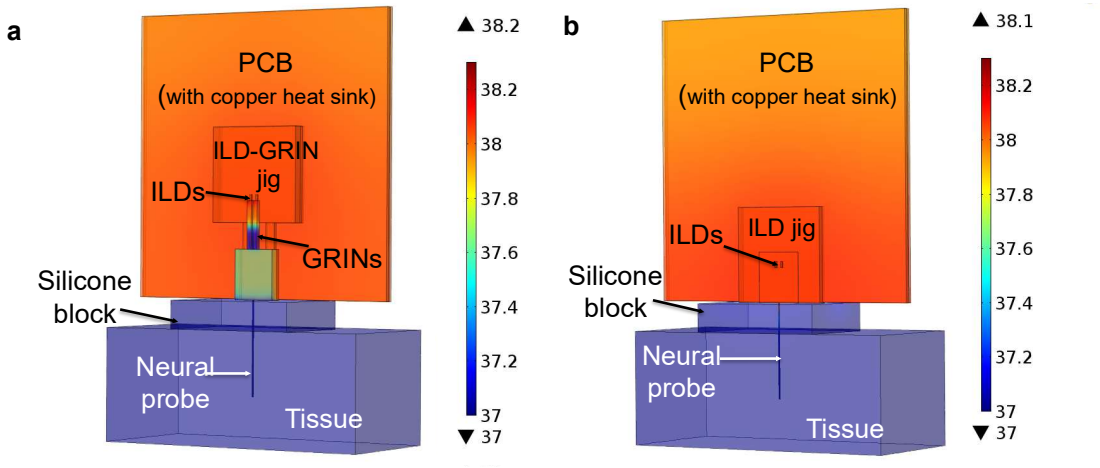

Figure 3-4. COMSOL model for a single shank optoelectrode for (a) GRIN-coupled and (b) butt-coupled design, showing surface temperature rise of optoelectrode components and tissue surface at 20 seconds when two ILDs are operated at 10% duty cycle power.

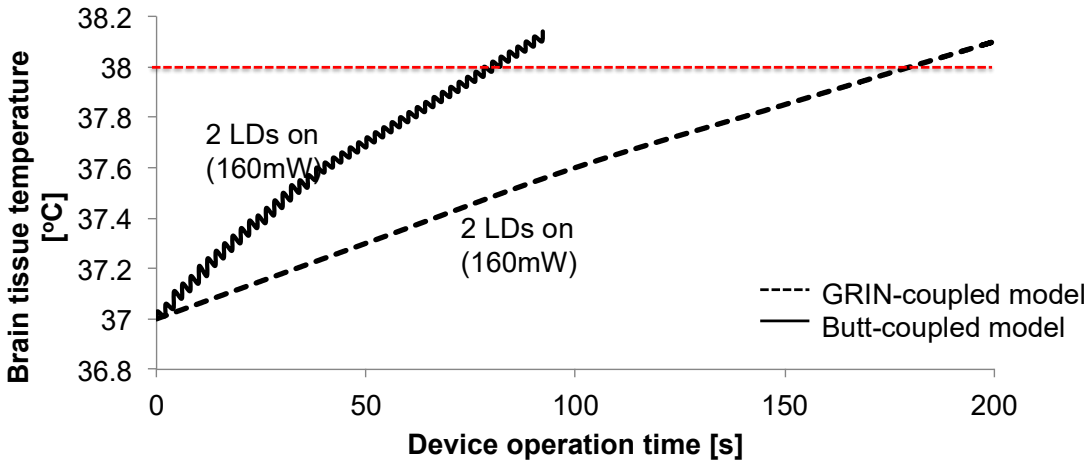

Figure 3-5. Tissue temperature rise over time for models shown in **Figure 3-4**(a) and (b).

just above their threshold current (200 ms pulse width, 10% duty cycle), which is more than adequate for most optogenetic circuit-analysis applications [13]. The maximal temperature of the ILDs themselves (after 190 s at 10% duty cycle) is 50.4°C, which is within the specified safe operational temperature [22]. In an extreme

case, when ILDs are driven by DC current, the continuous device operation time is reduced to 45 s, with a maximal ILD temperature of 52.4°C.

The results also show that a GRIN-coupled design (**Figure 3-4a**) prolongs device operation time more than 2-fold as compared to a conventional design (**Figure 3-4b**). This has a critical influence on the thermal budget when scaling the dual-ILD/single-shank device to multi-shank probes. The thermal design for scaled-up multishank probes is shown in Chapter 5.

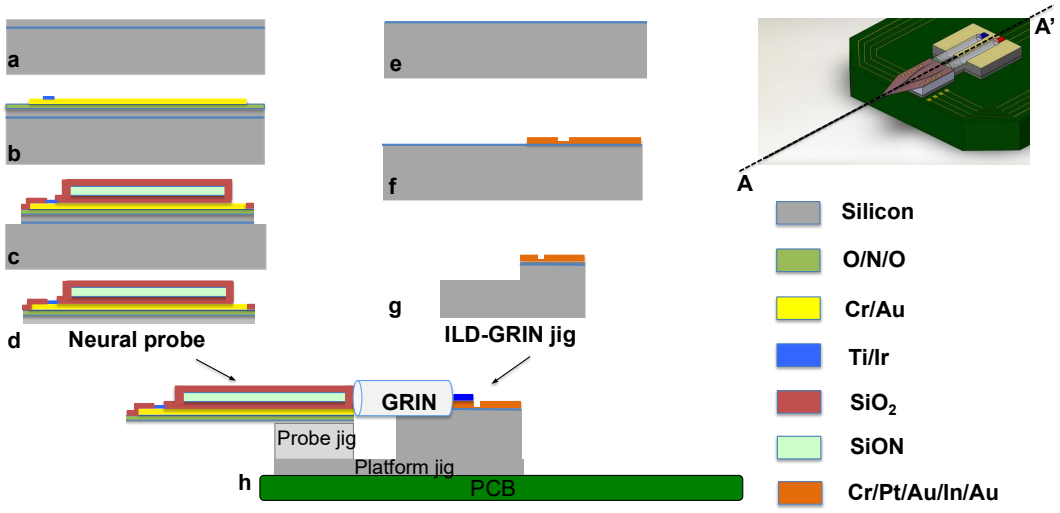

Figure 3-6. Optoelectrode fabrication and assembly on a PCB. Device fabrication along A-A'. (a) Begin probe fabrication on a <100> silicon-on-insulator (SOI) wafer with a 22 µm-thick silicon top layer; (b) LPCVD O/N/O stack deposition; lift-off of Cr/Au, Cr/Au and Ti/Pt/Ir; (c) deposition and patterning of PECVD (plasma-enhanced chemical vapor deposition)-grown waveguide films; dry plasma etching and wet etching; (d) front-side DRIE, backside thinning for release; (e) Begin ILD-GRIN fabrication on a <100> silicon wafer with 2 µm-thick top oxide; (f) deposition and pattering of of Cr/Pt/Au and In/Au; (g) front side DRIE and dicing for release; and (h) final assembly of device components on PCB.

3.3 Methods

3.3.1 Fabrication

Our modular fabrication process follows Michigan probe microfabrication technology [3], [23], [24]. The neural probe fabrication (**Figure 3-6a-d**) was started

on a Silicon-on-Insulator (SOI) wafer with 22 µm thick device layer (**Figure 3-6a**). An LPCVD (low-pressure chemical vapor deposition)-grown silicon dioxide/silicon nitride/silicon dioxide film stack (O/N/O stack, 0.7 µm total thickness) for stress

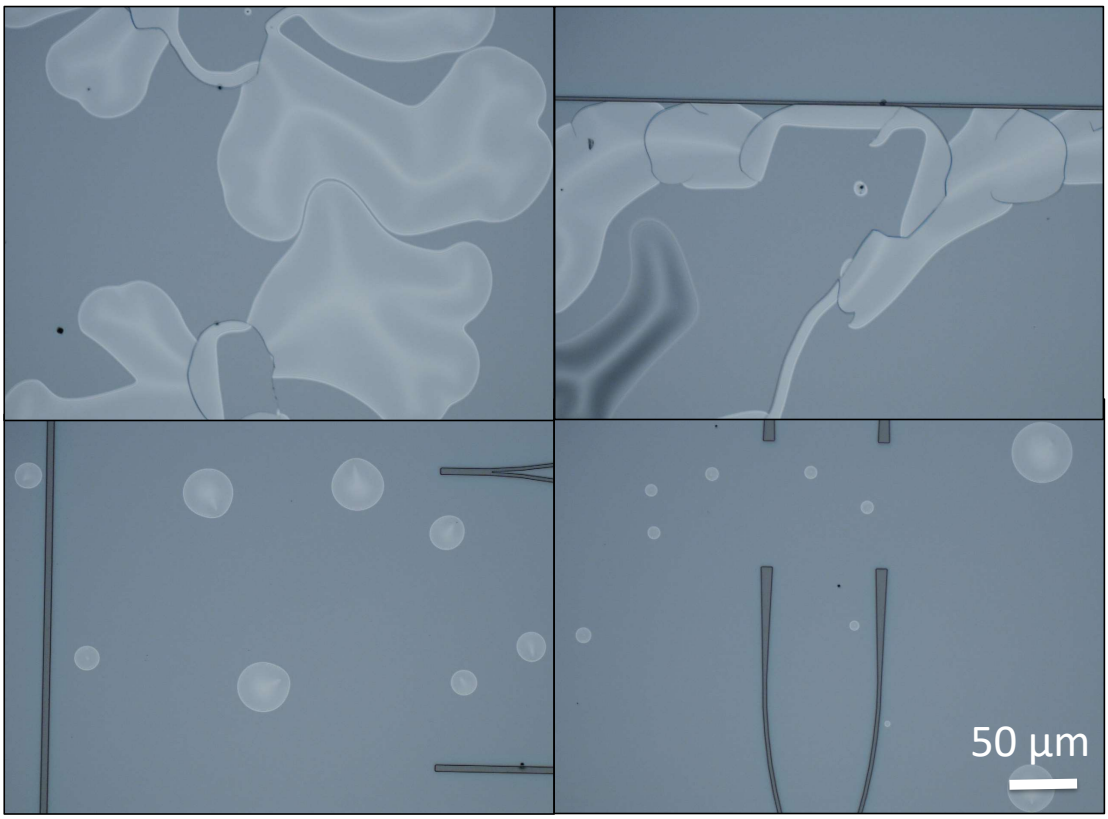

Figure 3-7. Compressive stress and peel-off visible after waveguide stack deposition and patterning step (**Figure 3-6c**) on a silicon wafer if no LPCVD O-N-O stack is deposited underneath waveguide films (**Figure 3-6b**).

compensation and electrical insulation. (**Figure 3-7** shows peeling off of waveguide films under compressive stress if LPCVD stress compensation stack is not deposited underneath). This was followed by lift-off of Cr/Au, Cr/Au and Ti/Pt/Ir for interconnection lines, bond pads and low-impedance electrode sites, respectively (**Figure 3-6b**). A 500 Å-thick aluminum oxide film was deposited under the waveguide films as an etch-stop, avoiding potential damage to the metal surfaces underneath. PECVD (plasma-enhanced chemical vapor deposition)-grown 2 µm thick

silicon dioxide (RI=1.46), 7 μm thick silicon oxynitride (RI=1.52), and another 2 μm thick silicon dioxide (RI=1.46) were deposited and patterned as waveguide lower cladding, core and upper cladding, respectively (**Figure 3-6c**). Dielectric waveguides form an attractive solution for integrated biomedical optics [3], [24], [25]. Unlike polymers, dielectrics are resistant to ionic and enzymatic environments, providing less *in vivo* degradation [26], [27]. In contrast to some polymer waveguides (SU-8, PDMS), they do not absorb light in the UV-blue range [28]–[30]. Since the RI of the waveguide films determines the NA of the waveguide, the PECVD processes were carefully optimized to tune the waveguide NA while maintaining film stress (72 MPa tensile for silicon oxynitride and 180 MPa compressive for silicon dioxide, respectively) and uniformity (<1%) over the entire 4-inch wafer surface. The dielectric waveguide films deposited in this process flow also serve as a top insulation layer for the metals deposited in the previous steps. This next step consisted of dry plasma etching of silicon dioxide and wet etching of 500 Å-thick aluminum oxide (in buffered hydrogen fluoride solution) to open contacts for bond pads and electrode sites. The probe shape was defined by reactive-ion etching from the front side of the wafer and then released using reactive-ion etching from the wafer backside (**Figure 3-6d**). **Figure 3-8** shows microscope images of the probe tip following several key fabrication steps shown in **Figure 3-6a-d. Figure 3-9** shows various probe tip designs that were included in the design masks. The design in **Figure 3-9a** was used for all final assemblies and animal tests. The design in **Figure 3-9b** has metal traces running under the waveguide for more compact routing of traces and waveguides. Successful fabrication of this design was verified; however optical and electrical characterization

is required in future to verify if the routing of metal lines under the waveguide has consequences on optical loss and noise artifacts. The design in **Figure 3-9c** had no patterned waveguides on the probe and was used for stress characterization.

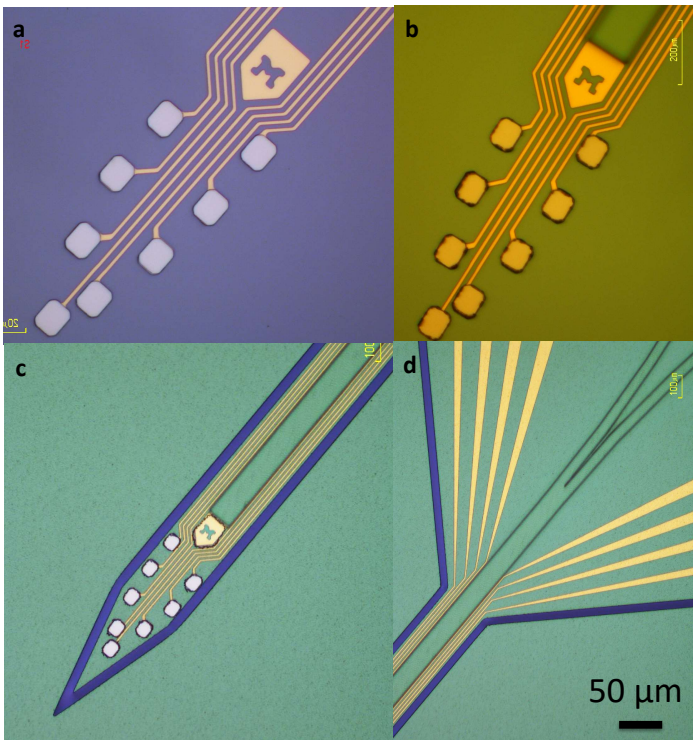

Figure 3-8. The microscope images of the probe following several key fabrication steps shown in **Figure 3-6**: (a) liftoff of Cr/Au interconnects and bond pads and Ti/Pt/Ir electrodes; (c) deposition and patterning of SiO_2/SiON/SiO_2 waveguide stack following by contact opening of Ir electrodes; and (c, d) front DRIE of Si substrate to define probe shank perimeter.

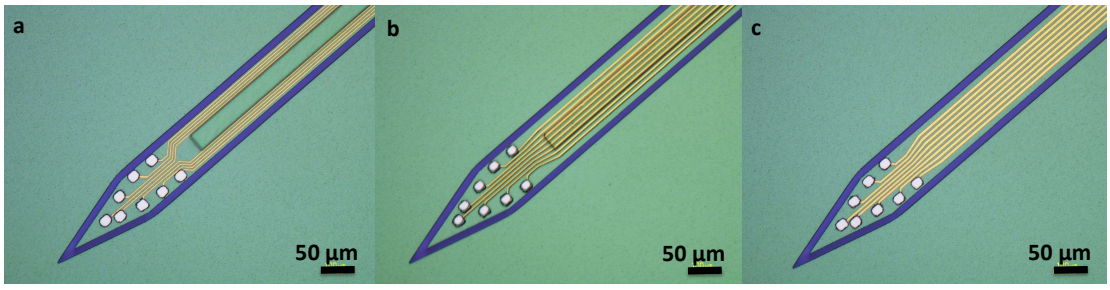

Figure 3-9. Other probe tip designs included in the mask design. (a) With no M-reflector in front of the waveguide tip. (b) Metal interconnects running beneath the waveguide. (c) Shank with no waveguide used as a test design for stress calculations.

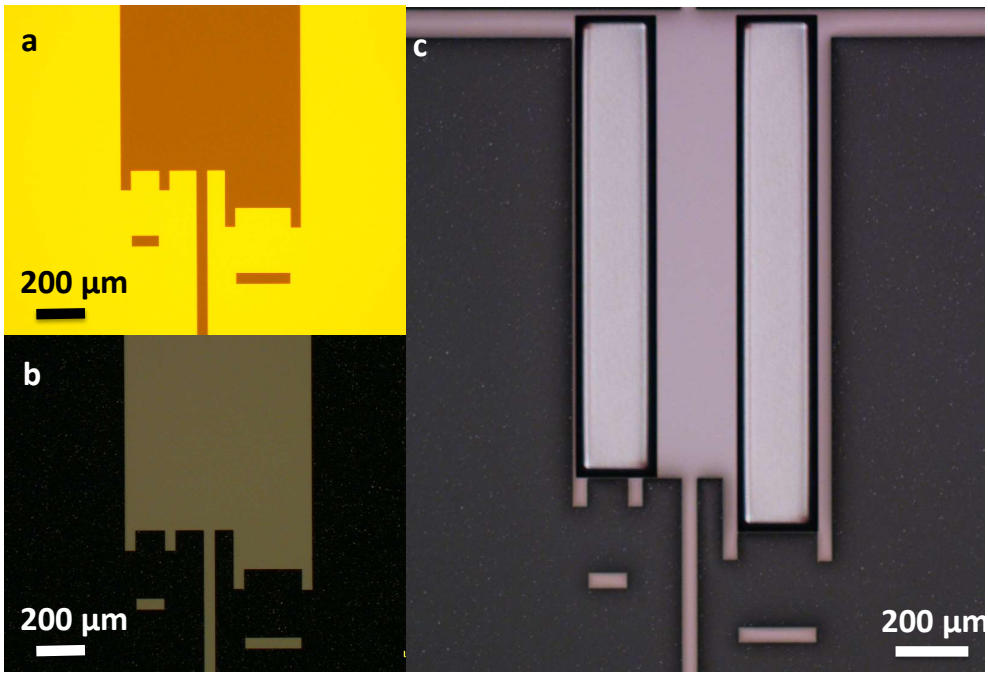

Figure 3-10. The microscope images of the ILD-GRIN jig following key fabrication steps shown in **Figure 3-6**: (a) liftoff of Cr/Pt/Au for defining wire bond pads on boundaries of ILD-GRIN jig; (b) liftoff of In/Au for defining eutectic metal stack for ILD flip-chipping; and (c) DRIE of GRIN slots in front of the ILD placement marks.

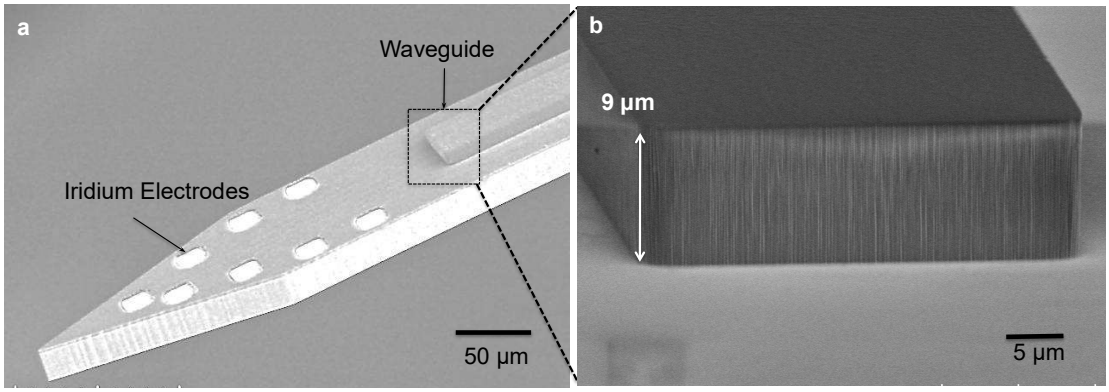

Figure 3-11. (a) Fabricated neural probe with monolithically-integrated dielectric waveguide and iridium electrodes in Buzsaki8 configuration. (b) High magnification SEM image of the dielectric waveguide tip (7 µm core with 2 µm top and 2 µm bottom cladding) fabricated on the neural probe shank.

ILD-GRIN jig fabrication was carried out as shown in **Figure 3-6e-g**. It was started on a <100> silicon wafer with 2 µm-thick top oxide (**Figure 3-6e)**. This was followed by deposition and pattering of metal stack of Cr/Pt/Au and In/Au for ILD

flip-chipping (**Figure 3-6f)**. These metal layers were also used to define alignment marks for ILD placement. Front-side DRIE was used to etch GRIN slots followed by wafer dicing to release ILD-GRIN jigs (**Figure 3-6g)**. **Figure 3-10** shows microscope images of the ILD-GRIN jig following key fabrication steps shown in **Figure 3-6e-g. Figure 3-11a** shows the SEM image of the released neural probe, **Figure 3-11b** shows the magnified SEM view of the waveguide structure fabricated on the top of the probe, and **Figure 3-12a** shows the image of released ILD-GRIN jig (without assembled components).

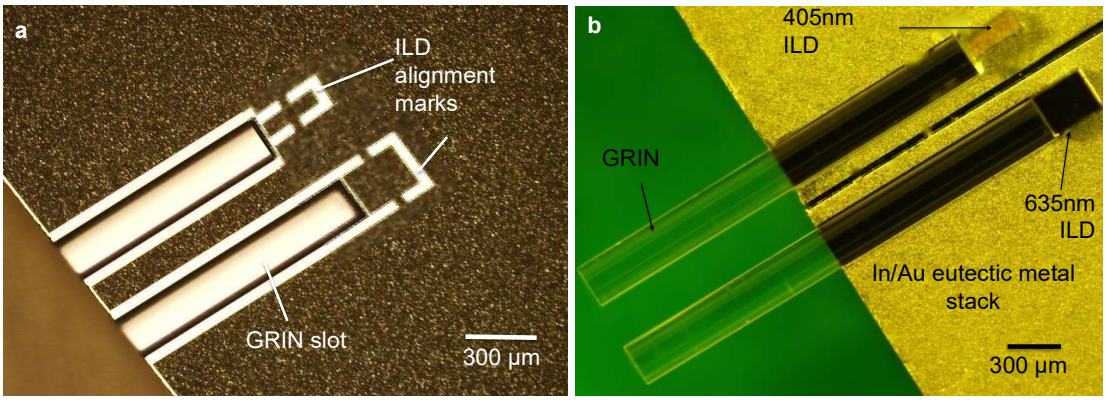

Figure 3-12. Fabricated ILD-GRIN jig (heat sink made of silicon with eutectic metal stack) with defined ILD alignment marks. (b) ILD-GRIN jig with epi-side down flip-chipped 405 nm and 635 nm ILDs and assembled GRIN lenses[1], [3].

3.3.2 Assembly

The optoelectrode was constructed by assembling multiple microfabricated components on a custom designed PCB (**Figure 3-6h**) [3]. The ILDs were aligned and flip-chip bonded onto the released ILD-GRIN jigs. We implemented In-Au eutectic bonding at 200°C to achieve epi-down bonding of the ILDs on ILD-GRIN jigs. In the epi-down configuration, the diodes are flip-chip bonded with the anode facing down, so the heated active region is close to the heat sink, thereby allowing rapid heat

dissipation from active region [31], [32]. Low-temperature indium-gold eutectic bonding was chosen since it protects the ILDs from potential thermal damage at high bonding temperatures. **Figure 3-12b** shows ILD-GRIN jig with assembled components. It is critical to control misalignment of optical components in all dimensions within its respective tolerance ranges. Given device size, this was achieved by photolithographically-defined geometries during microfabrication, and precise assembly techniques with the aid of micromanipulators.

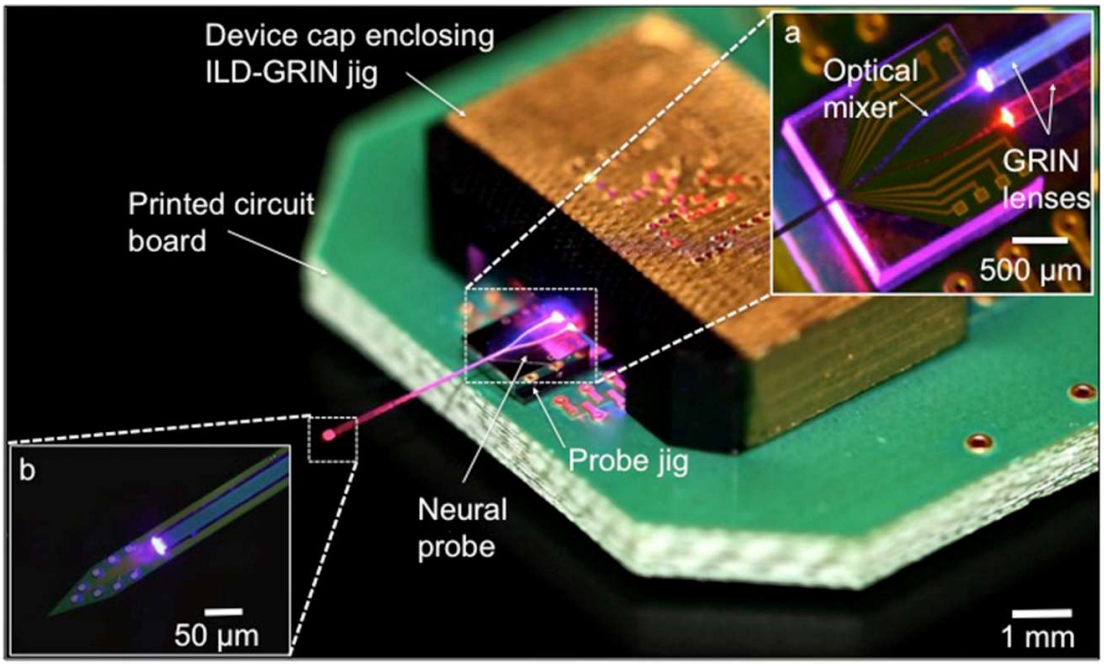

Figure 3-13. Working device prototype assembled on a PCB. Inset (a) shows the enlarged view of the optical mixer at the back end of the probe with GRIN lens coupling into the two arms of the waveguide mixer. Inset (b) shows the enlarged probe tip with color mixed light illuminating at the 30 µm x 7 µm waveguide tip.

During fabrication, all of the designed measures were achieved with ±1 µm precision. The dielectric waveguide core was made relatively tall (7 µm) to increase misalignment tolerances, and a relatively high waveguide NA (0.4228) was designed to reduce loss from angular misalignment. Assembly errors were minimized with

micro-fabricated assembly jigs. The neural probe was supported on a rectangular probe jig to precisely control the vertical alignment between the probe and ILD-GRIN jig. Probe jigs were released via dicing a wafer of a given thickness (no-mask process). These jigs provide modularity in assembly process since a given waveguide probe can be vertically aligned to any ILD height, by simply selecting a jig of a thickness matching the specific ILD-GRIN-PCB assembly. Once aligned in vertical plane, the waveguide mixer was aligned to ILDs in horizontal plane, and GRIN lenses were secured in the GRIN-slots using an index-matching UV-curable epoxy (NOA 61, Norland Products, NJ, USA; RI=1.56). Since the GRIN-waveguide optical junction was found more susceptible to angular misalignment errors, index-matching was not used at this junction. The entire ILD-GRN assembly was enclosed in a micromachined light-weight delrin cap (**Figure 3-13**; Delrin acetal resin, McMaster-Carr, Aurora, OH, USA), designed to serve three functions: (1) block the uncoupled light escaping from optical junctions and prevent it from reaching the unintended locations on brain surface; (2) facilitate convective cooling during device operation via air holes drilled on the cap; and (3) provide electrical shielding between ILDs and recording sites using a grounded 2000 Å thick gold-sputtered film. The assembled devices were wire-bonded on the PCB, which was designed to minimize the capacitive coupling noise between the light sources and recording traces. Two Omnetics connectors (A79006-001 and A790022-001, Omnetics Connector Corporation, Minneapolis, MN, USA) were used for electrical interfacing with external current sources and head stages. **Figure 3-13** shows the fully-assembled assembled working prototype of the device.

3.4 *In vitro* device characterization

3.4.1 ILD efficiency

An effective diode packaging solution can help to quickly dissipate the excessive heat generated in the diode to its surroundings and enhance device reliability. We efficiently managed the heat dissipation from the ILDs to the ILD-GRIN jig (heat sink) and to the PCB. The anode of the epi-side-down bonded ILDs quickly diverted the thermal flux from the diodes to the designated heat sink. The ILD cathodes were grounded (via wirebonds and thermal conductive epoxy) to the ground plane of the PCB.

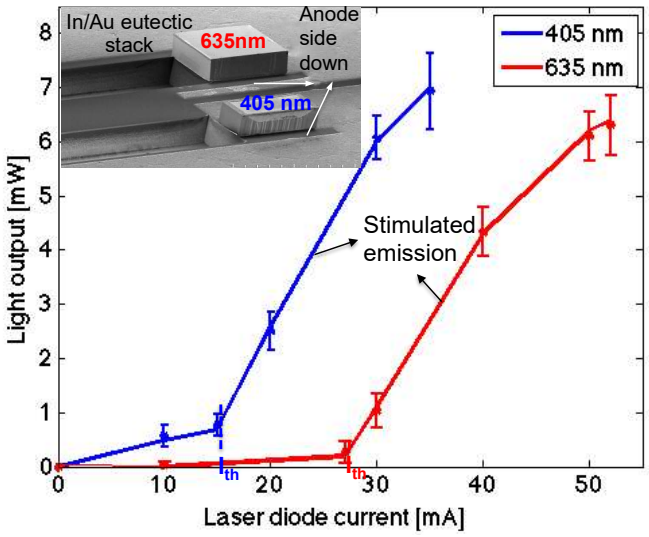

Figure 3-14. Light output-current (L-I) characteristics for epi-side down flip-chipped 405nm and 635nm ILDs (N=10, data points show the mean of the collected data, and error bars represent the standard deviation). The inset shows an SEM image of the eutectic bonded ILDs.

The effectiveness of an ILD assembly is evaluated from its wall-plug efficiency (or radiant flux), which is the efficiency at which the diode assembly converts input electrical power into output optical power. We measured a wall-plug efficiency of 4.48% (for 405 nm) and 5.49% (for 635 nm) for packaged ILDs (**Figure 3-14**). A

bench-top laser driver from Arroyo Instruments was used to drive the ILDs (4201-DR, Arroyo instruments) for characterization.

3.4.2 System optical loss

We quantified optical losses in each part of the system separately: (1) coupling loss at the ILD-GRIN and GRIN-waveguide junctions; (2) radiation loss in the bends and corners of the optical mixer; and (3) propagation losses through the waveguide. Measurement using the direct cut-back method was used to evaluate propagation loss per unit length of as a straight waveguide (**Figure 3-15**). The observed slope of the linear fit, 0.5 dB/mm, gives the waveguide propagation loss. The y intercept (at 0 mm length) of the linear fit, 1.76 dB, gives the total coupling (including Fresnel) loss between the GRIN lens and waveguide, including back reflection at the tip of the waveguide. The coupling loss from ILD to GRIN output was separately estimated as 0.5±0.1 dB (mean ± s.d., N=5) by comparing optical power at ILD (635 nm) and ILD-GRIN outputs. Radiation losses from straight channel waveguides are generally negligible for well-confined modes but may increase in waveguide bends. Our mixer geometry has two bends per light path, and we measured radiation losses of 1.4±0.3 dB (mean ± s.d., N=5) when coupled to 635 nm ILD source. The summed losses of all sources measured for 635 nm light during bench testing was 7.18±0.22 dB for the complete waveguide length (7.04 mm). However, the optical loss measured for packaged devices (**Figure 3-13**) was 11.7±1.1 dB and 9.9±0.7 dB (mean ± s.d., N=5) for 405 nm and 635 nm, respectively, which is ~27% higher than estimated values from experimental devices. This may be mainly due to misalignment in the micro assembly of optical components on a common substrate PCB in the packaged

devices. Nevertheless, the experimental range of total optical loss of 9.2-12.8 dB is, to the best of our knowledge, the lowest reported to date for diode-coupled optoelectrodes, allowing a total optical efficiency of 5.2-12%. Previous work on ILD-coupled SU-8 waveguides reported ~30 dB loss with only one integrated wavelength (650 nm) [33]. Other work reported a multicolor diode assembly with 26 dB loss for blue (465 nm) LEDs and 13 dB loss for red (639 nm) ILDs coupled into 50 µm (core diameter) fibers [13]. Other efforts reported comparable optical losses for a single wavelength, yet with high-power DPSS (diode-pumped solid-state) based systems[24], [25]. Our packaged device yielded, when coupled to a 6 mW ILD, an average output intensity of 1928 mW/mm^2 (405 µW output power) for 405 nm and 2905 mW/mm^2 (610 µW) for 635nm at the waveguide tip.

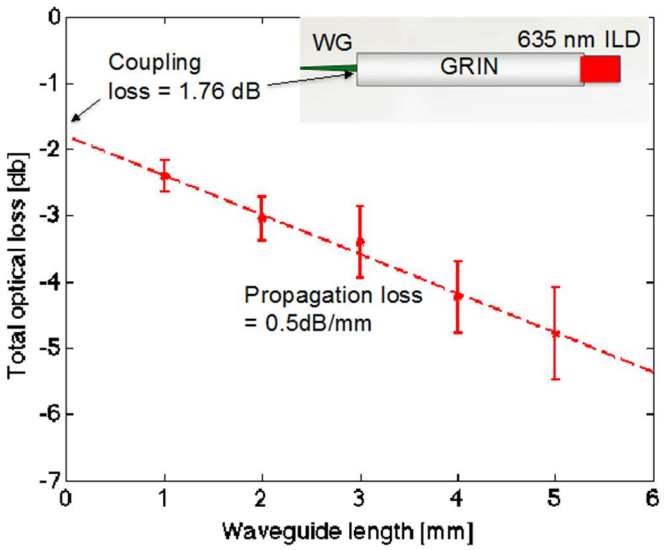

Figure 3-15. Direct cut-back measurement for identical straight waveguide sets (N=5, data points show the mean of the collected data, and error bars represent the standard deviation). The optical output for 5 sets of straight waveguides fabricated on the same substrate (each set consisting of five different waveguides: 5 mm, 4 mm, 3 mm, 2 mm and 1 mm long; all coupled to 635 nm LDs) was measured, and the total output loss in dB (difference between source power and measured power at waveguide output) was plotted as a function of waveguide lengths. The plotted data was used to calculate propagation loss in dB/mm (0.5 dB/mm for 635 nm and 0.63 dB/mm for 405 nm) and coupling loss in dB (1.76 dB for 635 nm and 1.92 dB for 405 nm) at GRIN-waveguide interface.

3.4.3 Optical misalignment tolerance analysis

Most alignment errors in micro-optics come from component mismatch and assembly misalignment. Using ray-tracing modeling, we investigated the effect of misalignment tolerances on the GRIN-based optoelectrode; we then compared the simulation results with bench tests (**Figure 3-16**) [3]. Among all optical coupling interfaces, the ILD-GRIN coupling junction is the most tolerant. Large misalignment margins were obtained when GRIN lens was misaligned in X and Y (lateral symmetrical GRIN axes) or Z (longitudinal) axes with respect to the ILD (**Figure 3-17a-b**), allowing up to ±115 µm lateral and 20 µm longitudinal misalignment with < 10% relative optical loss. This gives a huge error margin in microfabrication when defining GRIN slots. **Figure 3-18a-c** shows normalized coupling when the mixer waveguide (WG) is misaligned with respect to the ILD-GRIN assembly in the X, Y and Z-axes, respectively. Here, the axis most sensitive to misalignment is Y (**Figure 3-18b**), where tolerance is dictated by the height of the WG core.

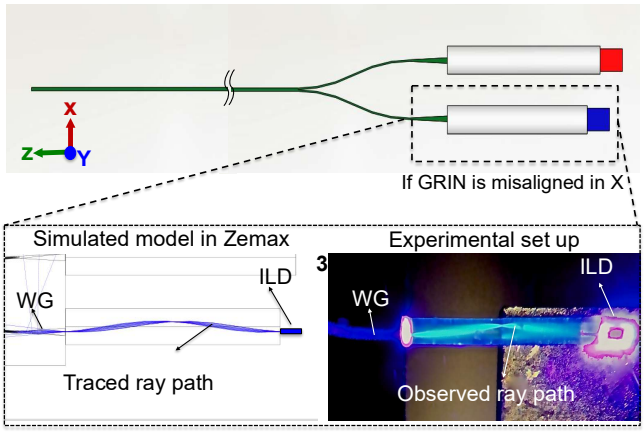

Figure 3-16. Schematic of optical model model components showing ILDs and GRINs coupled to the waveguide mixer (WG). Agreement between simulated models in Zemax and experimental results obtained when GRIN lens is intentionally misaligned by 25µm (in X-axis) while ILD and GRIN are kept stationary. The traced ray path in Zemax matches very well the observed ray path in the assembled prototype device.

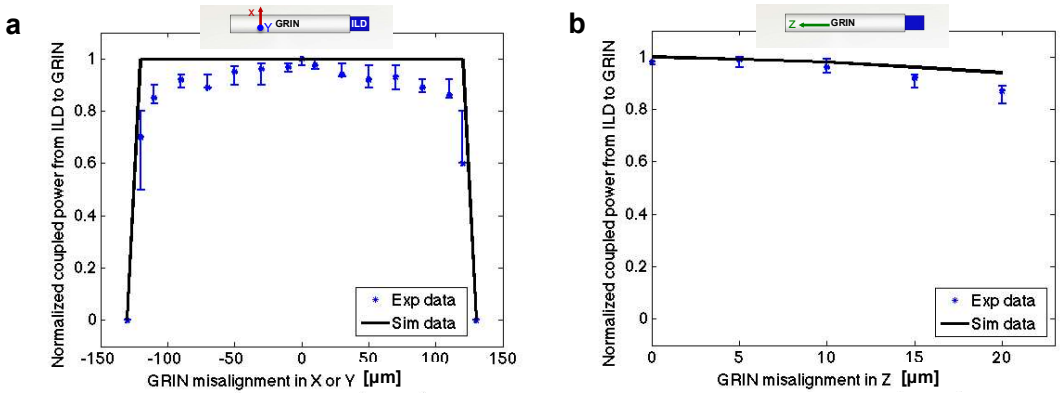

Figure 3-17. Alignment tolerance analysis for ILD-GRIN coupling when ILD is stationary but GRIN is (a) laterally misaligned in X or Y-axis (because GRIN lens is symmetrical about X and Y axis, misalignment in either directions leads to the same results); and (b) longitudinally misaligned in Z-axis.

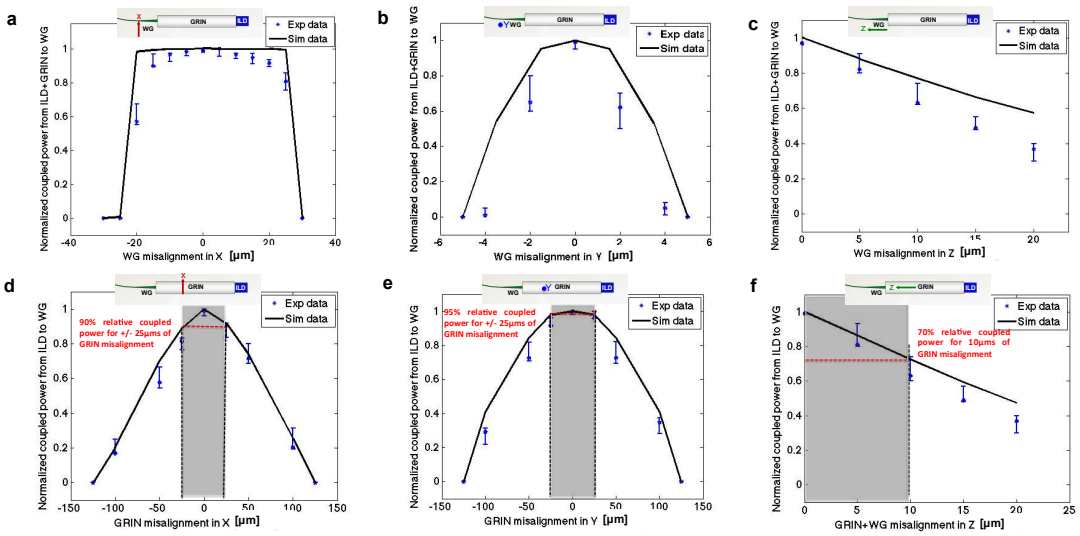

Figure 3-18. (a-c) Alignment tolerance analysis for ILD-GRIN-WG coupling when ILD and GRIN are perfectly aligned and stationary but WG is (a) laterally misaligned in X-axis; (b) laterally misaligned in Y-axis; and (c) longitudinally misaligned in Z-axis. (d-f) Alignment tolerance analysis for ILD-GRIN-WG coupling when ILD and WG are perfectly aligned and stationary but GRIN is (d) laterally misaligned in X-axis; (e) laterally misaligned in Y-axis; and (f) longitudinally misaligned in Z-axis (when WG displaces in Z-axis, WG displaces in Z-axis too).

In order to accurately control the vertical GRIN-WG alignment, the emission point of an ILD should be aligned to the center of a WG cross-section by selecting the precise height of the probe jig. Since this jig is easily replaceable, the GRIN lens can

be reliably and reproducibly positioned between the ILD and WG. Even if the GRIN lens is misaligned at this step, relatively large normalized output power of 90%, 95% and 70% can be achieved within a tolerance of ±25 μm in X and Y axes and 10 μm in Z-axis, respectively (**Figure 3-18d-f**). These alignment margins can be easily accomplished during the assembly process. The inset for all graphs shows the schematic of the respective coupling interface, depicting the axis and direction of misalignment. Data points show the median of the collected data (N=3), and error bars represent the range.

3.4.4 Electrical impedance measurements

Impedance and electrical noise of recording channels were measured in phosphate buffered saline (PBS, 0.1 M, Fisher Scientific, Hampton, New Hampshire, USA) with an RHD2164 amplifier board connected to an RHD2000 Evaluation System (Intan technologies, Los Angeles, CA, USA). The average impedance of recording sites (140 μm^2) was 410±30 kΩ with 68±2° phase at 1 kHz (mean ± s.d., N=3 devices, 8 sites each), which is sufficiently low to record neural signals with high signal-to-noise ratio. The average baseline noise picked up by the recording channels in absence of light stimulation was 8 μV peak-to-peak.

3.5 *In vivo* electrophysiological results

3.5.1 Bidirectional control of a single neuron

The electrophysiological procedures for animal experiments are listed in **Appendix B**. We inserted an 8-site dual-ILD silicon probe into the CA1 pyramidal cell layer of urethane-anesthetized mice. Spontaneous neural activity, including high-frequency ripple oscillations [34] and multi-neuronal spiking (**Figure 3-19**, top), was

observed on all 8 channels. When trains of 405 nm light pulses (50 ms, 1 pulse/s, 10 pulses/train; 30 mA, 100 µW at the waveguide tip) were applied; the recorded pyramidal cells (PYR) increased their spiking probability, consistent with ChR2 expression driven by the CaMKII-Cre driver in these animals (**Figure 3-19**, middle). When the trains of 635 nm light pulses (200 ms, 1 pulse/s, 10 pulses/train; 40 mA, 370 µW at the waveguide tip) were applied through the same waveguide without moving the probe, the same cells reduced their spiking rate (**Figure 3-19**, bottom), consistent with eArch expression in in PYR in these animals.

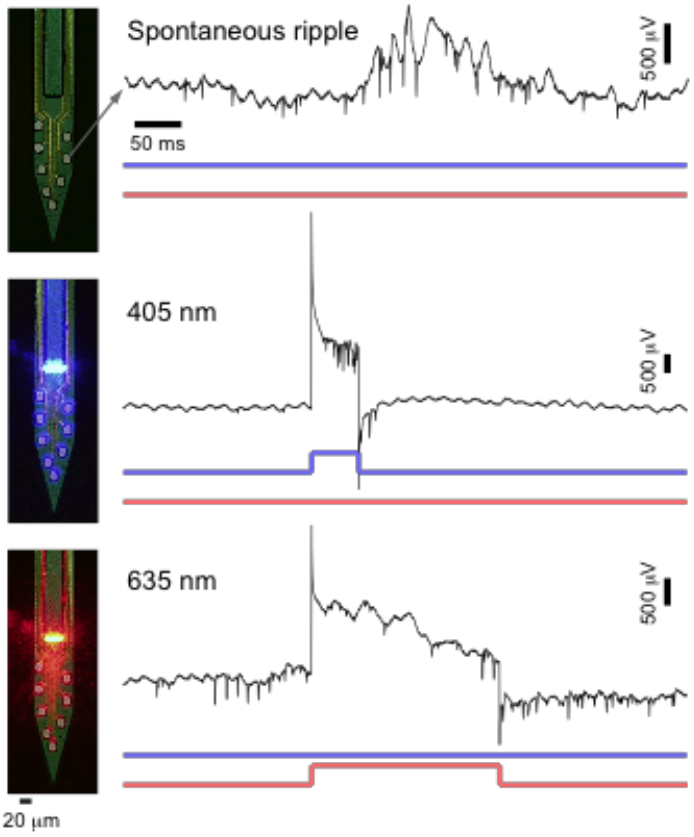

Figure 3-19. Wide-band (0.3-10,000 Hz) traces recorded from CA1 pyramidal cell layer of a urethane-anesthetized mouse expressing ChR2 and eArch3 under the CaMKII promoter. Top, spontaneous spiking and ripple activity; middle, activity from the same recording site during a 100 µW pulse (power at the waveguide tip) of 405 nm light; bottom, recording from the same site during a 370 µW pulse of 635 nm light. Note spontaneous, induced, and silenced spiking, respectively; and stimulus-locked artifacts during ILD driving.

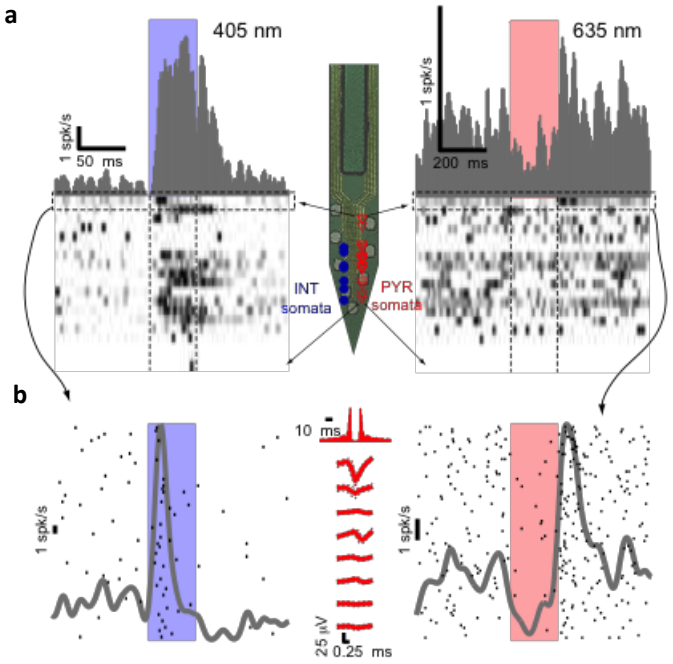

Figure 3-20. ILD-GRIN probes enable bi-directional control of pyramidal cells in the intact mouse. Spiking activity from 19 well-isolated pyramidal cells (PYR) recorded simultaneously from CA1 (same animal and session as in **Figure 3-19)**. Inset shows the vertical location of PYR (red triangles) and interneuron (INT, blue circles) somata relative to the probe sites. Bottom panels: heat maps showing, in each row, a peri-stimulus time histogram (PSTH) for one PYR; each PSTH was scaled to the 0-1 range. Higher rows show PSTHs for PYR with somata closer to the waveguide tip. PSTHs for simultaneously recorded INT are not shown. Most PYR (11/19; 58%) increased their spike rate ($p<0.05$, Poisson test) during 405 nm light; 4/19 (21%) decreased their rate during 635 nm light.

We quantified the cell-specific effect of light on a group of PYR (n=19) recorded simultaneously from CA1 (**Figure 3-20a**, inset shows the relative location of PYR and interneuron [INT] somata). Each cell was assessed for spike rate during the 405nm light pulse, compared to baseline spiking rate (in the lack of any light). Most (11/19; 58%) of the cells increased their spike rate ($p<0.05$, Poisson test), with a median gain (spike rate during light divided by baseline rate) of 15.1 and a median latency of 15 ms (see also **Figure 3-20a**, left). Using the same approach, the same cells were also assessed for spike modulation during 635 nm light: 4/19 cells (21%)

exhibited a consistent rate decrease ($p<0.05$, Poisson test), with a median gain of 0.11 and a median latency of 54 ms (**Figure 3-20a**, right). One PYR, the one closest to the waveguide (estimated distance from waveguide tip to soma, 75 μm), exhibited both consistent rate increase and rate decrease ($p<0.001$ for both; **Figure 3-20b**).

3.5.2 Control of different cell types

In addition to controlling pyramidal cells in CA1 of hippocampus, we also controlled PV interneuron cells (in different animals). Similar results were observed in CA1 of a mouse expressing ChR2 specifically in PV-cells (3/3 simultaneously-recorded INT consistently driven by 50 ms pulses of 405 nm light, $p<0.05$, Poisson test; median gain, 3.2; **Figure 3-21, Figure 3-22**), emphasizing the wide range of potential ILD-GRIN probe applications.

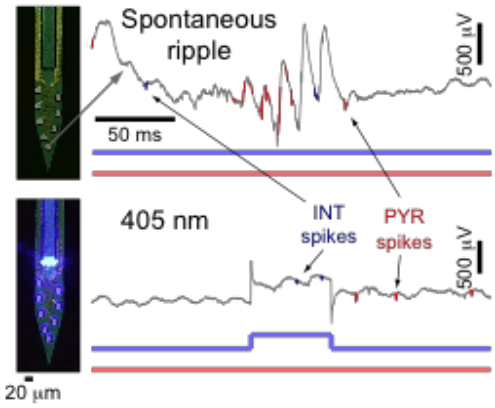

Figure 3-21. Wide-band (0.3-10,000 Hz) traces recorded from CA1 pyramidal cell layer of a urethane-anesthetized mouse expressing ChR2 under the PV promoter. Top panel shows spontaneous spiking and ripple activity. Bottom panel shows activity from the same recording site during a 50 μW pulse (power at the waveguide tip; driving current, 25 mA) of 405 nm light. Note induced INT spikes (blue), suppressed PYR spiking (red), and stimulus-locked artifacts during the light pulse.

3.6 Discussion

Optogenetic devices that use fibered light delivery from a bench-top source

constrain free animal movement, whereas LED-coupled systems yield poor coupling efficiency because of their Lambertian light distribution profile. ILDs offer an attractive solution for optoelectrode design since they are highly compact, provide a directional beam with a wide power range. However, commercial ILD packages are too large to be integrated into high-density micro-scale devices, whereas unpackaged

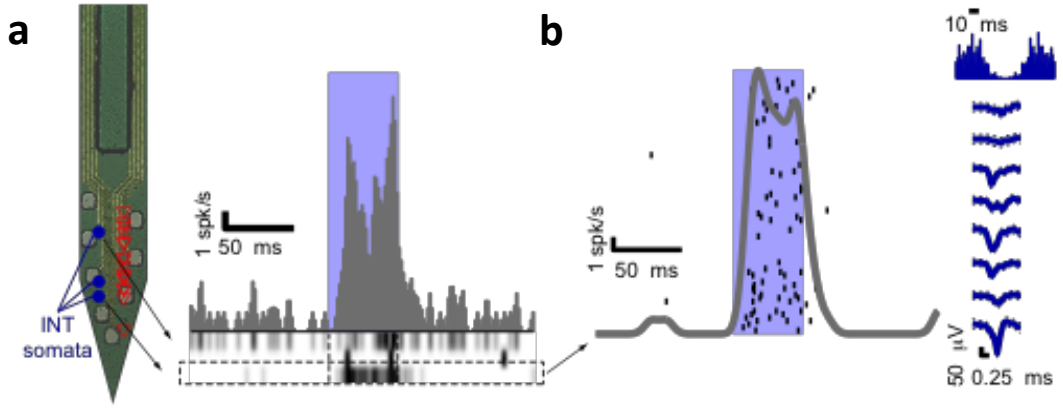

Figure 3-22. (a) Spiking activity from 3 well-isolated INT recorded simultaneously from CA1 (same animal and session as in **Figure 3-21**). Left panel shows the vertical location of the PYR (red triangles) and INT (blue circles) somata relative to the probe sites. Heat maps (bottom right) show, in each row, a PSTH for one INT, scaled to the 0-1 range. Higher rows show PSTHs for INT with somata closer to the waveguide tip. PSTHs for simultaneously recorded PYR are not shown. All three recorded INT increased their spike rate ($p<0.05$, Poisson test) during violet light pulses. (b) Raster plots for a single INT, exhibiting a 6.8-fold rate increase during 405 nm light pulses ($p<0.001$, Poisson test). Each black tick marks the occurrence of one spike. Gray curve shows PSTH (non-scaled; generated by summing spike times and convolving with a Gaussian kernel, SD=5 ms). Plots at right show the auto-correlation histogram (top) and spike waveform (mean and SD) in the lack of any illumination. Note robust activation during violet light pulses.

ILD chips have divergent output beams and are also easily damaged by electrostatic pickup or excessive heat. Here, these issues were addressed by incorporating unpackaged ILD chips in a fiberless, lightweight micro-fabricated module that enabled precise assembly of optical components and facilitated protecting electrical and thermal components at the device backend. With the use of GRIN lenses as the

optical coupling medium, we were able to achieve total optical efficiency range of 5.2-12% for the assembled working prototypes (the highest reported efficiency for diode-coupled optoelectrodes to date) while facilitating thermal dissipation at device backend and providing adequate thermal insulation to the tissue.

The electrophysiological data indicated three clear results. First, the existence of a 9 μm high waveguide over the probe surface does not hinder neuronal recordings [11], as spontaneous activity was recorded in each and every animal. Second, the application of 100 μW of 405 nm light was sufficient to consistently drive spiking in ChR2-expressing PYR with somata up to about 190 μm from the waveguide tip, despite the small cross-section of the waveguide core (7 x 30 μm). Although large waveguide cores can transmit more light, small cores help to confine light, resulting in higher light intensity for a given input power. Similar results were observed in CA1 of a mouse expressing ChR2 specifically in PV-cells (3/3 simultaneously-recorded INT consistently driven by 50 ms pulses of 405 nm light, $p<0.05$, Poisson test; median gain, 3.2), emphasizing the wide range of potential ILD-GRIN probe applications. Third, red light power of about 400 μW (range, 50-500 μW) – despite yielding high intensity at the waveguide tip – was partially effective at silencing spiking of nearby eArch3 neurons. This is consistent with previous observations indicating that optical silencers require higher light intensity than ChR2 [13], [15], [16]. The activation spectrum of eArch3 is blue-shifted relative to eHalo3 [16], and in our previous work, 0.4-1.3 mW of 561 nm light was required to silence PYR and suppress ripples in mouse CA1 using diode-probes [35]. These considerations suggest that potentially mitigated by the development of red-shifted silencers [36], increased

red light intensity is required for robust silencing of eArch3 *in vivo* with the ILD-GRIN probes.

3.7 Conclusion

In this chapter, we discussed and implemented successful fabrication, assembly, and characterization of the first monolithically-integrated fiber-less ILD-GRIN coupled optoelectrode device for *in vivo* circuit analysis [3]. The dielectric optical mixer waveguide integrated onto the neural probe enabled wavelength mixing at a common waveguide port, providing adequate light intensities to activate and silence local populations of same and different genetically targeted neurons. Optimal thermal packaging was achieved via efficient ILD assembly and GRIN-facilitated thermal insulation. The fully packaged optoelectrodes were tested in anesthetized mice and recorded high-quality neurophysiology, demonstrating device feasibility. This fully-integrated approach demonstrates spatial precision and scalability needed to enable independent activation and silencing of the same or different groups of neurons in dense brain regions while simultaneously recording from them.

References

[1] K. Kampasi, J. Seymour, K. Na, K. D. Wise, and E. Yoon, "Fiberless multicolor optoelectrodes using Injection Laser Diodes and Gradient-index lens coupled optical waveguides," in *Proceedings of the 18th International Conference on Solid-State Sensors, Actuators and Microsystems (TRANSDUCERS)*, 2015, pp. 273–276.

[2] K. Kampasi, J. Seymour, K. Na, K. D. Wise, and E. Yoon, "Fiberless multicolor optoelectrodes for neural circuit analysis," in *Society for Neuroscience (SfN)*, 2015.

[3] K. Kampasi, E. Stark, J. Seymour, K. Na, H. G. Winful, G. Buzsáki, K. D. Wise, and E. Yoon, "Fiberless multicolor neural optoelectrode for in vivo circuit analysis," *Sci Rep, Nat. Publ. Gr.*, vol. 6, p. 30961, 2016.

[4] K. Kampasi, E. Yoon, and J. P. Seymour, "Multicolor neural optoelectrode," US Patent 15 185 209, 2016.

[5] M. Riedl, *Optical Design Fundamentals for Infrared Systems, Second Edition*. Bellingham, WA: SPIE Press, 2001.

[6] W. J. Smith, *Modern Optical Engineering*. Tata McGraw-Hill Education, 1966.

[7] M. Riedl, *Optical Design Fundamentals for Infrared Systems, Second Edition*. SPIE Press, 2001.

[8] R. G. Hunsperger, *Integrated Optics*. Springer-Verlag New York, 1984.

[9] E. A. J. Marcatilli, "Bends in optical dielectric waveguides," *Bell Syst. Tech. J.*, vol. 48, no. 7, pp. 2103–2132, 1969.

[10] A. M. Aravanis, L.-P. Wang, F. Zhang, L. a Meltzer, M. Z. Mogri, M. B. Schneider, and K. Deisseroth, "An optical neural interface: in vivo control of rodent motor cortex with integrated fiberoptic and optogenetic technology.," *J. Neural Eng.*, vol. 4, no. 3, pp. S143–S156, Sep. 2007.

[11] A. V Kravitz, B. S. Freeze, P. R. L. Parker, K. Kay, M. T. Thwin, K. Deisseroth, and A. C. Kreitzer, "Regulation of parkinsonian motor behaviours by optogenetic control of basal ganglia circuitry.," *Nature*, vol. 466, no. 7306, pp. 622–6, Jul. 2010.

[12] S. Royer, B. V. Zemelman, M. Barbic, A. Losonczy, G. Buzsáki, and J. C. Magee, "Multi-array silicon probes with integrated optical fibers: Light-assisted perturbation and recording of local neural circuits in the behaving animal," *Eur. J. Neurosci.*, vol. 31, no. 12, pp. 2279–2291, 2010.

[13] E. Stark, T. Koos, and G. Buzsáki, "Diode probes for spatiotemporal optical

control of multiple neurons in freely moving animals.," *J. Neurophysiol.*, vol. 108, no. 1, pp. 349–63, Jul. 2012.

[14] G. Nagel, T. Szellas, W. Huhn, S. Kateriya, N. Adeishvili, P. Berthold, D. Ollig, P. Hegemann, and E. Bamberg, "Channelrhodopsin-2, a directly light-gated cation-selective membrane channel.," *Proc. Natl. Acad. Sci. U. S. A.*, vol. 100, no. 24, pp. 13940–5, 2003.

[15] V. Gradinaru, F. Zhang, C. Ramakrishnan, J. Mattis, R. Prakash, I. Diester, I. Goshen, K. R. Thompson, and K. Deisseroth, "Molecular and Cellular Approaches for Diversifying and Extending Optogenetics," *Cell*, vol. 141, no. 1, pp. 154–165, 2010.

[16] J. Mattis, K. M. Tye, E. a Ferenczi, C. Ramakrishnan, D. J. O'Shea, R. Prakash, L. a Gunaydin, M. Hyun, L. E. Fenno, V. Gradinaru, O. Yizhar, and K. Deisseroth, "Principles for applying optogenetic tools derived from direct comparative analysis of microbial opsins," *Nat. Methods*, vol. 9, no. 2, pp. 159–172, 2011.

[17] M. M. Elwassif, Q. Kong, M. Vazquez, and M. Bikson, "Bio-heat transfer model of deep brain stimulation induced temperature changes.," *J. Neural Eng.*, vol. 3, no. 4, p. 306, 2006.

[18] K. fei Shen and P. A. Schwartzkroin, "Effects of temperature alterations on population and cellular activities in hippocampal slices from mature and immature rabbit," *Brain Res.*, vol. 475, no. 2, pp. 305–316, Dec. 1988.

[19] P. Andersen and E. I. Moser, "Brain temperature and hippocampal function," *Hippocampus*, vol. 5, no. 6, pp. 491–498, 1995.

[20] M. A. Long and M. S. Fee, "Using temperature to analyse temporal dynamics in the songbird motor pathway.," *Nature*, vol. 456, no. 7219, pp. 189–94, 2008.

[21] F. Wu, E. Stark, P. C. Ku, K. D. Wise, G. Buzsáki, and E. Yoon, "Monolithically Integrated μLEDs on Silicon Neural Probes for High-Resolution Optogenetic Studies in Behaving Animals," *Neuron*, vol. 88, no. 6, pp. 1136–1148, 2015.

[22] H. I. Abdelkader, H. H. Hausien, and J. D. Martin, "Temperature rise and thermal rise-time measurements of a semiconductor laser diode," *Rev. Sci. Instrum.*, vol. 63, no. 3, pp. 2004–2007, 1992.

[23] K. D. Wise, "Silicon microsystems for neuroscience and neural prostheses," *IEEE Eng. Med. Biol. Mag.*, vol. 24, no. 5, pp. 22–29, Sep. 2005.

[24] F. Wu, E. Stark, M. Im, I.-J. Cho, E.-S. Yoon, G. Buzsáki, K. D. Wise, and E. Yoon, "An implantable neural probe with monolithically integrated dielectric waveguide and recording electrodes for optogenetics applications.," *J. Neural Eng.*, vol. 10, no. 5, p. 56012, Oct. 2013.

[25] A. N. Zorzos, E. S. Boyden, and C. G. Fonstad, "Multiwaveguide implantable probe for light delivery to sets of distributed brain targets.," *Opt. Lett.*, vol. 35, no. 24, pp. 4133–5, Dec. 2010.

[26] K. Worhoff, L. T. H. Hilderink, A. Driessen, and P. V Lambeck, "Silicon oxynitride - A versatile material for integrated optics applications," *J. Electrochem. Soc.*, vol. 149, no. 8, pp. F85–F91, 2002.

[27] K. Wörhoff, E. Klein, G. Hussein, and A. Driessen, "Silicon oxynitride based photonics," in *Proceedings of 2008 10th Anniversary International Conference on Transparent Optical Networks, ICTON*, 2008, vol. 3, pp. 266–269.

[28] B. Rubehn, S. B. E. Wolff, P. Tovote, A. Lüthi, and T. Stieglitz, "A polymer-based neural microimplant for optogenetic applications: design and first in vivo study.," *Lab Chip*, vol. 13, no. 4, pp. 579–88, Feb. 2013.

[29] K. Kwon and W. Li, "Integrated multi-LED array with three-dimensional polymer waveguide for optogenetics," in *Proceedings of the IEEE International Conference on Micro Electro Mechanical Systems (MEMS)*, 2013, pp. 1017–1020.

[30] M. Im, I. J. Cho, F. Wu, K. D. Wise, and E. Yoon, "A dual-shank neural probe integrated with double waveguides on each shank for optogenetic applications," *Proc. Annu. Int. Conf. IEEE Eng. Med. Biol. Soc.*, pp. 5480–5483, Jan. 2011.

[31] X. Liu, M. H. Hu, H. K. Nguyen, C. G. Caneau, M. H. Rasmussen, R. W. Davis, and C. E. Zah, "Comparison between epi-down and epi-up bonded high-power single-mode 980-nm semiconductor lasers," *IEEE Trans. Adv. Packag.*, vol. 27, no. 4, pp. 640–646, 2004.

[32] T. Jin and W. Ronnie, *Semiconductor Laser Diode Technology and Applications*. InTech, 2012.

[33] M. Schwaerzle, K. Seidl, U. T. Schwarz, O. Paul, and P. Ruther, "Ultracompact optrode with integrated laser diode chips and SU-8 waveguides for optogenetic applications," in *Proceedings of the IEEE International Conference on Micro Electro Mechanical Systems (MEMS)*, 2013, pp. 1029–1032.

[34] G. Buzsáki, Z. Horváth, R. Urioste, J. Hetke, and K. Wise, "High-frequency network oscillation in the hippocampus.," *Science*, vol. 256, no. 5059, pp. 1025–1027, 1992.

[35] E. Stark, L. Roux, R. Eichler, Y. Senzai, S. Royer, and G. Buzsáki, "Pyramidal cell-interneuron interactions underlie hippocampal ripple oscillations," *Neuron*, vol. 83, no. 2, pp. 467–480, 2014.

[36] A. S. Chuong, M. L. Miri, V. Busskamp, G. A. C. Matthews, L. C. Acker, A. T. Sørensen, A. Young, N. C. Klapoetke, M. A. Henninger, S. B. Kodandaramaiah, M. Ogawa, S. B. Ramanlal, R. C. Bandler, B. D. Allen, C. R. Forest, B. Y. Chow,

X. Han, Y. Lin, K. M. Tye, B. Roska, J. A. Cardin, and E. S. Boyden, “Noninvasive optical inhibition with a red-shifted microbial rhodopsin.,” *Nat. Neurosci.*, vol. 17, no. 8, pp. 1123–9, 2014.

Chapter 4

Noise Artifacts in Fiberless Optoelectrodes

4.1 Introduction

Electromagnetic (EM) fields are generated by electrical sources carrying voltages and currents. EM fields can get undesirably coupled to the nearby victim circuits via mutual capacitance and/or mutual inductance and result in EM interference (EMI). The exact relationship between separation distance between source and victim (d) and field strength (E) is complex and depends on the radiating source, transmitter power, and frequency. In general, field strengths start to diminish with increasing separation between source and victim. At distances greater than a wavelength, these fields fall off in inverse proportion to distance and can be represented approximately as $E = K/d$, where K is the constant dependent on radiating source design, power and frequency [1], [2].

In fiberless optoelectrodes, EM fields are generated by electric traces carrying modulating currents that drive optical sources. The abrupt rise and fall of modulating waveform charges and discharges the stimulating terminals and this sudden change in EM fields, when picked up by the nearby recording traces on the neural probe, induces artifacts in neural data and corrupts it.

4.2 Noise artifacts in first-generation ILD-GRIN optoelectrodes

A limitation of the first-generation ILD-GRIN probes in Chapter 3 was that

local field potential (LFP) exhibited stimulus-locked transients (onset and offset of stimulation pulse) and artifacts (**Figure 3-19**), which are also evident in many other optogenetic studies[3]–[5]. These artifacts are comprised of a fast transient and DC offset with an asymptotic attenuation, features which are consistent with capacitive effects**.** The putative source of artifacts with the ILD-GRIN probes is the presence of capacitive coupling effects in device assembly, via the opening in the shield cap, and via the platform jig/PCB substrate. In the ILD-GRIN optoelectrodes, current carrying ILDs are flip-chip bonded on the ILD-GRIN jig; thus, the entire surface of ILD-GRIN jig can act as a potential source of radiating EM fields, which get coupled to the recording channels on the probe. The resulting EM fields are usually complicated due to the presence of various coupling paths, which do not show up explicitly in the formal circuit design. In this work, we also describe modified assembly techniques, improved shield cap design, and better grounding strategies that were implemented to minimize artifacts in future multi-shank prototypes [6], [7].

4.3 Electrical design for second-generation ILD-GRIN optoelectrodes

4.3.1 Equivalent circuit model

Lumped circuit analysis is proven to be successful for prediction of EMI behaviors [8]–[12]; especially at lower frequencies, where most of the advanced EMI analysis tools fail to converge to produce reliable results. In this section, we describe a lumped circuit model for analysis of EMI coupling paths in a multi-shank optoelectrode design (**Figure 4-1, Figure 4-2)**.

The assembly components (neural probe, probe jig, ILD-GRIN jig and platform jig) along with the ILD current source (EMI source) and recording channels (EMI

victim) were modeled in Cadence SPICE circuit simulator (**Figure 4-3)**. The initial model analysis showed that a coupling capacitance of as small as few fF, from ILD to recording traces, largely dominated the transient magnitude on the recording channel

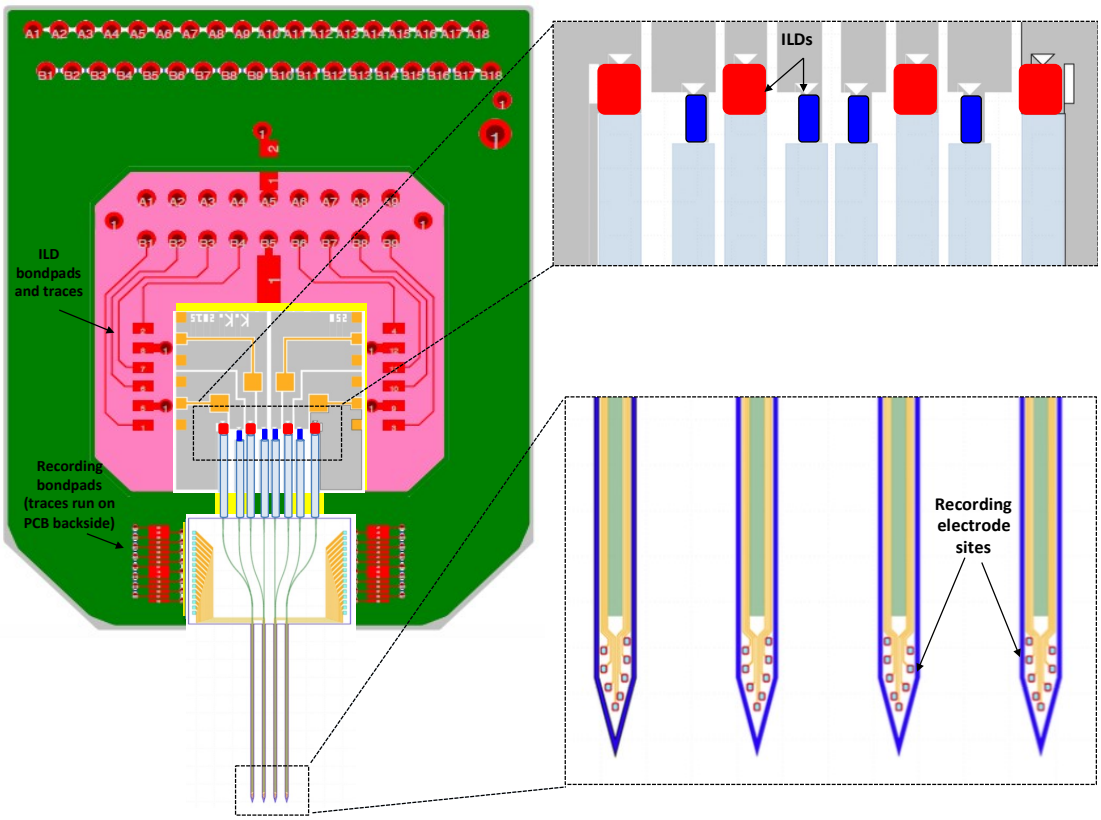

Figure 4-1. Front view of the assembled optoelectrode on a custom-designed PCB showing arrangement details and physical separation between ILDs, recording electrodes, ILD traces and recording traces.

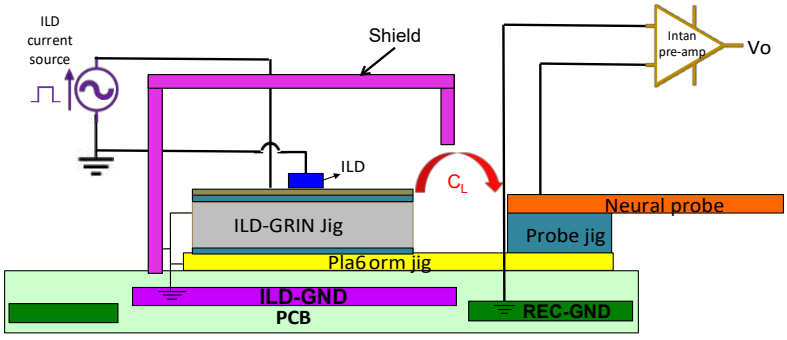

Figure 4-2. A representative block diagram of the optoelectrode assembly shown in **Figure 4-1**, which was used as a reference to construct the lumped circuit model shown in **Figure 4-3.**

output; whereas the effect of coupling inductance was negligible. This also agreed well with our bench testing results, which showed no change in the recorded transient magnitude with increase in ILD driving current. Hence, we focused our effort into studying the RC circuit model for our assembly and understanding the effect of different resistive and capacitive elements on the characteristics of stimulus-locked transients.

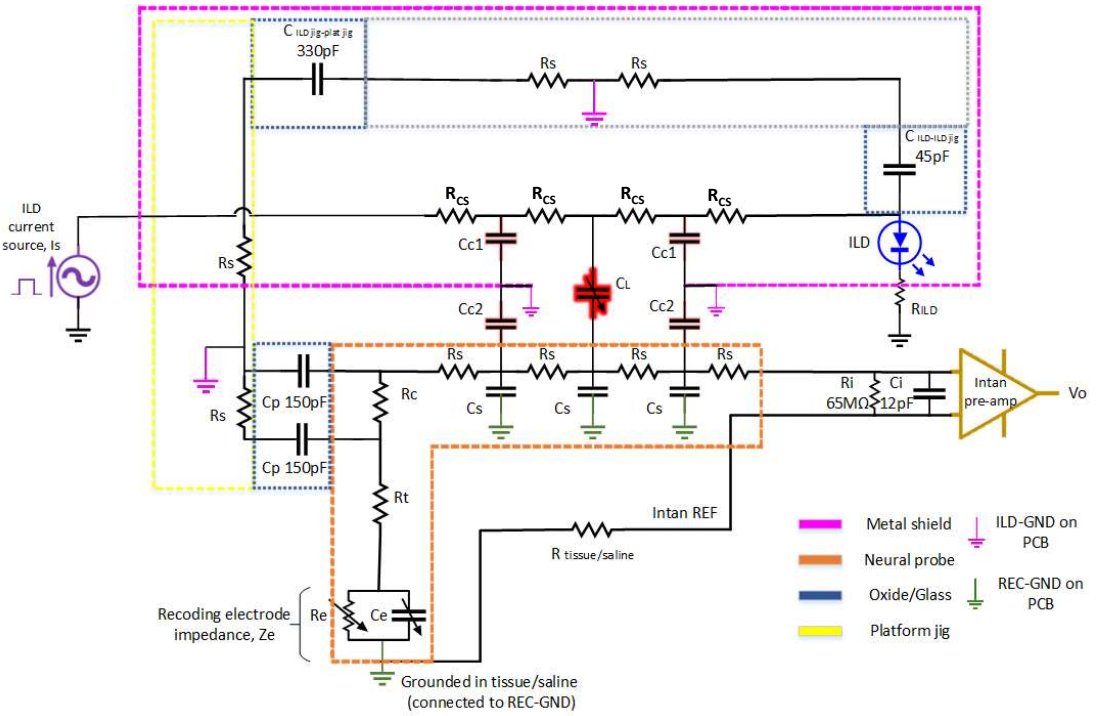

Figure 4-3. Lumped circuit model designed in Cadence SPICE simulator. The circuit blocks are color coded to the assembly components shown in **Figure 4-2**. The circuit was studied to minimize coupling noise from ILDs to the recording electrodes that gets picked up as high frequency transients at Intan output, V_O. C_L is the stray capacitance coupling from ILDs to the neural probe due to the leaky metal shield around ILD-GRIN jig assmebly. Z_e, R_c and R_t are electrode impedance, contact resistance and transmission resistance of interconnects on the neural probe. R_{CS} is the parasitic resistance in the power line connecting the current source and the ILD. R_S and C_S are parasitic resistances and capacitances of silicon. Other capacitances ($C_{ILD\text{-}ILD\ jig}$; $C_{ILD\ jig\text{-}plat\ jig}$ and C_P) approximate parallel plate capacitances between different micro-fabricated silicon components.

Figure 4-3 shows the lumped circuit (RC) model of our assembly design. Different model blocks correspond to their respective color coded assembly

components shown in **Figure 4-2**. The model contains essential coupling paths between ILD-GRIN jig assembly and neural probe that allow easy physical interpretations. It assumes the ILD current path from the source (I_S) to the ILDs as the primary noise source that gets capacitively coupled to the recording channels on the probe. The current source is a pulsed current source, generating typically a rectangular pulse of a few tens of mA. As the current flows into ILD terminals, ILD is switched on and an equivalent voltage (V_{ILD}) gets generated across ILD terminals. This voltage, when coupled to recording traces on the neural probe, generates a high frequency transient spike on Intan recording channel output, V_O. In our design, V_{ILD} can get coupled to the probe via two paths; via air (via C_L) and via the conductive silicon platform jig (via $C_{ILD\text{-}ILD\ jig}$; $C_{ILD\ jig\text{-}plat\ jig}$ and C_P). The magnitude of the capacitive coupling via air (in absence of a shield) was approximated by the equation: $C \approx \varepsilon_0 \varepsilon_r / \ln(d/r)$ F/m [1]. This equation estimates coupling capacitance between circular parallel conductors (ILD and recording traces and their respective wirebonds in this case) of radius r separated by a distance d. ε_o and ε_r are relative permittivities of vacuum and coupling medium (air) respectively. The estimated coupling capacitance (C_L in absence of the shield) is calculated as ~30 fF (for 3 mm total length of parallel wirebonds/traces in our assembly). The actual coupling capacitance could be more than what has been estimated here because of the complex coupling paths from the radiating ILD-GRIN jig to the probe. The crosstalk via platform jig is governed by the size and thickness of all the components that physically connect the ILD lines to probe channels. This was approximated by calculating individual capacitances between ILD and ILD-GRIN jig ($C_{ILD\text{-}ILD\ jig}$); ILD-GRIN jig and

platform jig ($C_{ILD\ jig\text{-}plat\ jig}$); platform jig and neural probe (C_P); using a simple parallel plate capacitance equation: $C = \varepsilon_o \varepsilon_r A / d$. Here, the capacitance between two parallel surfaces depends on their overlapping area, A, and separation d. While a parallel plate capacitor underestimates the capacitance by ignoring fringing fields, later modeling showed these values to have negligible effects. To mitigate the magnitude of crosstalk via the two coupling paths discussed above, we implemented the following shielding and grounding strategies to allow quick discharge of coupling capacitances to the ILD ground plane on the PCB. First, the floating silicon of ILD-GRIN jig and platform jig were physically grounded (shown as ILD-GND in **Figure 4-2, Figure 4-3**). Second, a brass shield was designed around the ILD-GRIN jig assembly and also grounded to ILD-GND plane of PCB. However, considering physical gaps around the shield edges at shield-PCB boundary and the wide opening at the front of the micromachined metal shield in actual device (to provide a window for the GRIN lenses to optically couple to the probe), it was assumed that the shield was not perfect. As a consequence, though most of stray capacitance from ILD-GRIN jig to neural probe (represented as C_{C1} and C_{C2}) was made to discharge to the ground via the shield, it was assumed that a small fraction of escaping electric fields still managed to couple to the neural probe through the shield gap. This leaky capacitance C_L was simulated for a wide range of 1-125 fF, considering that some assemblies can have higher stray capacitance coupling from source to victim than what has been implemented here. All other circuit components including path resistances, coupling capacitances and parasitic components were estimated by calculations and making simplifying assumptions about the geometry of the components and tracks. Components R_S and

C_S in the model are parasitic resistances and capacitances of silicon and the model were simulated for 1-10 Ω of R_S and 1-10 pF of C_S. Ze is the impedance of electrode recording site on the neural probe and was assumed to be 500 kΩ unless Ze was the variable under study (**Figure 4-5**).

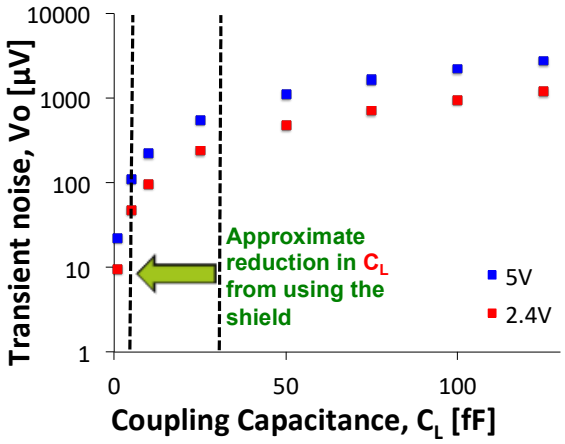

Figure 4-4. The magnitude of stimulus-locked noise transients at V_O as a function of total stray capacitance, C_L (in absence and presence of a metal shield). The reduction in C_L from ~30 fF to ~5 fF with the use of an EMI metal shield proved to be successful in reducing the transients at V_O to less than 100 µV. The plot also shows dependence of noise transient magnitude on ILD stimulating voltage (~5 V for 405 nm and ~2.4 V for 635 nm). Electrode impedance, Ze, is assumed as 0.5 MΩ (Re = 1.12 MΩ, Ce = 284 pF).

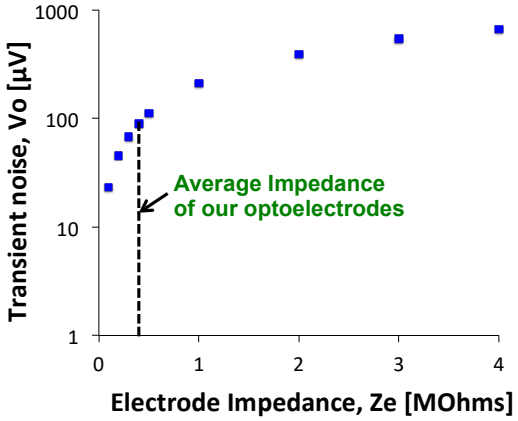

Figure 4-5. The magnitude of stimulation-locked transients induced by 405 nm ILD as a function of electrode impedance, Ze, for second-generation optoelectrodes presented in the current work (in presence of metal shield, assumed C_L = 5 fF) [7]. The results show smaller increase in transient magnitude with increase in Z_e, a desirable design characteristic for chronic studies.

The values of R_C (contact resistance of wire bonding pads of the probe) and Rt (transmission resistance of metal interconnects on the probe) were simulated for the range of 1-100 Ω. Ri and Ci (input resistance and capacitance of Intan differential amplifier) were modeled as 65 MΩ and 12 pF, respectively, based on the product specification sheet [13]. The probe was assumed to be grounded in saline or tissue; which ultimately connects to the recording ground (REC-GND) plane of the PCB.

4.3.2 Simulation results

The model was simulated in Cadence SPICE for both 405 nm (5V/30mA) and 635nm (2.4V/40mA) ILD driving inputs and studied in depth to realize the effect of different circuit elements on the transients generated at V_O. The stimulus-locked transients were found to be most sensitive to coupling capacitance C_L. A change in a few femto Farads at C_L resulted in increase in transient magnitude at V_O by 100s of μV (**Figure 4-4**). Since 405nm ILD has a higher diode turn-on voltage (higher V_{ILD}) than 635nm ILD, 405nm ILDs induced much higher magnitude transients at Vo. Electrode impedance, Z_e, showed a significant effect on transient characteristics. Higher Z_e resulted in transients with higher magnitude and higher transient decay time. The transient decay time was also found to increase with a higher capacitive load at Z_e, whereas transient rise time always followed the pulse rise time of current source, I_S. An increase in R_C also increased the transient magnitude but this effect was not evident until change in R_C was in the range of MΩ which is unlikely in practice. **Figure 4-5** plots model results for transient magnitude vs electrode impedance for second-generation optoelectrodes. The electrical impedance of our fabricated optoelectrodes measures ~0.5 MΩ, hence the recorded artifacts fall within

100 μV range. This plot is helpful to decide the target impedance range for fabricated probes based on the noise requirement of a system. It also provides information regarding expected rise in noise artifacts following increase in electrode impedance post-implantation in chronic animals.

In absence of a metal shield, there is no ground path for C_L to discharge and hence all of C_L (~ 30 fF for ~3 mm of coupling length) gets coupled from ILD to the neural probe, giving rise to larger transients. When not grounded, the floating silicon jigs also discharge to ground via their parasitic capacitances, adding more coupling capacitive noise to the probe. Hence, if the discussed shielding and grounding methods are disabled from the model (all ILD-GND connections disconnected from the model), the transients at V_O not only increase by a factor of ~10 but also become much more susceptible to the changes in geometry, sizes and parasitic electrical properties (resistance, R_S, and capacitance, C_S) of the assembled components and their physical separation. This case was found to be similar to our first-generation optoelectrodes where shielding and grounding was not implemented and the recorded transients during *in vitro* and *in vivo* experiments measured from 1-5 mV [6], [14]. Such a design also showed a higher susceptibility to changing electrode impedance on artifact magnitude**,** which is undesirable for chronic studies where electrode impedance may change over time.

According to our model results, grounding the floating jigs alone (assumed C_L = 30 fF) reduces the transient magnitude by ~1.5 times and shielding the ILD-GRIN assembly alone (assumed C_L = 5 fF) reduces the magnitude by ~2.4 times. When implemented together, both shielding and grounding reduced the transient magnitude

by ~10 times (**Figure 4-6**). These simulations verify how capacitive coupling through each path (via air and via platform jig) produces substantial EMI at V_O. Being based on a lumped circuit approach, the proposed model is easy to apply in practice for understanding, diagnosing and approximating EMI behaviors.

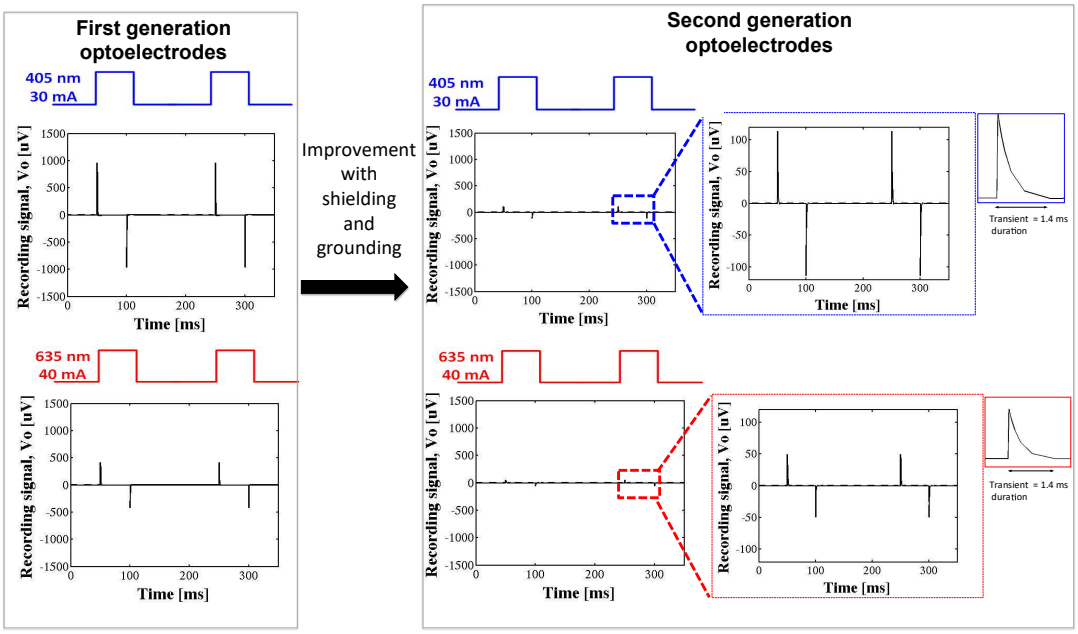

Figure 4-6. Reduction in transient magnitude from first-generation to second-generation of optoelectrodes as predicted by the circuit model. The transients reduce from 1.55 mV (for 405 nm ILD) and 0.65 mV (for 635 nm ILD) in first generation optoelectrodes (assumed CL = 30 fF) to 110 µV (for 405 nm ILD) and 50 µV (for 635 nm ILD) in second generation optoelectrodes (assumed CL = 5 fF). The decay time of the transients remains the same for all cases when simulated for same values of electrode impedance (magnitude = 0.5 MΩ, phase = -65°).

It should be noted that the presented model does not consider the presence of photoelectric effects [5], [15] that could be a potential issue for optoelectrodes and add further to the artifacts in some designs. The silicon substrates for our optoelectrodes are chosen to be heavily boron doped to allow fast recombination of electron-hole pairs and a quicker discharge of photoelectrically-induced transients. Our fabrication process is also modified to define electrode sites buried 2 µm deep in

dielectric films (**Figure 4-7**). This allows us to keep the photoelectric effects to minimum by significantly reducing the intensity of waveguide light that directly hits the electrodes. This absence of photoelectric effect was verified during *in vitro* characterization as discussed in section **4.4.1**.

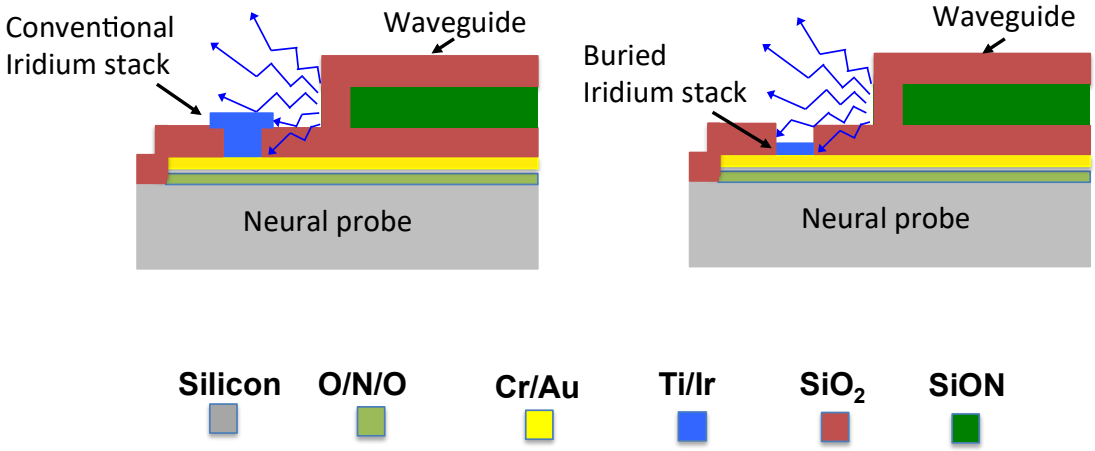

Figure 4-7. Potential way to reduce the photoelectric effect in optoelectrodes. An electrode metal stack buried deep under dielectric layers, reducing the chance of waveguide light directly hitting the metal pads. The silicon substrate used is heavily boron-doped.

4.3.3 PCB design

Considering the high sensitivity of our circuit model to capacitive noise, the PCB was designed to minimize capacitive coupling between the light sources and recording traces. We custom-designed our PCB to have four planes, consisting of a dedicated set of signal plane and ground planes for routing ILD and recording trace connections, respectively. **Figure 4-1** shows details of the designed planes. The middle plane (pink) is the ground plane (ILD-GND) under ILD traces that are routed on PCB front side and the outer plane (green) is the ground plane (REC-GND) under recording traces that are routed on the PCB back side. The recording ground plane was strategically designed and placed around the ILD ground plane such that there

was no overlap between the two sets and hence minimum capacitive coupling.

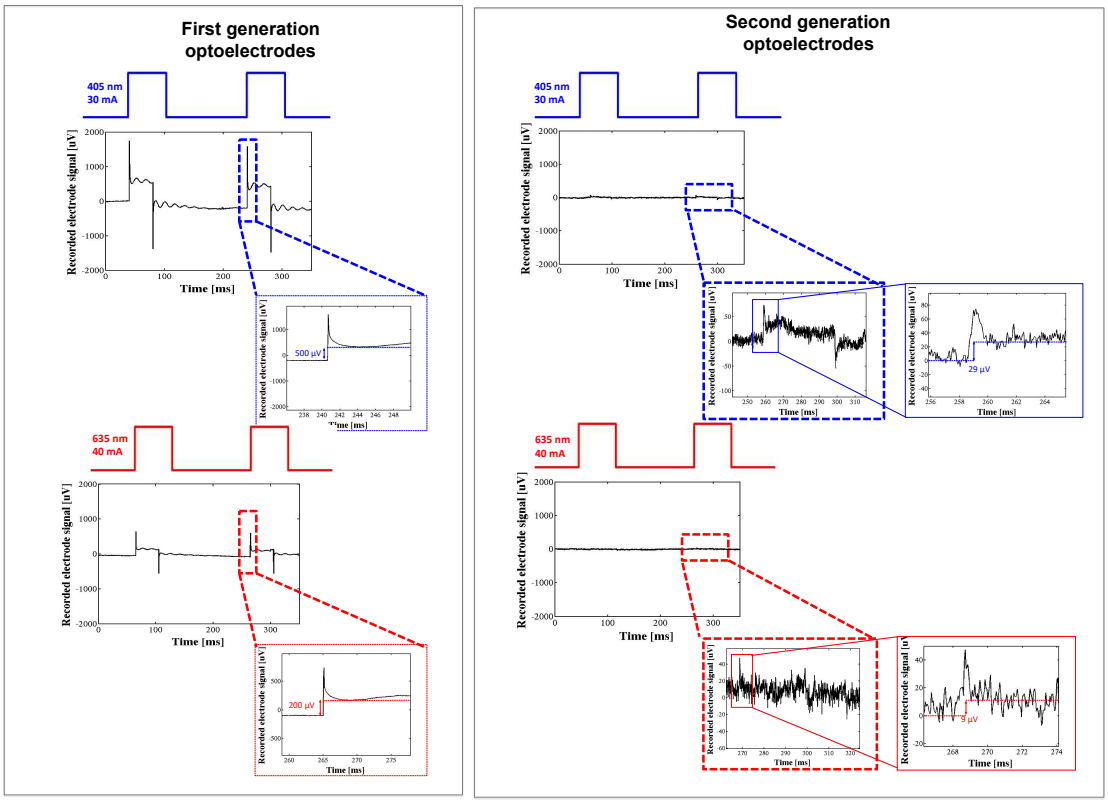

Figure 4-8. Comparison of stimulation-locked artifacts between first-generation and second-generation optoelectrodes measured in phosphate buffered saline (PBS, 0.1 M) with an RHD2164 amplifier board connected to an RHD2000 Evaluation System (Intan technologies, Los Angeles, CA, USA). The transient magnitude and D.C. offset in the artifacts was reduced by a factor of ~15-24. 1.8 mV/ 0.5 mV/ -1.4 mV (onset/DC/offset) for 405 nm ILD (30 mA current) and 0.75 mV/ 0.2 mV/ -0.5 mV (onset/DC/offset) for 635 nm ILD (40 mA current) in first-generation devices was reduced to 75 µV/ 29 µV / 50 µV (onset/DC/offset) for 405 nm ILD (30 mA current) and 48 µV/ 11 µV/ -19 µV (onset/DC/offset) for 635 nm ILD (40 mA current). Due to the presence of the baseline noise and D.C. offset in the recordings, it is difficult to measure exact transient rise and fall times.

4.4 Noise artifact reduction in second-generation ILD-GRIN optoelectrodes

4.4.1 *In vitro* characterization

In vitro impedance and electrical noise measurements were done in phosphate buffered saline (PBS, 0.1 M, Fisher Scientific, Hampton, New Hampshire, USA) with

an RHD2164 amplifier board connected to an RHD2000 Evaluation System (Intan technologies, Los Angeles, CA, USA) and bench laser drivers (4201-DR from Arroyo Instruments, LDC202C from Thorlabs, Inc) connected to ILDs on the devices. With the implementation of EMI reduction techniques discussed above, the magnitude of stimulus-locked artifacts recorded on electrode channels was reduced from few millivolts to ~100 µV. Specifically, for the first-generation devices, 405 nm ILD (50 ms, 30 mA square pulse) stimulation induced transients measuring 1.8/0.5/-1.4 mV (onset/DC/offset) and 635 nm ILD (50 ms, 40 mA square pulse) stimulation induced transients measuring 0.75/0.2/-0.5 mV (onset/DC/offset) (**Figure 4-8).** The artifacts in second-generation devices measured only 75/29/50 µV (onset/DC/offset) for 405

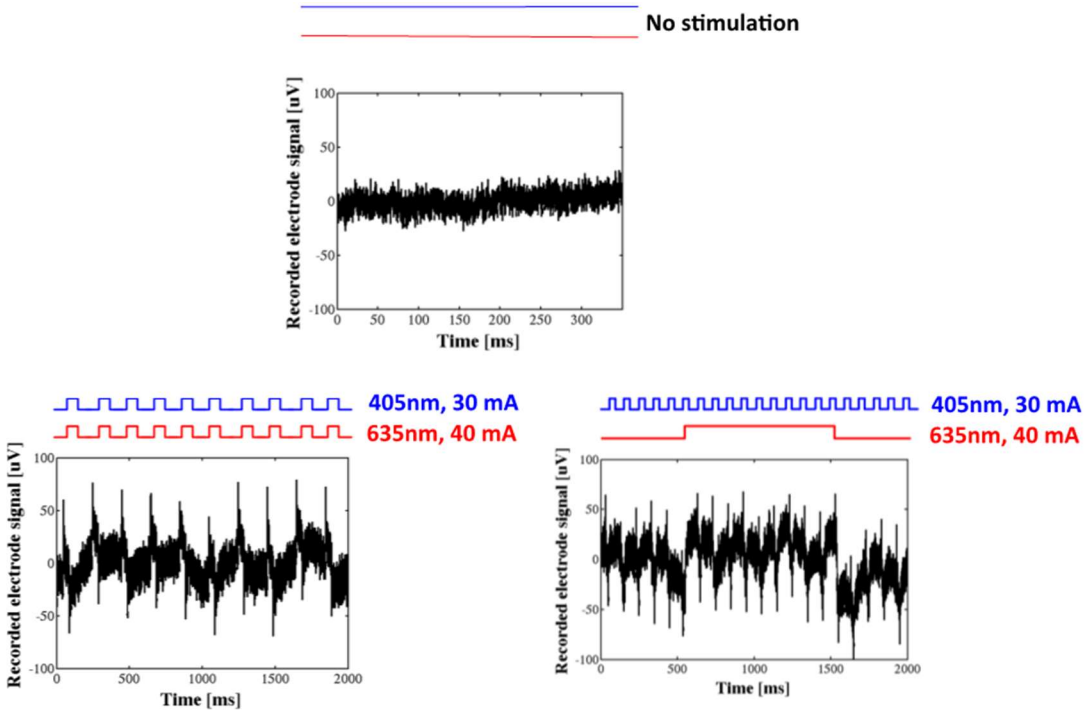

Figure 4-9. Baseline noise and stimulus-locked artifacts measured in phosphate buffered saline when Top, no ILDs are pulsed; middle, both ILDs (405 nm at 30 mA and 635 nm at 40 mA) are pulsed simultaneously at 40 ms pulse width and 20% duty cycle; bottom, 405nm ILD is pulsed at 30 mA (20 ms pulse width, 20% duty cycle) and 635nm ILD is pulsed at 40 mA (1 s pulse width, 50% duty cycle)

nm ILD (30 mA current) and 48/11/-19 μV (onset/DC/offset) for 635 nm ILD (40 mA current), respectively (**Figure 4-8**). We also measured artifacts for different cases of simultaneous dual-color square pulse stimulation, which is a very relevant scenario in multi-opsin optogenetic experiments. The artifact magnitude and other characteristics were maintained below 100 μV in all such experimental cases (**Figure 4-9**). These artifacts comprised of a fast-transient component with an asymptotic attenuation, features which are consistent with capacitive effects as predicted by our model. However, the experimental artifacts also had an additional DC offset component. This offset was present when damaged ILDs (with same V-I characteristics but no light output) were driven too, verifying the absence of any photoelectric-induced artifacts. One of the possible reasons for the DC offset could be the potential difference between system ground and Intan reference signal. This could arise from the parasitic (resistive or capacitive) components of saline or tissue. The origin of this offset needs further investigation for future designs.

The total artifact reduction (for transient and DC artifacts) measured for *in vitro* experiments was ~15-24 times. This is more than what was estimated from simulation results (10 times reduction). This could be possibly because the total artifact reduction reported for *in vitro* results is for both the DC and the transient artifacts. Whereas, our model only simulated transient artifacts and not DC artifacts.

4.4.2 *In vivo* characterization

Packaged four-shank second-generation optoelectrodes with 4 dual-color waveguide ports and 32 recording sites were used to record neural activity in awake mice. We recorded 120/-95 μV (onset/offset) artifacts for 200 μW violet-light 40 mA

square pulse stimulation (50 ms) (**Figure 4-10**), <50 µV artifacts for 450 µW red light illumination 50 mA square pulse stimulation (300 ms), and transient-free recording for 200 µW violet-light 40 mA half-sine stimulation (**Figure 4-10).** The electrical design modification discussed in this work was a useful modification since *in vivo* electrical artifacts were considerably reduced in these probes compared to the first-generation optoelectrodes [14] though both were capable of robustly driving neural activity (**Figure 4-11**).

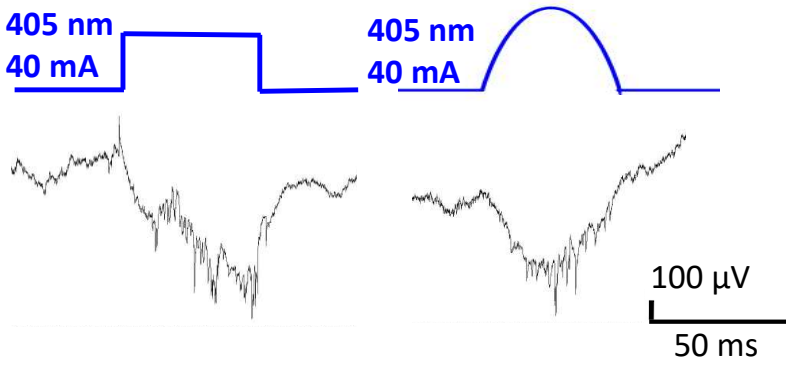

Figure 4-10. Wide-band (0.3-7,500 Hz) spiking activity and stimulus-locked artifacts recorded from CA1 pyramidal cell layer of an awake head-fixed mouse expressing ChR2 in pyramidal cells. A 40 mA 405 nm square pulse induces 120 µV/ -95 µV (onset//offset) artifacts for 40 mA square pulse stimulation (405 nm diode) and artifact-free recording for 40 mA half-sine stimulation.

4.5 Artifact reduction using ILD-biasing

To further reduce EMI-induced artifacts in the system, we applied an ILD biasing technique, where a modulating alternating signal is superimposed on a fixed direct current bias to drive the ILDs. We current-biased the ILDs at very low currents (<3mA), which corresponds to high voltages (~70-80% of lasing voltage) for lasers (**Figure 4-12**), reducing the transient magnitude by 8-16%. Biasing reduces the differential of source coupling voltage, V_{ILD}, thereby reducing the capacitive noise between stimulating and recording traces. This was verified via both modeling and

bench testing (**Figure 4-13a**).

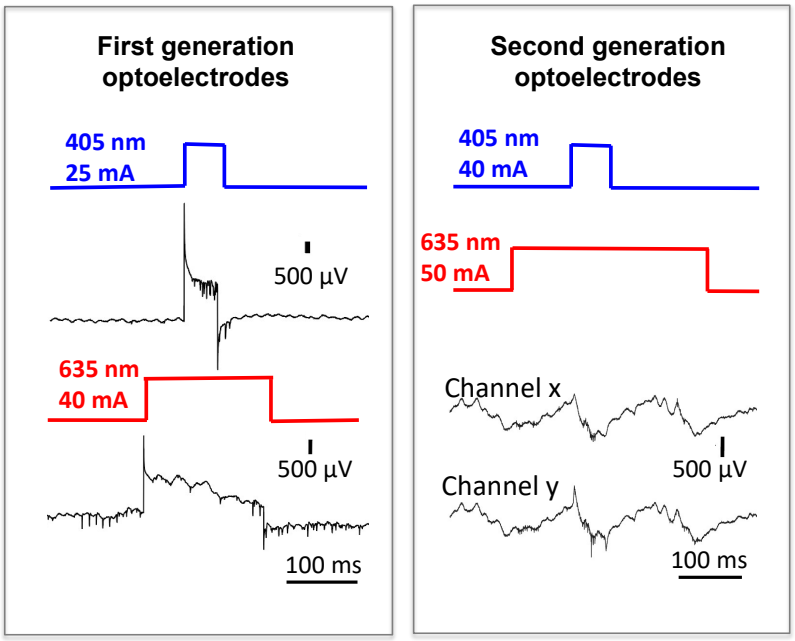

Figure 4-11. Comparison between stimulus-locked artifacts in first generation and second generation of optoelectrodes. The left panel shows the wideband spiking activity (0.3-10,000 Hz) recorded using first-generation devices [14]; which measured 5 mV/ 2 mV/ -1.8 mV (onset/DC/offset) for 25 mA current (405 nm diode) and 3 mV/ 1.5 mV/-0.7 mV (onset/DC/offset) for 40 mA current. With implementation of improved electrical design in current second-generation devices, the recorded artifacts during light stimulation (as shown in the right panel) were significantly reduced to 30- 450 µV range for both colors across all channels. The artifacts on channel x and channel y are representative of the smallest and largest artifacts recorded on different channels of the same device.

Though laser biasing helps to reduce transient magnitude on recording channels, two potential challenges need to be addressed before implementing biasing for optogenetic applications. First, it should be ensured that there is no light emission from waveguide tip at biasing and no resulting light activation of neurons. For this reason, it is critical to bias ILDs way below their threshold currents. For our device, the ILD light power at 2.5 mA was measured to be less than 5 µW. At such low currents/optical power, ILDs behave as LEDs. GRIN lenses can only collimate a focused beam of light that enters the GRIN input facet within the designed NA of the

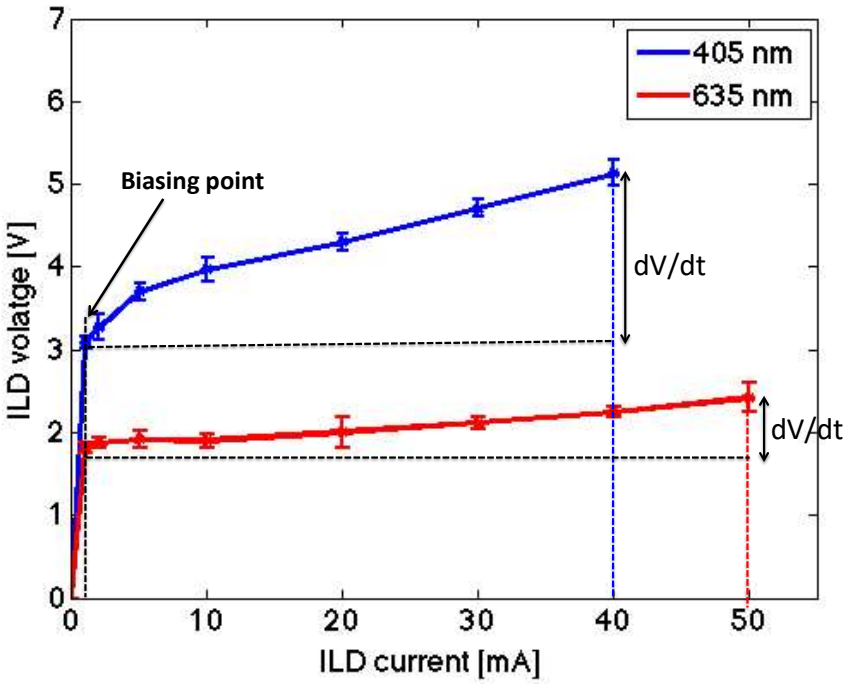

Figure 4-12. (a) ILD voltage-current (V-I) characteristics for epi-side down flip-chipped 405nm and 635nm ILDs (N=5; data points show the mean of the collected data and error bars represent standard deviation). When ILDs are biased at low currents (shown as ILD biasing point), the voltage differential (dV/dt) applied across ILD terminals decreases significantly.

lens. For the lenses used in our design, the half acceptance angle for incoming rays was 24 degrees, which is ideal for coupling a laser beam. Light output from LED is lambertian and hence cannot be coupled effectively from ILDs to GRINs and then to the waveguides. This was also verified experimentally for our devices (**Figure 4-13b**), where no optical power was detected at the waveguide output for currents < 4 mA for both ILDs, confirming no possibility of neuron stimulation in biased condition. However, this might not be the case when coupling light sources (ILDs or LEDs) directly to fibers/waveguides without an intermediate lensing mechanism [16]–[18]. In such cases, some light might get coupled and emitted from the waveguide port, stimulating nearby neurons. Therefore, though biasing technique can

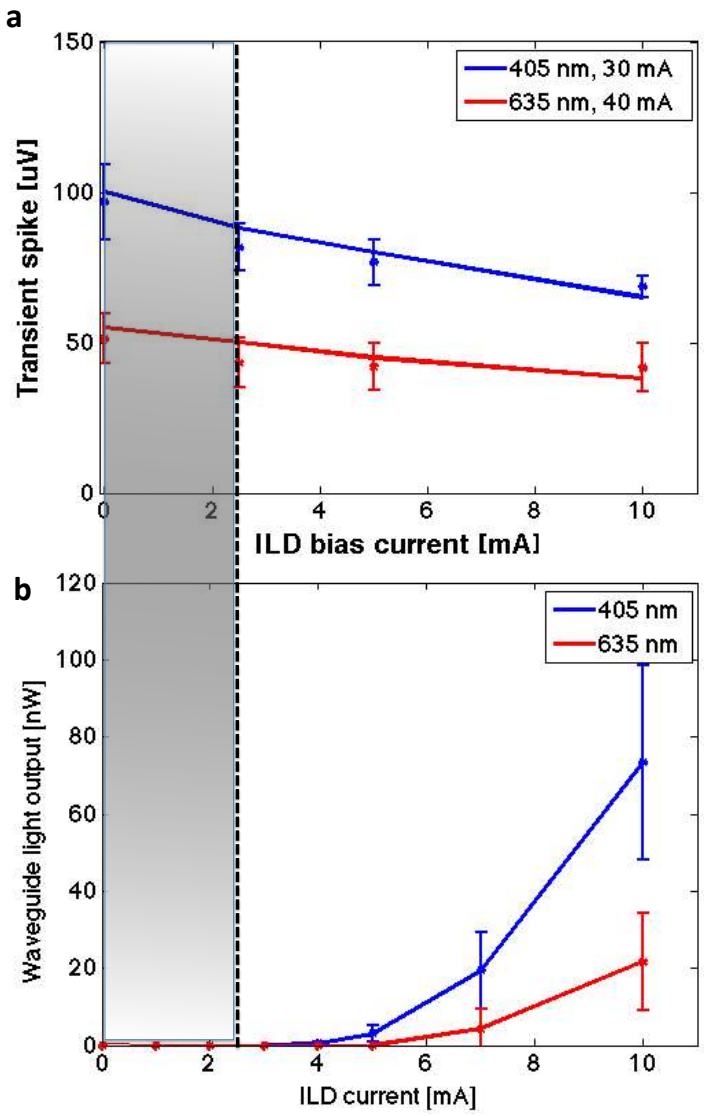

Figure 4-13. (a) Simulated and *in vitro* measurements for stimulus-locked transient noise as a function of ILD biasing current. As the biasing current is increased, the voltage differential across the ILD drops, resulting in decrease in capacitive coupling and transient noise (N=10 channels from the same device, data points show the mean of the collected data and error bars represent standard deviation). (b) Waveguide optical power versus ILD driving current for the assembled devices. No light output was detected at waveguide port for upto 3 mA of ILD current, confirming no possibility of neural stimulation at biasing, if implemented for ILD-GRIN optoelectrodes. (N=2 devices with 8 waveguides each; data points show the mean of the collected data and error bars represent standard deviation).

be an attractive solution to reduce stimulus-locked artifacts in ILD-GRIN optoelectrodes (**Figure 4-13),** utility of this technique may differ for other

optoelectrode designs. A potential concern of biasing optoelectrodes is accelerated tissue heating. When biasing at a constant current (power), the devices continuously heat up, reducing the permissible device operation time for safe operation *in vivo*. Biasing at low currents can help mitigate this problem as the power dissipated at low current biasing (2.5 mA x 1.8 V for 635 nm) is much lower than power dissipated in ILD lasing mode.

The ILD biasing technique for artifact reduction was also verified *in vivo* where the artifacts induced by 405 nm ILD (at 40 mA) were reduced from 120/-95 μV (onset/offset) at zero current bias to 97/-88 μV (onset/offset) when biased at 2.5 mA current. Though the artifact reduction at 2.5 mA is not huge, biasing could still be an effective way to get further reduction in artifacts for applications, where artifacts need to be kept at their bare minimum to detect smaller than usual spikes.

4.6 Choosing the right ILD driver

One of the challenges for optoelectrodes with on-board light sources is to find a reliable driver interface for driving the on-board light sources. While there are many commercial multi-channel LED drivers available, the same is not true for ILD drivers because of the many reasons. ILDs are highly sensitive current-driven sources and cannot be driven by voltage sources, which are simpler to design. ILDs require a constant current source, which is linear, noiseless and delivers an exact amount of programmed current to the laser diode. A good current resolution and control feature prevents sudden power surges on driver channels preserving efficiency and lifetime of the laser. ILDs also generate thermal noise and need a low noise driving circuit. A driver with stable low noise on its channels (<5 μAp-p @ 1-10 Hz) will also couple

less noise to the nearby circuit components in a microsystem.

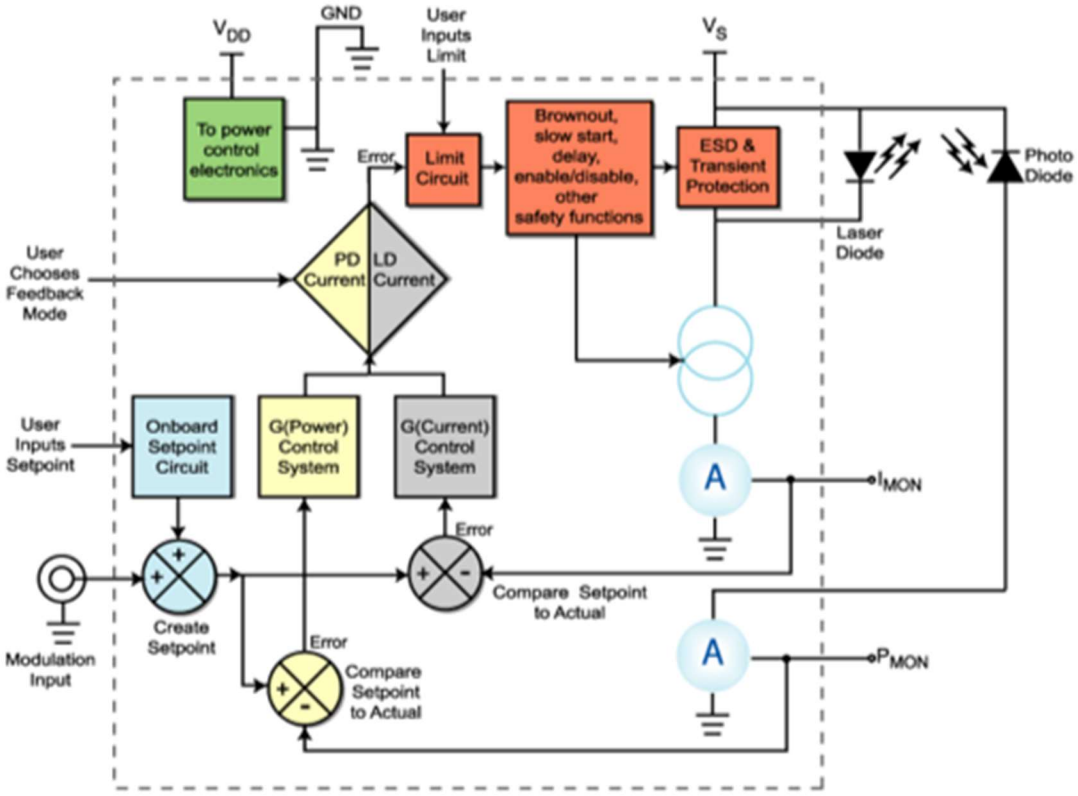

Figure 4-14. Block diagram of essential components of a laser diode driver. [Source: *https://www.teamwavelength.com/info/laserdiodedrivers.php*]

The laser driving circuitry has to integrate not only precise current control but also many protection circuits for reliable laser operation. All these factors make a multichannel laser driver design costly, bulky and challenging to fit into a small form factor, leading to its less popularity in commercial markets. Instead, single-channel bench-top laser drivers (LDC202C from Thorlabs, Inc; 4201-DR from Arroyo Instruments) are fairly common in use in both academia and industry. Some single channel on-board laser drivers are currently available too (FL593FL from Wavelength Technology, ATL100mA212D from Analog technologies, iC-HT from iC Haus). However, they offer limited functions, laser safety circuitry and noise

performance as compared to the bench-top drivers.

The block diagram in **Figure 4-14** shows important design elements that should be incorporated in a basic laser diode driver design. A current/power feedback control is an essential component of a laser driver that maintains a constant driving current assuring safe laser operation. The driver usually has current/power monitoring voltage ports (I_{MON} and P_{MON}). The current and power are related to this voltage by a transfer function specific to the driver. Limit circuit, softstart and ESD protection are part of safety features for the laser. Limit circuit lets the user to set the limit current based on the operating parameters of the laser diode and shuts off the laser diode current if the control system drive exceeds this current limit setting. Softstart function allows the laser current to rise slowly (usually within 100s of milliseconds) from zero to its final value when a laser is turned on, hence preventing the laser from sudden thermal breakdown during initial switch on period. The feature is more essential for continuous wave lasers that operate on high currents (in amperes) and are more susceptible to thermal damage from sudden rise in temperature. ESD protection should be present at all laser ports to prevent them from sudden electrostatic discharge when connecting or disconnecting the laser from the circuit. There are additional considerations when pulsing a laser [19], [20]. Laser switching induces additional noise in the system, which could be detrimental for optogenetic studies. When using high pulse rise time (~10ns), impedance line effects become a concern. To prevent this, the impedance of the diode cables needs to be properly matched. Otherwise, the power reflections in the cable can induce pulse ringing. This ringing can couple to the recording lines corrupting neural data and also damaging the laser.

All bench top lasers usually come with the impedance-matched cables and hence form a better choice for low-noise applications. The packaging of a laser also plays an important role in cancelling noise during diode pulsing. Any parasitic capacitance between the cathode of the diode and earth ground can cause slow rise times and stray signal pickup. The driver circuit for lasers should also include a well-filtered power supply that, as efficiently as possible, blocks capacitive and inductive loads and other sources of interference. Battery operation circumvents the problem but is not an option in many industrial applications. Keeping the connections between the diode laser and the driver circuit short generally will help reduce interference.

Laser diode drivers can vary widely in feature set and performance and should be chosen according to the user-end application and laser specifications. For driving the ILD-GRIN optoelectrodes described in this work, the laser diode driver should fulfill the requirements listed in **Appendix C**.

4.7 Conclusion

EMI coupling paths in a compact optoelectrode design could exist in a subtle manner, making it hard to identify. A lumped circuit modeling approach was useful for our understanding the sensitivity of the physical and non-contact coupling paths that exist. We used this to identify and successfully mitigate the putative source of stimulus-locked artifacts associated with first-generation ILD-GRIN waveguide probes [7]. The grounded silicon jigs along the metal shield formed effective 6-face faraday enclosure for the electrical assembly, suppressing most of the emitting electric fields generated within the ILD-GRIN jig assembly. The grounded jigs made of highly conductive silicon wafers (0.005 Ω-cm resistivity) provide a physical path

for the transients arising from the stimulation sources to quickly discharge to the ground and the brass shield helps to terminate and ground the electric fields that couple via air. At very low frequencies (near-field), where electric and magnetic field shielding is considered separately; shielding is not just a matter of reflection and absorption but of locally redirecting the fields. Our model predicted strong presence of electric (capacitive) than magnetic (inductive) fields. In our current work, we used a brass shield that can provide electric field shielding only. Brass is highly conductive, easily machinable and resistant to corrosion, making it a desirable metal to integrate into micro packaging. And as evident from experimental results, brass was effective in shielding significant electric coupling from ILD traces to recording traces via air. Other than providing shielding, the shield also helped to block the light escaping from the optical coupling junctions and facilitates convective cooling during device operation via 200 μm diameter air holes drilled on its top surface. For low frequencies, since the air hole size is much smaller than the working wavelengths, they provide almost no impedance to the flow of currents on the conducting cap surface and hence do not affect the shielding quality. For future designs, if a magnetic field shield has to be incorporated, high permeability materials (such as steel) can be used to redirect the fields. To implement a magnetic shield, the shield thickness should be designed to be more than the penetration depth given by formula: $\delta = \sqrt{[\rho/(\pi f \mu)]}$, where, ρ is resistivity of the material, f is the frequency of EM wave and μ is absolute magnetic permeability of the metal. Advanced EMI analysis tools (such as High Frequency Structural Simulator) can also be studied for more extensive noise analysis in future designs. Furthermore, a low-noise custom multi-channel ILD

driver can also be designed and integrated for ILD driving in high-density optoelectrode systems.

References

[1] Charles S. Walker, *Capacitance, Inductance, and Crosstalk Analysis*. Artech House, 1990.

[2] H. Bassen, "Electromagnetic Interference of Medical Devices and Implications for Patient Safety," *Int. J. Bioelectromagn.*, vol. 4, no. 2, pp. 169–172, 2002.

[3] A. V Kravitz, B. S. Freeze, P. R. L. Parker, K. Kay, M. T. Thwin, K. Deisseroth, and A. C. Kreitzer, "Regulation of parkinsonian motor behaviours by optogenetic control of basal ganglia circuitry," *Nature*, vol. 466, no. 7306, pp. 622–6, Jul. 2010.

[4] X. Han, X. Qian, J. G. Bernstein, H.-H. Zhou, G. T. Franzesi, P. Stern, R. T. Bronson, A. M. Graybiel, R. Desimone, and E. S. Boyden, "Millisecond-timescale optical control of neural dynamics in the nonhuman primate brain.," *Neuron*, vol. 62, no. 2, pp. 191–8, Apr. 2009.

[5] S. Royer, B. V. Zemelman, M. Barbic, A. Losonczy, G. Buzsáki, and J. C. Magee, "Multi-array silicon probes with integrated optical fibers: Light-assisted perturbation and recording of local neural circuits in the behaving animal," *Eur. J. Neurosci.*, vol. 31, no. 12, pp. 2279–2291, Jun. 2010.

[6] K. Kampasi, J. Seymour, E. Stark, G. Buzsáki, K. D. Wise, and E. Yoon, "Efficient assembly of multi-color fiberless optoelectrodes with on-board light sources for neural stimulation and recording," *Conf. IEEE Eng. Med. Biol. Soc.*, pp. 4479–4482, 2016.

[7] K. Kampasi, D. F. English, J. Seymour, S. McKenzie, E. Stark, K. D. Wise, G. Buzsaki, and E. Yoon, "Independent optogenetic control of distinct neural populations using low-noise fiberless optoelectrodes," (unpublished).

[8] K. Najafi, J. Ji, and K. D. Wise, "Scaling limitations of silicon multichannel recording probes," *IEEE Trans. Biomed. Eng.*, vol. 37, no. 1, pp. 1–11, 1990.

[9] E. Laboure, C. Gautier, F. Costa, and W. Melhem, "Accurate simulation of conducted interferences in isolated DC to DC converters regarding to EMI standards," *Pesc 1996*, pp. 1973–1978, 1996.

[10] M. H. Pong, C. M. Lee, and X. Wu, "EMI due to electric field coupling on PCB," in *PESC Record - IEEE Annual Power Electronics Specialists Conference*, 1998, vol. 2, pp. 1125–1130.

[11] M. T. Zhang, F. C. Lee, J. Roudet, and E. Clavel, "Conducted EMI analysis of a boost PFC circuit," in *Proceedings of APEC 97 - Applied Power Electronics Conference*, 1997, vol. 1, pp. 223–229.

[12] D. F. Knurek, "Reducing EMI in switch mode power supplies," *10th Int.*

Telecommun. Energy Conf., pp. 411–420, 1988.

[13] Intan Technologies, “RHD2000 Series Digital Electrophysiology Interface Chips,” 2012. .

[14] K. Kampasi, E. Stark, J. Seymour, K. Na, H. G. Winful, G. Buzsáki, K. D. Wise, and E. Yoon, “Fiberless multicolor neural optoelectrode for in vivo circuit analysis,” *Sci Rep, Nat. Publ. Gr.*, vol. 6, p. 30961, 2016.

[15] A. Khurram and J. P. Seymour, “Investigation of the photoelectrochemical effect in optoelectrodes and potential uses for implantable electrode characterization,” in *Proceedings of the Annual International Conference of the IEEE Engineering in Medicine and Biology Society, EMBS*, 2013, vol. 2013, pp. 3032–3035.

[16] E. Stark, T. Koos, and G. Buzsáki, “Diode probes for spatiotemporal optical control of multiple neurons in freely moving animals.,” *J. Neurophysiol.*, vol. 108, no. 1, pp. 349–63, Jul. 2012.

[17] M. Schwaerzle, K. Seidl, U. T. Schwarz, O. Paul, and P. Ruther, “Ultracompact optrode with integrated laser diode chips and SU-8 waveguides for optogenetic applications,” in *Proceedings of the IEEE International Conference on Micro Electro Mechanical Systems (MEMS)*, 2013, pp. 1029–1032.

[18] M. Schwaerzle, P. Ringwald, O. Paul, and P. Ruther, “First dual-color optrode with bare laser diode chips diecrtly butt-coupeld to hybrid-polymer waveguides,” in *MEMS*, 2017, vol. 2, pp. 26–29.

[19] U. M. Malzahn, “Driving Diode Lasers Is Straightforward,” *EuroPhotonics*, pp. 22–23, 2004.

[20] D. Hodgson, K. Noonan, B. Olsen, and T. Orosz, “Pulsing a Laser Diode,” 2004 [Online]. Available: http://assets.newport.com/webDocuments-EN/images/Pulsing_Laser_Diode_IX.PDF.

Chapter 5

Multishank Low-Noise Fiberless Optoelectrodes for Independent Control of Distinct Neural Populations

5.1 Introduction

In Chapter 3, we presented successful implementation of the first fully-integrated multicolor optoelectrode to activate and silence different neuron types *in vivo*. The idea to enable independent activation and silencing of the same or different groups of neurons with such precision and scalability has generated a lot of enthusiasm in the neuroscience community. This formed our motivation to scale-up the first-generation prototype from a single-shank to a four-shank optoelectrode which could be used for neuroscience studies in behaving animals. However, significant technological challenges had to be addressed to implement the proposed high-density prototype.

While higher-density optoelectrodes with on-board light sources [1]–[6] form an attractive choice for optogenetic tools, they are challenging to implement for implantable devices because of the following potential issues. First, the densely-packed light sources can induce device heating and risk thermal damage to the surrounding tissue during device operation. Second, close proximity of electrical traces on a compact scale makes them susceptible to EMI coupling giving rise to stimulation-locked artifacts as described in Chapter 4. Third, packing light sources of

different wavelengths (for independent control of different neuron types) in a high-density micro-assembly poses design and assembly challenges of its own. The only available multi-color optoelectrode approaches for independent control of different neuron types at that time [1], [5] were either limited to only one color illumination at a single site with intra-cortical illumination area of ~3000 μm^2 [1] or to a single multi-color site with recorded stimulus-locked artifacts [5]. Another multicolor optoelectrode has been reported recently but lacks *in vitro* and *in vivo* device verification and validation [6].

In this chapter, we present high-density four-shank optoelectrodes offering high-quality recording capability with <100 μV stimulation artifacts for multicolor local circuit analysis [7]. Our devices have integrated 405 nm and 635 nm ILD light sources to enable crosstalk-free two-color activation of neural spiking and synaptic transmission in independent neural populations. The resulting optoelectrode was used to independently activate two spatially-intermingled cell types: pyramidal cells expressing Channelrhodopsin-2 and parvalbumin cells expressing red-shifted channel rhodopsin, ChrimsonR in the hippocampal CA1 region of awake mice [7]. In the following sections of this chapter, we present device design, assembly and results and discuss the technological challenges that are involved with scaling up a fiberless optical stimulation system.

5.2 Design and methods

As in our previous developments [5], [8] the design involves coupling compact ILDs to monolithic dielectric optical mixer waveguides via GRIN lenses. In contrast to the previous single-shank version, the present device has four shanks: each shank is

70 µm wide, 22 µm thick, and inter-shank pitch is 300 µm. The integrated iridium electrode sites have a 20 µm pitch, allowing high-density recordings from densely populated brain regions. The integrated customized "ILD-GRIN jig" houses eight ILD-GRIN pairs (four 405 nm ILDs and four 635 nm ILDs with a GRIN lens coupled to each ILD) in a highly compact design. GRIN lenses again serve as a key design element enhancing optical coupling and minimizing thermal dissipation and electromagnetic coupling in the implanted probe. **Figure 5-1** shows the schematic of GRIN-based optoelectrodes.

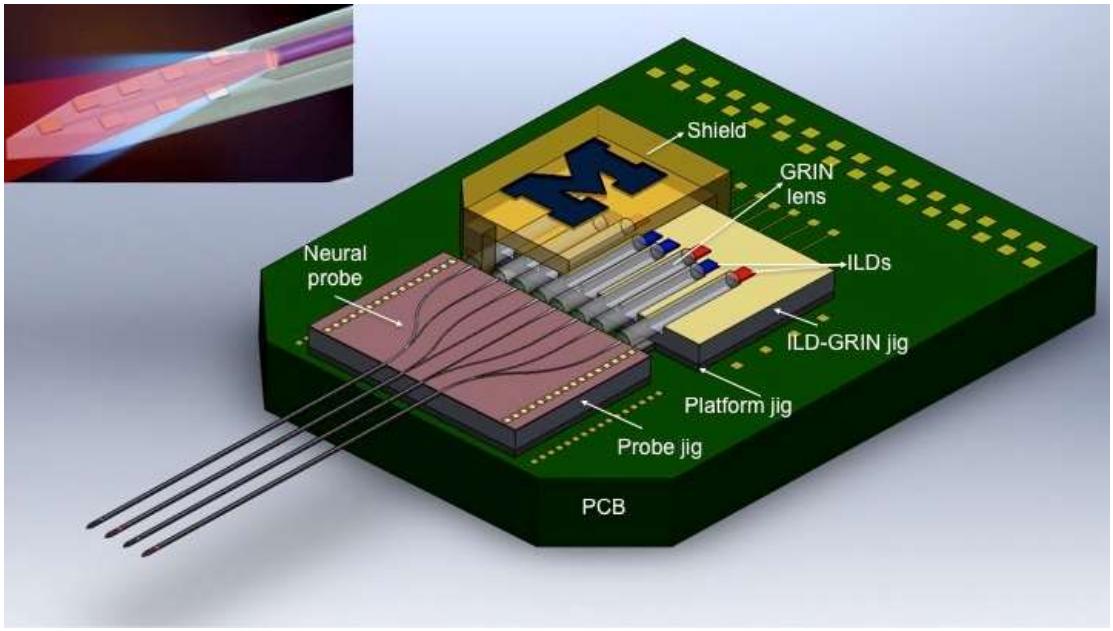

Figure 5-1. Schematic of multishank multicolor fiberless optoelectrode assembled on a printed circuit board

5.2.1 Optical design

As in our previous work [5], [8], a collimation-focusing mechanism using GRIN lenses was implemented for the optical design of an optoelectrode. GRIN design parameters including N.A., working distances (L1 and L2) and mechanical length (Z), were optimized to achieve the desired magnification (M<1) for enhanced

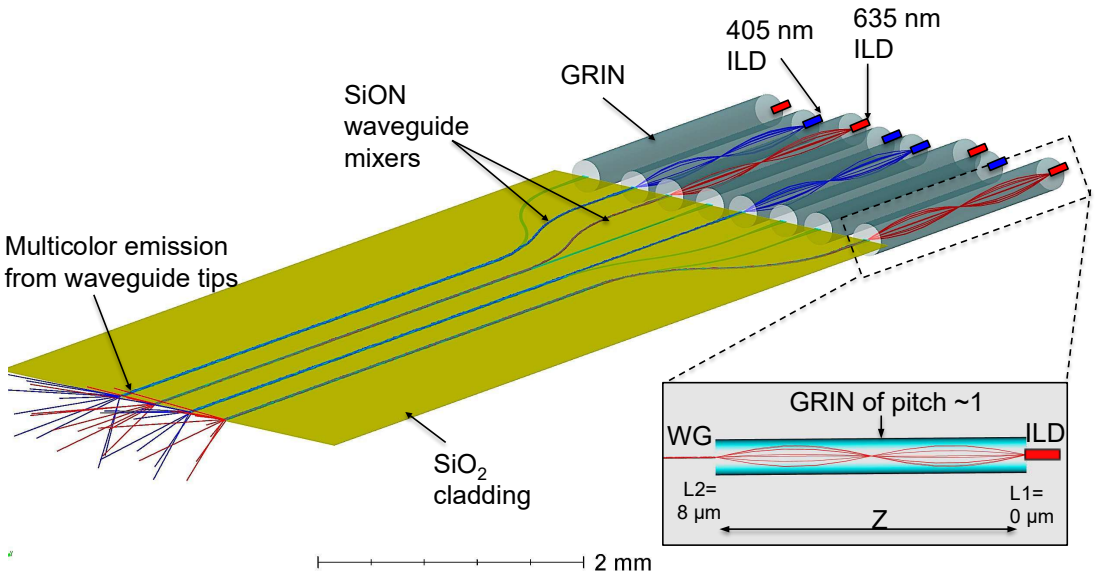

Figure 5-2. Zemax optical model of optical mixer waveguide coupled to ILDs to deliver multicolor light output at all waveguide ports. The model consists of eight ILDs (four 405 nm four 635 nm ILDs) coupled to arms of optical mixer via their respective GRIN lenses. The 405 nm (2.38 mm long) and 635 nm (2.54 mm) GRIN lenses are designed to facilitate optimal coupling while allowing maximum misalignment tolerance between the ILDs and the waveguide. The schematic in the inset shows a full pitch GRIN lens collimating and focusing a divergent ILD laser beam into the waveguide mixer arm (WG).

optical coupling. GRIN lens numerical aperture, N.A., (0.4226), was designed to closely match the waveguide N.A. (0.4228) [5]. The optical design of the four-shank mixer waveguide was studied using ray-tracing models and is shown in **Figure 5-2**. A full-pitch (P~1) GRIN lens was used to couple ILD and achieve beam focusing on the waveguide mixer arm backend (7 µm x 50 µm cross-section) (**Figure 5-2**, *inset*). The focused beam enters the waveguide mixer arms, which taper down from a width of 50 µm and converge into a 5 mm-long straight waveguide (cross-section: 30 µm x 7 µm). Since the GRIN lens has a continuous change of the refractive index (RI) within the lens material, light rays can be continuously bent within the lens until they are finally focused on a spot. The focused beam travels through the curved and tapered

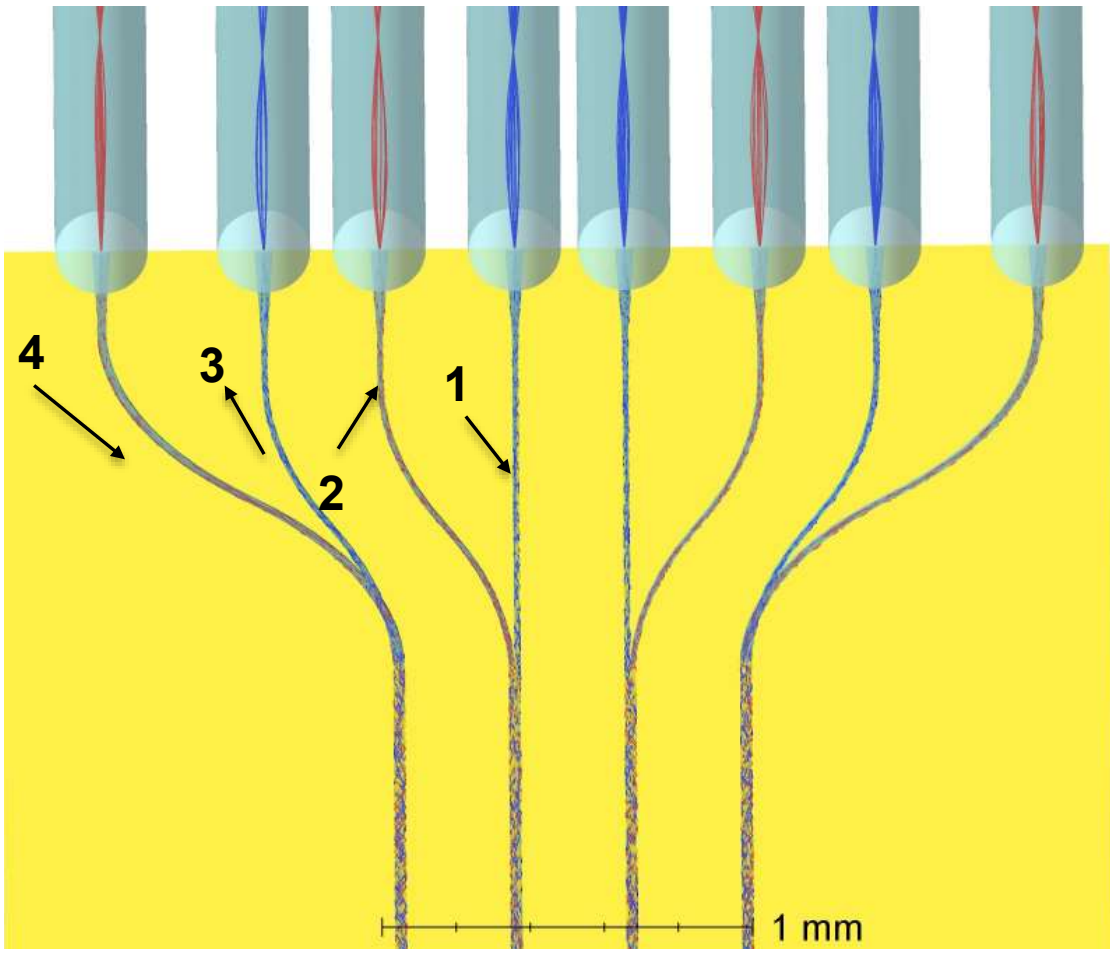

Figure 5-3. Waveguide mixer arm geometries designed in Zemax to achieve optical output within ~3% of the mean value for both transmitting wavelengths (405 nm and 635 nm) at all waveguide ports. Mixer arm 1 is a straight waveguide. Mixer arms 2 and 3 are identical with 2.335 mm bending radius, but arm 2 transmits 635nm wavelength and arm 3 transmits 405nm wavelength, resulting in difference in optical intensities delivered at the output of each arm. Mixer arm 4 has the maximum bend of 1.370 mm radius. Since 405nm wavelength suffers more dispersive loss than 635nm, a mixer arm with the minimum loss (arm 1) was designed to transmit 405nm and a mixer arm with the maximum loss (arm 4) was designed to transmit 635nm.

waveguide mixer arms, and is finally emitted from the output port of the channel waveguide on the probe shank (7 μm x 30 μm cross-section).

The coupling losses at ILD-GRIN junction and GRIN-waveguide junction were modeled, yielding a total coupling loss of 0.925 dB from ILD to waveguide at both junctions. For multi-shank probes, the mixer arms had to be bent to route two colors

on all four shanks. The beam suffers radiation (mode conversion) losses in the bends.

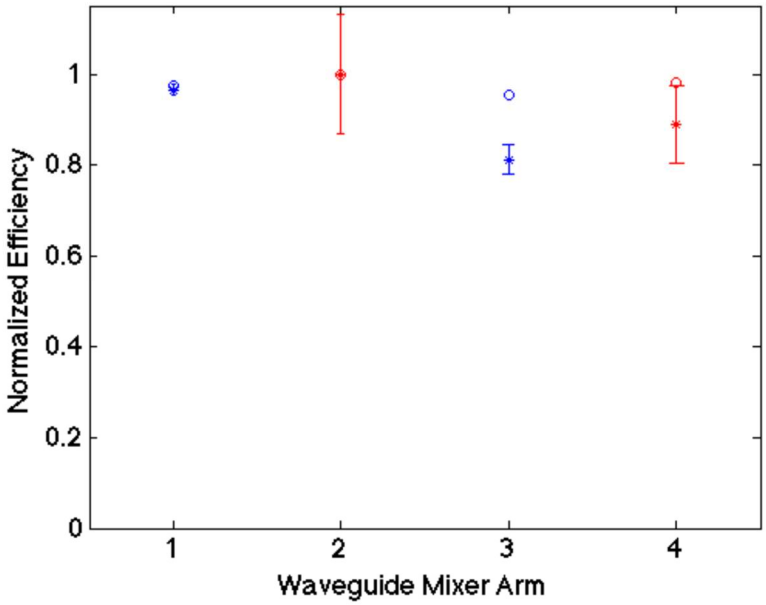

Figure 5-4. Zemax simulated data and experimental data for normalized optical power emitted at the tip of each waveguide when transmitting at their respective wavelengths. The mixer arms 1 and 3 transmit 405 nm wavelength and are marked in blue; mixer arms 2 and 4 transmit 635 nm wavelength and are marked in red. Though mixer arms 2 and 3 have same geometric design, optical transmission of 635 nm wavelength via arm 2 is more than of 405 nm wavelength via arm 1 because 405 nm gets more scattered than 635 nm wavelength. The experimental optical output of all four shanks was within 11.4% of the mean value for both transmitting wavelengths. The measurement data was collected on optical micromanipulators (for N=3 devices x 8 waveguides each).

These losses were reduced by maximizing the bend radius of mixer arms, which is limited by the diameter and assembly pitch of GRIN lenses. For maintaining the smallest possible form factor and maximizing the radius of curvature of each mixer arm, we designed mixer arms 2 and 3 with a bending radius of 2.335 mm and mixer arm 4 with a bend radius of 1.370 mm [9], [10]. The designed width for all mixer arms was 15 µm, except the width of arm 4 was increased from 15 µm to 24 µm to compensate for the higher radiation loss in the sharper bend (**Figure 5-3**). Other than coupling and radiation loss, light rays also suffer from propagation loss, which is

attenuation in the form of scattering and absorption as they travel through the waveguide. Since 405 nm suffers more scattering losses than 635 nm, ILDs were arranged in such a manner that 405nm ILD is coupled with the mixer arm design with least loss (arm 1) and 635 nm is coupled with the mixer arm design with highest loss (arm 4), while both colors are available on each shank. The optical power output at each waveguide port at the shank is given by ILD output optical power minus total optical loss through each waveguide, L_T, which is expressed as: $L_T(dB) = L_{coupling}(dB) + L_{propogation}(dB) + L_{radiation}(dB)$, where $L_{coupling}$ is coupling loss, $L_{propagation}$ is propagation loss and $L_{radiation}$ is radiation loss. As noted above, the discussed design modifications were successful in achieving the optical output of all four shanks within 11.4% of the mean value for both transmitting wavelengths (**Figure 5-4**). Multi-shank design involves the alignment of eight ILD-GRIN-waveguide pairs in all three axes making it more susceptible to alignment losses during micro-assembly. Thus, it is critical to keep designed losses to minimum.

Since the waveguide aperture on neural shank was positioned 55 μm away [1], [5], [11] and the recording sites span 140 μm, opsin activation thresholds must be crossed at a distance of ~200 μm from the tip of 7 μm x 30 μm waveguide. The light cone angle exiting the waveguide (NA = 0.4228) is calculated to be 18.11 degrees ($NA = n_o * \sin\theta$, n_o for tissue = 1.36). Considering geometric losses and tissue scattering losses through brain tissue for each wavelength, the required light intensity (~2 mW/mm^2 for 405 nm [12], [13] and ~7 mW/mm^2 for 635 nm [14]) is achieved at a distance of 200 μm from the waveguide if the output power (intensity) at the waveguide tip exceeds 100 μW (476 mW/mm^2) for 405nm and 200 μW (952

mW/mm^2) for 635 nm. These values are well within the simulated values from our model [5].

5.2.2 Thermal design

As the number of diodes per device increases, the electrical power consumed increases, and hence the dissipated heat. Following the same bio-heat transfer design

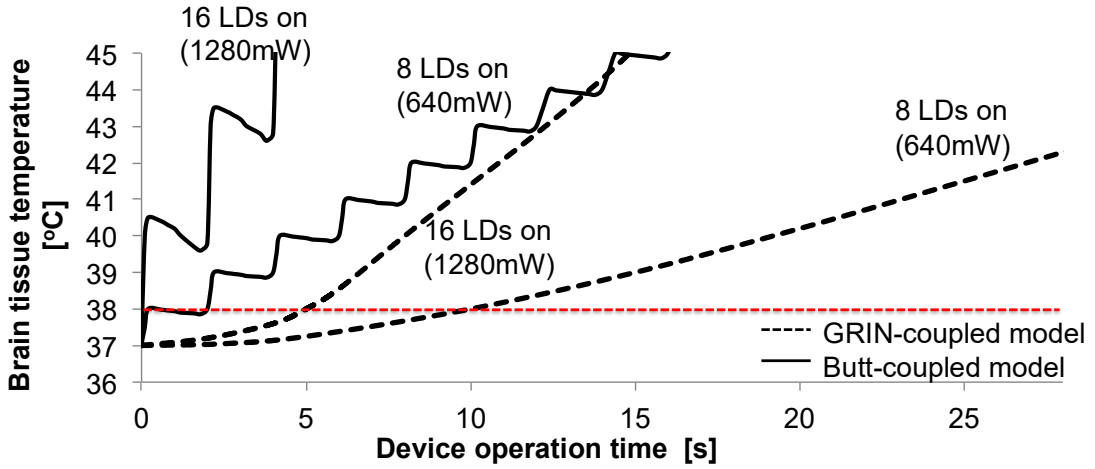

Figure 5-5. Tissue temperature rise over time for multi-shank GRIN-coupled optoelectrodes compared to their design equivalent butt-coupled optoelectrodes with 8 and 16 assembled diodes. The power values on each graph line signify the total input electrical power delivered to the device, 80mW per diode. Butt-coupled optoelectrodes show a fast and oscillatory temperature rise at their probe shanks in response to the pulsed ILD driving currents. In contrast, GRIN-coupled optoelectrodes exhibit slow and gradual temperature rise because of thermal isolation between ILDs and probe shank, offered by the thermally insulating GRIN lenses.

using COMSOL Multiphysics (COMSOL Inc.) that was discussed in Chapter 3, we simulated the temperature rise at the tissue surface for GRIN-coupled and butt-coupled designs for 8- and 16-diode assemblies, respectively (**Figure 5-5**). These results indicate that 8 ILDs (one on each shank) can be pulsed for 10 s continuously just above their threshold current (200 ms pulse width, 10% duty cycle), which fits the requirement for optogenetic circuit-analysis applications [1]. The higher thermal resistance of the GRIN lenses helps manage the heat generated by the light sources

without the use of active (e.g., thermoelectric) coolers. GRIN-coupled design was found to prolong the device operation by a factor of four as compared to conventional butt coupled design, allowing scaling in terms of the numbers of shanks and diodes.

5.2.3 Electrical design

The electrophysiological data from Chapter 3 indicated presence of stimulation-locked artifacts. These artifacts obscure neural activity near the stimulation site for tens or hundreds of milliseconds and pose a limitation in neuroscience studies. In second-generation four-shank optoelectrodes, we successfully mitigated the EMI coupling from the ILD traces to recording traces, bringing down the magnitude of stimulation-locked artifacts within permissible levels of <100 μV. The modified electrical design of four-shank optoelectrodes is discussed in Chapter 4 [5], [15]. The simulation results in Cadence circuit simulator showed ~10 times reduction in noise transient magnitude between first- and second-generation optoelectrodes.

5.2.4 Device fabrication and assembly

The fabrication process (**Figure 5-6**) follows Michigan probe microfabrication technology [5], [11], [16] with monolithic integration of a waveguide mixer (and fabrication of a custom heat sink (ILD-GRIN jig) for micro-optic assembly of ILDs and GRINs as described in detail in Chapter 3 [5]. **Figure 5-7a** shows the SEM image of the released neural probe with the inset showing the magnified SEM view of a single shank tip. **Figure 5-7b** shows a probe backend with waveguide mixers. The SEM image of bonded ILDs on ILD-GRIN jig, ILD alignment marks and GRIN slots is shown in **Figure 5-8a**. **Figure 5-8b** shows the image of the released ILD-GRIN jig with eight assembled ILDs.

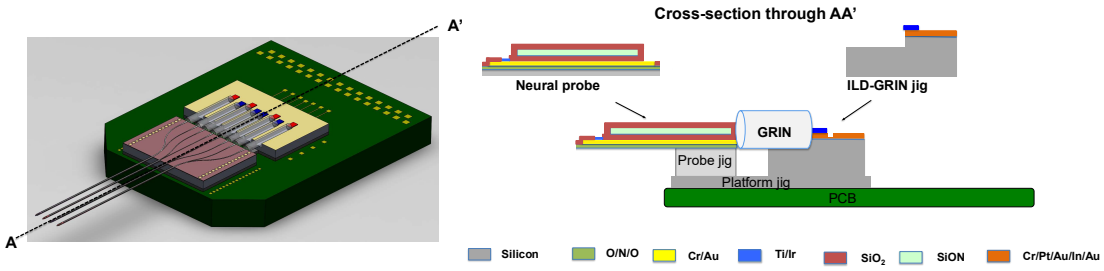

Figure 5-6. Device fabrication details along A-A' showing final assembly of fabricated components on PCB. The fabrication process steps are same as described in Figure 3-6.

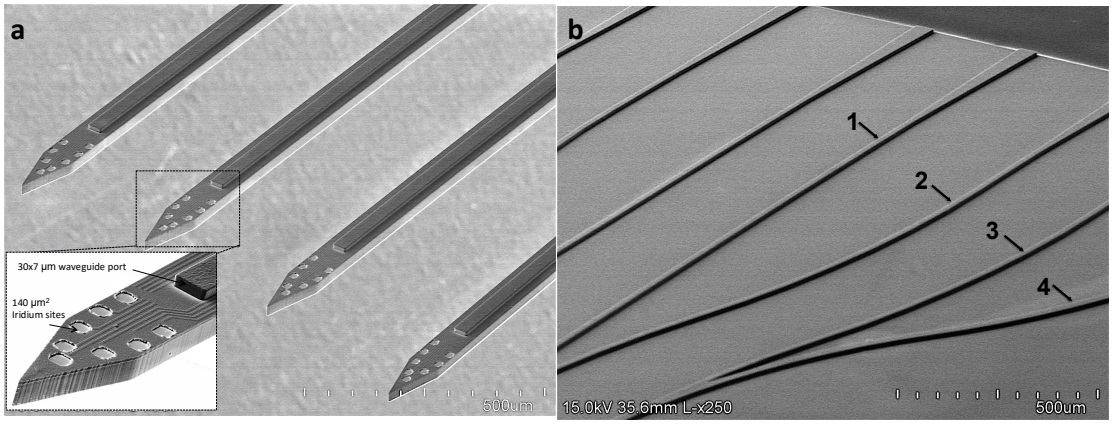

Figure 5-7. (a) Fabricated neural probe shank tips with monolithically-integrated dielectric waveguides. The inset shows a high magnification SEM image of a single shank with a dielectric waveguide tip (7-µm core with 2-µm top and 2-µm bottom cladding) and iridium electrodes in Buzsaki8 configuration. (b) Fabricated dielectric waveguide mixer arms on the neural probe backend. All waveguide mixer arms (design 1, 2, 3 and 4) taper from 50-µm width at the backend to 30-µm width at shank tip.

The packaging process, especially for laser diodes, should preferably be a low-temperature and pressure-free process as excessive bonding heat and stress may cause change in the parametric performance of the laser diode. A stringent alignment tolerance is required in order to achieve good optical coupling. Though, one of the biggest micro-packaging challenges for ILDs is to manage their thermal dissipation, especially for applications that require driving lasers at wider-pulse widths (milliseconds are used to drive most opsins). Thermal damage to laser can affect its

optical brightness, wall-plug efficiency, spectral quality and reliability over time. Epi-side down bonding technique prevents this damage by bringing the heat source to the

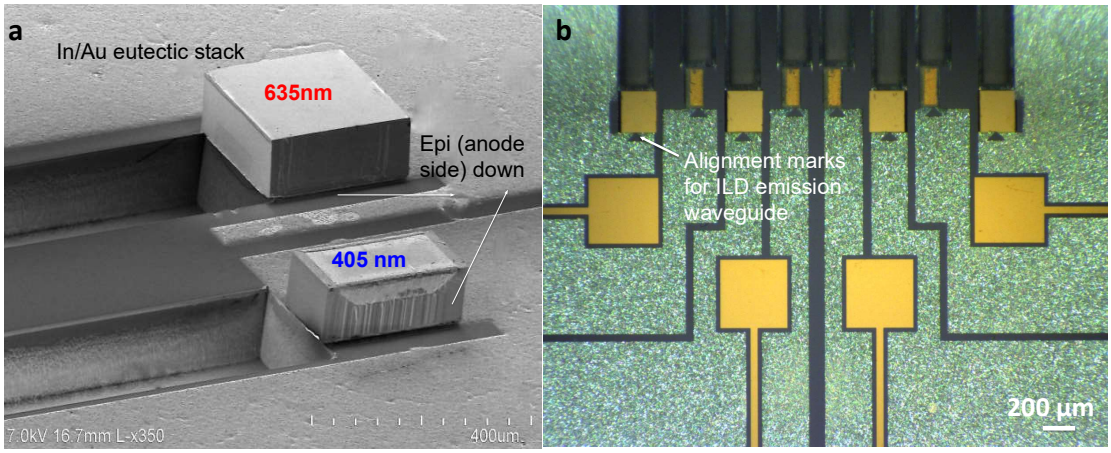

Figure 5-8. (a) High magnification SEM image of epi-side down flip-chipped 405 nm and 635 nm ILDs on the ILD-GRIN jig (heat sink made of silicon with 6 µm eutectic In/Au metal stack). (b) Fabricated ILD-GRIN jig (5 mm x 5 mm) with defined ILD alignment marks and eight bonded ILDs.

heat sink as close as possible and minimizing the thermal resistance [17], [18]. The use of eutectic metals with good thermal conductivity and formation of void-free thermal contact between the laser diode and the heat sink further minimizes thermal resistance. A solder bump technique [17] can accomplish chip positioning through self-alignment; however, thermal dissipation is compromised since heat can only be transferred through the solder bumps. Bridged die bonding [19] employs solder pattern with a gap; it facilitates better heat conduction than solder bump technique and prevents the solder from blocking the sensitive laser ridge but still provides a higher thermal resistance for the heat flux generated at the active region that has to be re-directed to the side of the laser diode before travelling towards the heat sink. Understanding these design considerations and maximizing heat management for our design, we designed the metal pads on our heat sink to have a full contact with the

ILD anode face.

In current implementation, In-Au eutectic bonding at 200°C was implemented to achieve epi-down bonding of the ILDs on ILD-GRIN jigs. Sub-micron diode alignment and initial bonding was achieved with the aid of a flipchipper tool (Lambda Flipchip bonder, Finetech, Germany) that precisely aligned the ILDs to ILD ridge-alignment marks defined in the metal lift-off step. The vacuum pick-and-release process using the flipchipper was used to cause minimum handling damage to ILDs. The ILD-GRIN jigs with assembled ILDs were then annealed in a rapid thermal annealing oven in 5% forming gas for final eutectic bond formation. An oxygen-free annealing process prevents indium from oxidation resulting in stronger indium-gold eutectic bond (void-less solder bond) and improved V-I characteristics. The ILDs were positioned such that the front of their emitting ridge hangs over the GRIN trench by 10 um, preventing the solder to block the front ridge. The implemented bonding technique used was a flux-less, pressure-free bonding to ensure that the ridge does not sink in the solder. The diode bonding metal pads were designed to cover the maximum area of the ILD-GRIN jig for facilitating maximum conduction and uniform heat distribution on a 5 mm x 5 mm heat sink. The shorter heat paths from ILDs' active region to ILD-GRIN jig and finally to the ground plane of the PCB was also modeled to verify safe and reliable operation for optoegentics experiments [5].

The optoelectrode was constructed by assembling all microfabricated components on a custom designed PCB (**Figure 5-6**). It is critical to control misalignment of optical components in all dimensions within its respective tolerance ranges [5]. This was achieved by photo-lithographically defined geometries during

microfabrication, and precise assembly techniques with the aid of flip-chip bonder and micromanipulators. Following optical assembly, a micromachined light-weight brass shield (**Figure 5-1**) was put in place over the ILD-GRIN jig assembly and grounded to a PCB ground. The platform jig and ILD GRIN jig were also electrically connected to the PCB ground using wirebonds and conductive silver epoxy. The assembled devices were wire-bonded on the PCB. Two Omnetics connectors: a 36-pin male for 32 neural recording channels and reference and ground, and a 12-pin male for driving and grounding 8 ILDs (A79022-001 and A79624-001; Omnetics Connector Corporation, Minneapolis, MN, USA) were soldered to the PCB via flexible wires (36744MHW, Phoneix wires Inc, South Hero, VT, USA) for electrical interfacing with an external driver and amplifier. Our assembly approach is also modular as the assembled ILD-GRIN packages on the PCB can also be reused from device to device to facilitate a cost and labor effective solution. The neural probes are assembled on the PCBs using an acetone dissolving epoxy and PDMS, which can be readily removed/peeled off to replace and re-align a new waveguide neural probe on the same assembly. This probe replacement can be done if the probe accidently breaks during implantation or if an explanted chronic device has to be reused for more experiments. The reusability of the technique was verified experimentally by assembling more than one probe on the same PCB assembly (with all assembled components) and achieving optical power values at all shanks within ~12% accuracy. **Figure 5-9** shows the assembled four-shank device prototype and **Figure 5-10** shows the microscopic view of shank probe tips with multicolor light emission.

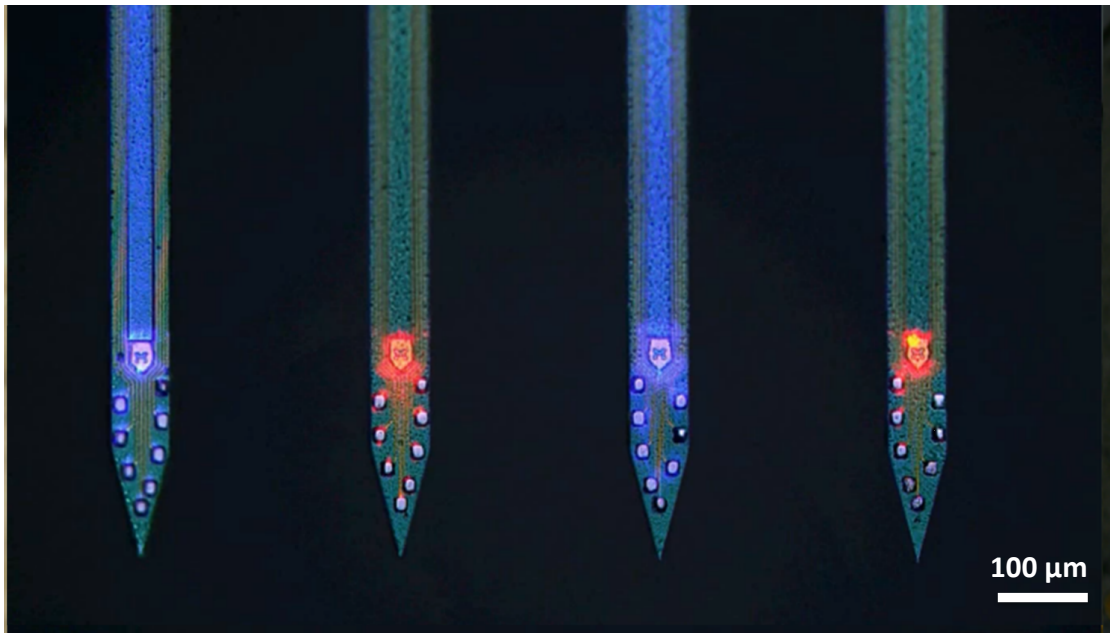

Figure 5-9. Working device prototype showing enlarged view of the probe shank tips with multi-color light illuminating from the 30 µm x 7 µm waveguide tips.

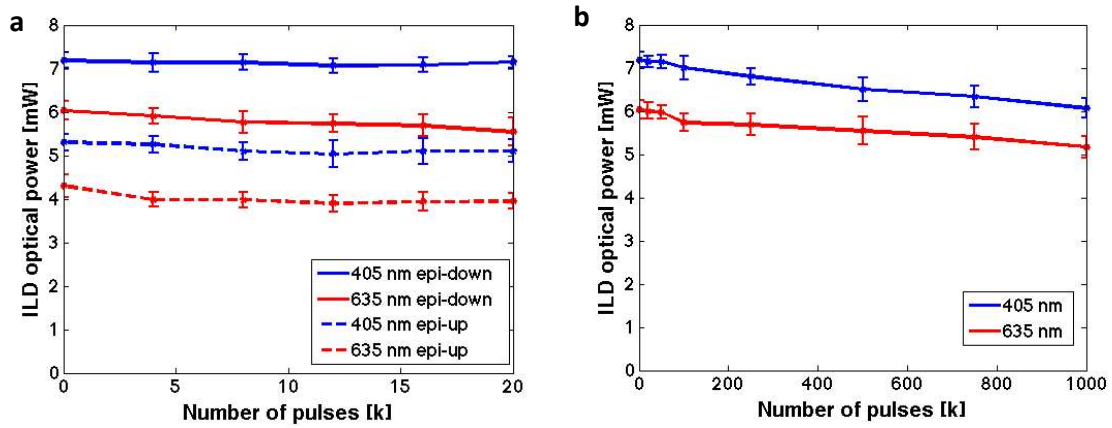

Figure 5-10. ILD characterization. (a) Comparison of optical power output and its decay for epi-side down and epi-side up flip-chipped ILDs (N=5 for each ILD type, data points show the mean of the collected data and error bars represent standard deviation) when pulsed for 20,000 pulses at 5 Hz frequency, 20% duty cycle. Initial optical power of epi-side down bonded ILDs was measured to be 35.47% (for 405 nm at 30 mA) and 40.23 % (for 635 nm at 40 mA) more than that of epi-side up bonded ILDs. The optical power decay after 20,000 pulses was observed to be similar for epi-up and epi-down ILDs. (b) Lifetime testing of epi-down ILDs (N=5 for each ILD type, data points show the mean of the collected data and error bars represent standard deviation) when pulsed for 1 million cycles at 5 Hz frequency, 20% duty cycle. The reduction in ILD output power after driving them through one million pulses was measured to be 18.94% for 405nm ILDs and 16.12% for 635nm ILDs when operated at 30mA and 40mA, respectively.

5.3 *In vitro* device characterization

5.3.1 ILD lifetime tests

Fluxless, no-pressure indium-gold eutectic bonding at 200 OC was implemented for ILD bonding to ILD-GRIN jigs. This bonding recipe was selected to protect the ILDs from potential damage at high bonding temperatures and pressures. Indium is a soft solder that forms a eutectic bond with gold at ~180 ^{O}C and offers high thermal conductivity (80 W/m/^{O}C) and low electrical resistivity (8.8 μΩ.cm). Its capability to deform plastically also helps to relieve the stress developed in bonded structures, making it ideal for packaging of sensitive laser chips. The ILDs were flip-chip bonded with the anode facing down (epi-side down configuration). A bench-top laser diode driver (4201-DR, Arroyo Instruments) was used for all characterization tests. The effectiveness of epi-side down bonded ILD technique was verified experimentally by comparing the ILD performance characteristics for epi-side up and epi-side down bonding techniques (**Figure 5-10a**). The initial optical power measured for epi-side down bonded diodes was 35.47% (405 nm) and 40.23 % (635 nm) higher than the epi-side up bonded diodes and this difference in optical power was maintained through 20,000-pulsed cycles (N=5). The optical output characteristics of a laser are sensitive to the operating temperature of the laser diode and excessive heat accumulation in the active region can influence spectral and spatial characteristics of a laser. Epi-side down bonding technique helps in reducing the thermal resistance of the ILD package by bringing the heat source to the heat sink as close as possible [20]. The close proximity of the active region of the ILD to the heat sink allows rapid dissipation of the generated heat flux to the ILD-GRIN jig and then to the PCB,

enhancing the optical power of the ILD. Given the better performance characteristics of the epi-side down packaging technique, it was used for all the following device assemblies and characterization [20], [21].

It is important to access the lifetime of the ILDs when integrating them into implantable devices for chronic use. There can be various reasons for diode degradation over time including thermal damage due to absorption of laser light, recombination enhanced defect motion or facet degradation due to non-radiative recombination. We verified the longevity of our packaged ILDs by driving them at maximum diode currents for a million pulse cycles (20% duty cycle, 40 ms pulse width). The initial (at zero pulse cycles) wall-plug efficiency (or radiant flux) for epi-side down packaged 405 nm ILDs and 635 nm ILDs on ILD-GRIN jig (heat sink) was measured as 5.1% (for 405 nm at 30 mA, N=5) and 6.8% (for 635 nm at 40 mA, N=5), respectively. The increase in wall-plug efficiencies as compared to what was reported before [5] is attributed to the improved ILD packaging technique using a die (flipchip) bonder. A more uniform contact of ILDs to the substrate helps in better heat dissipation, yielding higher optical power for a given driving current. The decrease in ILD light power after running through one million pulses was only 18.94% (for 405nm, N=5) and 16.12% (for 635 nm, N=5), suggesting good ILD longevity for chronic experiments (**Figure 5-10b**).

5.3.2 System optical loss measurements

We quantified optical losses in each part of the system separately: (1) coupling loss at the ILD-GRIN and GRIN-waveguide junctions; (2) radiation loss in the bends and corners of the optical mixer; and (3) propagation losses through the waveguide.

Measurement using the direct cut-back method was used to evaluate propagation loss per unit length of a straight waveguide [5]. The observed slope of the linear fit 0.48 dB/mm for 635 nm and 0.59 dB/mm for 405 nm, gives the waveguide propagation loss. The y intercept (at 0 mm length) of the linear fit, 1.76 dB for 635 nm and 1.92 dB for 405 nm, gives the total coupling (including Fresnel) loss between the GRIN lens and waveguide, including back reflection at the tip of the waveguide. The coupling loss from ILD to GRIN output was separately estimated as 0.5±0.1 dB for 635 nm and 0.6±0.05 for 405 nm (mean ± s.d., N=5) by comparing optical power at ILD and ILD-GRIN outputs. Radiation losses from straight channel waveguides are generally negligible for well-confined modes but may increase in waveguide bends. Our mixer geometry has two bends per light path, and we measured radiation losses of 0.93±0.47 dB for mixer arm 2 and 1.1±0.31 dB for mixer arm 4 (mean ± s.d., N=5) when coupled to 635 nm ILD source. Similarly, we measured radiation loss of 0.95±0.12 dB for mixer arm 3 (mean ± s.d., N=5) when coupled to 405 nm ILD source. The summed losses for all mixer arms during bench testing were 7.28±0.05 dB for arm 1 (405 nm source, 7.68 mm waveguide length), 6.9±0.57 dB for arm 2 (635 nm source, 7.728 mm waveguide length), 8±0.17 dB for arm 3 (405 nm source, 7.728 mm waveguide length) and 7.41±0.41 dB for arm 4 (635 nm source, 7.887 mm waveguide length) (mean ± s.d., N=5). The total optical loss measured for packaged devices (**Figure 5-11**, **Figure 5-9**) was 13±0.7 dB and 10.88±1.24 dB (mean ± s.d., N=24 from 3 devices and 8 waveguides each) for 405 nm and 635 nm, respectively; which includes loss through all mixer types. This experimental range of total optical loss, 9.64 - 13.7 dB (with 4.2-10.86 % coupling efficiency) translates to an average

output intensity of 1714 mW/mm^2 (360±116 µW output power; mean ±s.d., N=24 from 3 devices and 8 waveguides each) for 405 nm and 2523 mW/mm^2 (530±49 µW output power; mean ±s.d., N=24 from 3 devices and 8 waveguides each) for 635nm at the waveguide tip. This is similar to what was reported for single-shank optoelectrodes in Chapter 3, confirming good alignment accuracy of ILD-GRIN design for multi-shank assemblies. The details of misalignment tolerance analysis on optical efficiency of the GRIN-based optoelectrode [5] is presented in Chapter 3. The wide misalignment tolerance range offered by the GRIN lens helps to maintain reproducible device yield in a mass production.

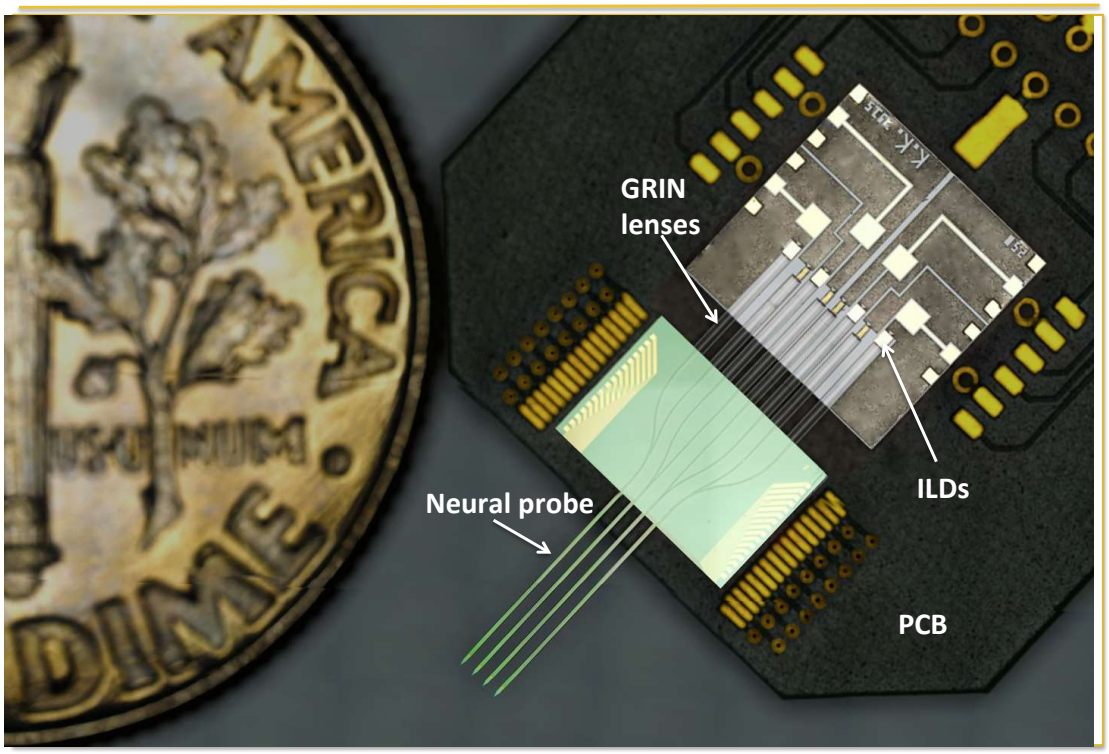

Figure 5-11. Assembled multi-shank ILD-GRIN optoelectrode prototype on a PCB, compared to a dime in size.

5.3.3 Impedance and noise measurements

In vitro impedance and electrical noise measurements were done in phosphate

buffered saline (PBS, 0.1 M, Fisher Scientific, Hampton, New Hampshire, USA) with an RHD2164 amplifier board connected to an RHD2000 Evaluation System (Intan technologies, Los Angeles, CA, USA). The average impedance of recording sites (140 μm^2) was 514 ± 107 kΩ with 65±3° phase at 1 kHz (mean ± s.d., N=5 devices, total 154 working sites), which is sufficiently low to record neural signals with high signal-to-noise ratio. The average baseline noise picked up by the recording channels in absence of light stimulation was 8.92 ± 0.45 μV peak-to-peak (mean ± s.d., N=5 devices, total 154 working sites). The stimulated-locked artifacts on recording channels of second-generation optoelectrodes measured 75/29/50 μV (onset/DC/offset) for 405 nm ILD (30 mA current) and 48/11/-19 μV (onset/DC/offset) for 635 nm ILD (40 mA current). The details of these measurements are discussed in Chapter 4.

5.4 *In vivo* electrophysiological results: Novel circuit effects

Packaged four-shank neural probes with 4 dual-color waveguide ports and 32 recording sites were used to record neural activity in awake head-fixed mice. Recordings were obtained from dorsal CA1 of head-fixed awake PV-Cre mice, which had previously been injected with AAV's encoding CaMKII promoter driven ChR2 and Cre-dependent ChrimsonR, yielding expressing in pyramidal neurons and PV+ interneurons, respectively.

Spontaneous neural activity was recorded on all shanks while the light-modulated neuronal activity was observed on the illuminated neural shanks (**Figure 5-12**). 405 nm pulse illumination (100 ms; 40 mA, 200 μW) elicited spiking in a subset of the pyramidal neurons, while different levels of 635 nm pulse illumination

(300 ms); low power (45 mA, 340 µW), medium power (50 mA, 420 µW), high power (55 mA, 500 µW) elicited spiking in a subset of cells (putative PV interneurons) recorded on the same stimulated shank (**Figure 5-13**). All PYR showed

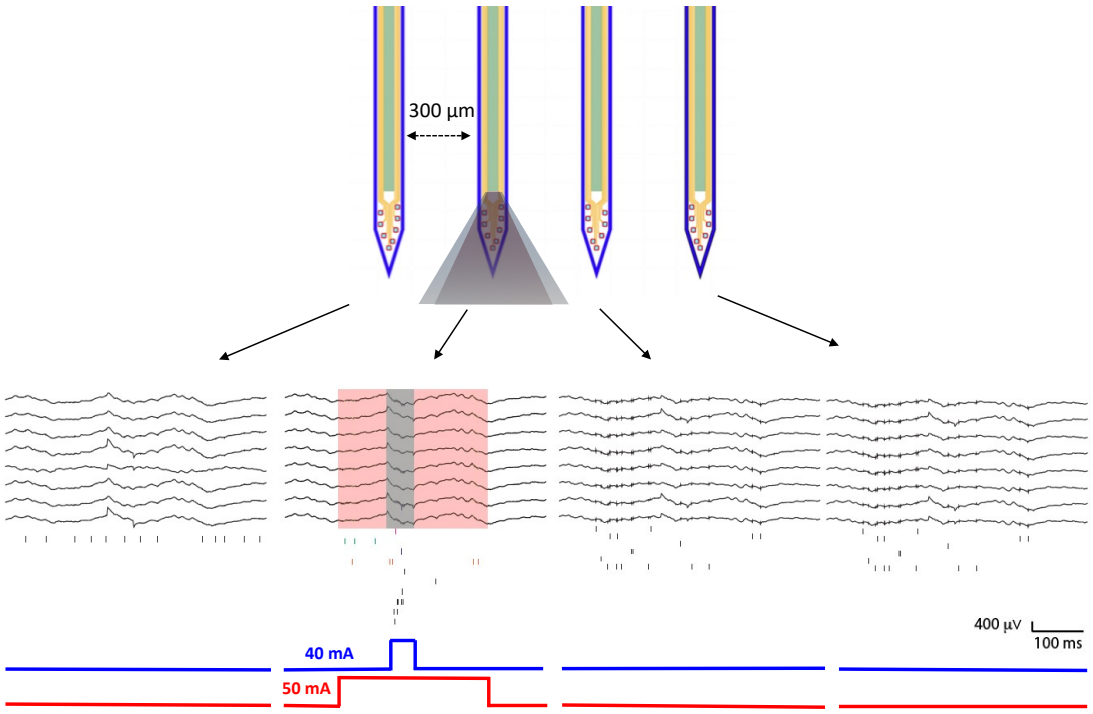

Figure 5-12. Wide-band (0.1-7,500 Hz) spiking activity recorded on a four-shank probe from CA1 pyramidal cell layer of an awake mouse expressing ChR2 in pyramidal cells and ChrimsonR in parvalbumin expressing cells (interneurons). The illuminated shank shows spiking activity during a 200 µW 405 nm light pulse (100 ms, 40 mA) and 450 µW 635 nm light pulse (300 ms, 50 mA). Note spontaneous activity on all shanks and induced spiking during ILD driving on illuminated shank. When simulated in our thermal model, the device can be driven for up to ~27 continuous seconds when driving 2 ILDs on the same shank with a total input electrical power of 320 mW (40mA x 5V for 635 nm + 50 mA x 2.4 V for 405 nm).

robust response to 405 nm light stimulation and no response to 635 nm light stimulation (**Figure 5-13**, pink cell). The two putative PV interneurons (**Figure 5-13**, green and orange cell) showed increasing spiking response to different levels of 635 nm illuminations and also to 405 nm stimulation. These cells were found to be in a monosynaptic connection with two other ChR2 expressing PYR cells (**Figure 5-13**,

light blue and dark blue cell) presumably making excitatory synapses with PV and hence responsible for their firing response during 405 nm stimulation. One more

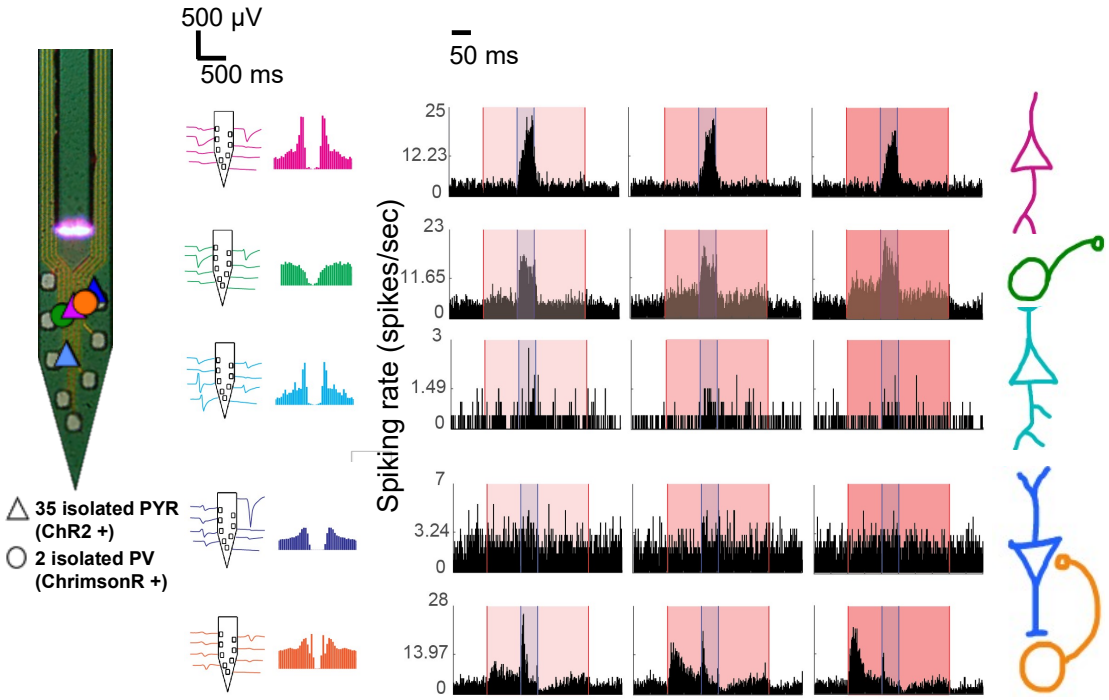

Figure 5-13. Independent multicolor excitation of pyramidal neurons (PYR) and interneurons (PV). The spiking data was quantified for 37 well-isolated cells (35 PYR and 2 PV interneurons) recorded simultaneously from CA1 (same animal and session as in Figure 5-12). Inset of the probe tip shows the vertical location of five light-modulated cells (3 PYR and 2 PV) relative to the probe sites. Plots in the center show auto-correlation histogram and spike waveform (mean and SD) in the lack of any illumination. Histogram plots on the right show spiking response to 50 ms long 405 pulses and 400 ms long 635 nm pulses (for three different intensities) in a ChR2+ PYR, and two monosynaptic pairs of ChR2+ PYR and a ChrimsonR+ PV. Note the excitatory synapse from light blue to green cell and from dark blue to orange cell. Also note the synaptic inhibition of the evoked spiking in the interneuron (orange cell) by higher intensity of 635 nm illumination.

interesting effect observed for one of the monosynaptic pairs (**Figure 5-13**, dark blue and orange cell) was that increasing intensity of 635 nm illumination reduced the spiking rate of the PV interneuron (**Figure 5-13**, orange cell) within 405 nm illumination period; suggesting that the interneurons synaptically inhibit the PYR (**Figure 5-13**, dark blue cell) in this pair. This synaptic inhibition results in reduced

spiking of PYR, which in turns reduces the excitatory input to PV. Such effects are interesting to observe as they provide useful insights about potential synaptic connections between different cell types in a given local circuit.

The results from our previous *in vivo* study in Chapter 3 indicated that red light power of about 400 μW (range, 50-500 μW) was only partially effective at silencing spiking of nearby eArch3 neurons. Given the observation that optical silencers require higher light intensity than ChR2 [1], [21], [22], our current animal preparation was designed to have ChrimsonR+, a red-shifted channel rhodopsin, instead of a silencer like eArch3 or eHalo. The results in **Figure 5-13** show clear light-mediated modulation of ChrimsonR+ with various levels of red light output, ~300-500 μW range, indicating better responsiveness of ChrimsonR+ to red light than eArch3 or eHalo. The light-modulated increase in spiking activity was observed to be fairly localized through the length of illuminating shank only (**Figure 5-14**), verifying two things. First, the waveguide light cone is narrow enough for the shanks to have no apparent light-crosstalk between them. Second, the light intensity as low as 70 μW at the waveguide output is high enough to illuminate up to 200 μm of tissue depth.

As reported in Chapter 4, we recorded 120/-95 μV (onset/offset) artifacts for 200 μW violet-light 40 mA square pulse stimulation (50 ms), <50 μV artifacts for 450 μW red light illumination 50 mA square pulse stimulation (300 ms), and transient-free recording for 200 μW violet-light 40 mA half-sine stimulation (Chapter 4, **Figure 4-10**). We also observed no significant change in artifact magnitude 56 days post-implantation. Our circuit model results in Chapter 4 indicate that artifacts magnitude increases with increase in electrode impedance. We observed only 30.45%

absolute change in impedance (with standard deviation of 29.61 kΩ) across 31 channels after 56 days of implantation. This could be a possible reason for no significant change in artifact magnitude; suggesting good utility of these probes for long-term low-noise chronic recordings.

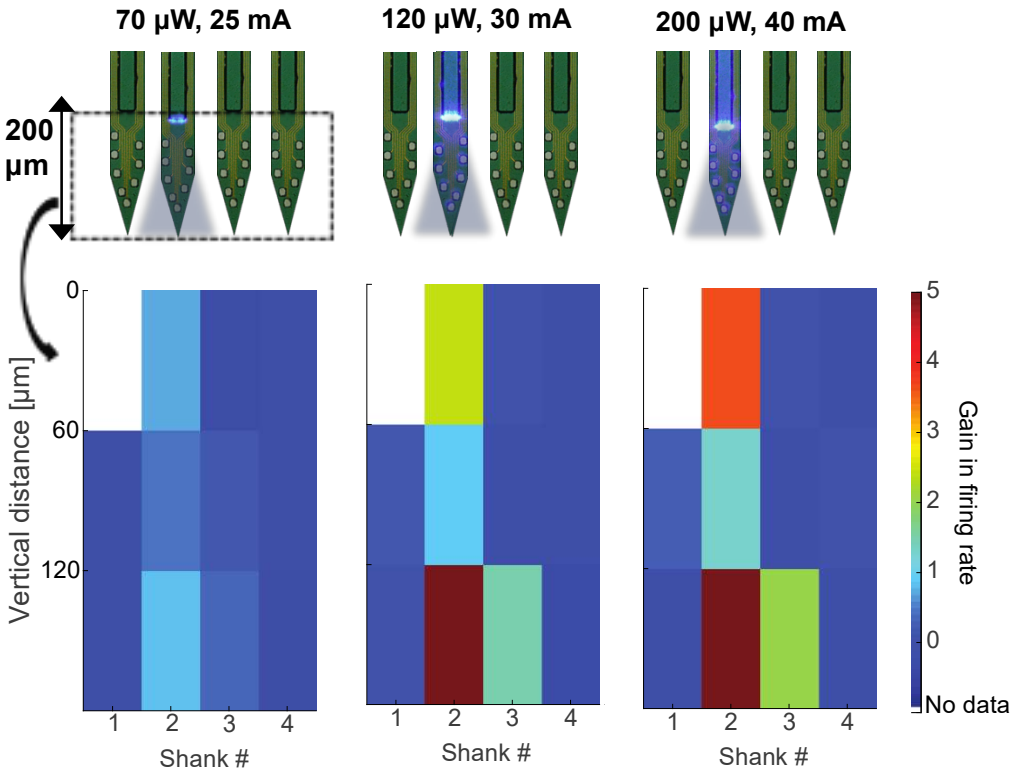

Figure 5-14. Mean firing rate gain as a function of shank number and vertical distance (waveguide site at 0 µm) when shank 2 is illuminating 405 nm light while other shanks have no light on them. Each sub plot if for a different power level of 405 nm at the waveguide tip. As simulated in Figure 3-3, the plots show the capability of ILD-GRIN probes to stimulate tissue depths of up to ~200 µms. The gain in firing rate seen at the bottom of shank 3 could be because of possible crosstalk or synaptic connections between neurons recorded on shank 2 and shank 3.

5.5 Conclusion

In this chapter, we demonstrated design, fabrication and high-density packaging of ILD-GRIN optoelectrodes for multicolor neural stimulation and low-noise recording. While facilitating thermal protection and adequate electrical noise

shielding at device backend, our effective diode packaging solution also enabled precise assembly of optical components with wide alignment tolerance. We were able to achieve high optical efficiency range of 4.2-10.86% for the assembled working prototypes. Having total of 4 optical sites with 2-color control at each, this tool can independently and simultaneously manipulate the spike timing of different cell types at 4 precise locations with an illumination depth of up to ~200μm at each site.

Multi-opsin optogenetic studies require careful selection of opsins and matching light wavelengths during device design. We chose 405nm over 470 nm light (usually used for ChR2 activation) because of its low sensitivity of Chrimson (activated here with 635 nm light), facilitating minimum crosstalk between excitation spectrums of the opsins. For the first time, to our knowledge, this work demonstrates optical excitation of distinct neural populations *in vivo* at precise locations within a local recording volume of tissue. This proves the utility of these devices for circuit interrogation applications that require the parametric control of two types of neurons or the bidirectional control of a single cell type in awake animals. With this new capability, we can now possibly identify distinct roles of various genetically modified excitatory and inhibitory cells and understand how they communicate within a given local neural circuit. This could not be possible before with electrical stimulation methods or mono-color optogenetic methods. Altogether, the presented technology will considerably help to advance our understanding of neural computation and unravel the local neuronal network dynamics.

References

[1] E. Stark, T. Koos, and G. Buzsáki, "Diode probes for spatiotemporal optical control of multiple neurons in freely moving animals.," *J. Neurophysiol.*, vol. 108, no. 1, pp. 349–63, Jul. 2012.

[2] T. Kim, J. G. McCall, Y. H. Jung, X. Huang, E. R. Siuda, Y. Li, J. Song, Y. M. Song, H. A. Pao, R.-H. Kim, C. Lu, S. D. Lee, I.-S. Song, G. Shin, R. Al-Hasani, S. Kim, M. P. Tan, Y. Huang, F. G. Omenetto, J. A. Rogers, and M. R. Bruchas, "Injectable, Cellular-Scale Optoelectronics with Applications for Wireless Optogenetics," *Science (80-.).*, vol. 340, no. 6129, pp. 211–216, Apr. 2013.

[3] F. Wu, E. Stark, P. C. Ku, K. D. Wise, G. Buzsáki, and E. Yoon, "Monolithically Integrated μLEDs on Silicon Neural Probes for High-Resolution Optogenetic Studies in Behaving Animals," *Neuron*, vol. 88, no. 6, pp. 1136–1148, 2015.

[4] R. Scharf, T. Tsunematsu, N. McAlinden, M. D. Dawson, S. Sakata, and K. Mathieson, "Depth-specific optogenetic control in vivo with a scalable, high-density μLED neural probe," *Sci. Rep.*, vol. 6, no. January, p. 28381, 2016.

[5] K. Kampasi, E. Stark, J. Seymour, K. Na, H. G. Winful, G. Buzsáki, K. D. Wise, and E. Yoon, "Fiberless multicolor neural optoelectrode for in vivo circuit analysis," *Sci Rep, Nat. Publ. Gr.*, vol. 6, p. 30961, 2016.

[6] M. Schwaerzle, P. Ringwald, O. Paul, and P. Ruther, "First dual-color optrode with bare laser diode chips diecrtly butt-coupeld to hybrid-polymer waveguides," in *MEMS*, 2017, vol. 2, pp. 26–29.

[7] K. Kampasi, D. F. English, J. Seymour, S. McKenzie, E. Stark, K. D. Wise, G. Buzsaki, and E. Yoon, "Independent optogenetic control of distinct neural populations using low-noise fiberless optoelectrodes," (unpublished).

[8] K. Kampasi, J. Seymour, K. Na, K. D. Wise, and E. Yoon, "Fiberless multicolor optoelectrodes using Injection Laser Diodes and Gradient-index lens coupled optical waveguides," in *Proceedings of the 18th International Conference on Solid-State Sensors, Actuators and Microsystems (TRANSDUCERS)*, 2015, pp. 273–276.

[9] R. G. Hunsperger, *Integrated Optics*. Springer-Verlag New York, 1984.

[10] E. A. J. Marcatilli, "Bends in optical dielectric waveguides," *Bell Syst. Tech. J.*, vol. 48, no. 7, pp. 2103–2132, 1969.

[11] F. Wu, E. Stark, M. Im, I.-J. Cho, E.-S. Yoon, G. Buzsáki, K. D. Wise, and E. Yoon, "An implantable neural probe with monolithically integrated dielectric waveguide and recording electrodes for optogenetics applications.," *J. Neural Eng.*, vol. 10, no. 5, p. 56012, Oct. 2013.

[12] G. Nagel, T. Szellas, W. Huhn, S. Kateriya, N. Adeishvili, P. Berthold, D. Ollig, P. Hegemann, and E. Bamberg, "Channelrhodopsin-2, a directly light-gated cation-selective membrane channel.," *Proc. Natl. Acad. Sci. U. S. A.*, vol. 100, no. 24, pp. 13940–5, 2003.

[13] A. M. Aravanis, L.-P. Wang, F. Zhang, L. a Meltzer, M. Z. Mogri, M. B. Schneider, and K. Deisseroth, "An optical neural interface: in vivo control of rodent motor cortex with integrated fiberoptic and optogenetic technology.," *J. Neural Eng.*, vol. 4, no. 3, pp. S143–S156, Sep. 2007.

[14] N. C. Klapoetke, Y. Murata, S. S. Kim, S. R. Pulver, A. Birdsey-benson, Y. K. Cho, T. K. Morimoto, E. J. Carpenter, Z. Tian, J. Wang, Y. Xie, Z. Yan, Y. Zhang, B. Y. Chow, B. Surek, M. Melkonian, V. Jayaraman, M. Constantine-paton, G. K. Wong, E. S. Boyden, S. N. Group, C. Sciences, and C. Biocenter, "Independent Optical Excitation of Distinct Neural Populations," vol. 11, no. 3, pp. 338–346, 2014.

[15] K. Kampasi, J. Seymour, E. Stark, G. Buzsáki, K. D. Wise, and E. Yoon, "Efficient assembly of multi-color fiberless optoelectrodes with on-board light sources for neural stimulation and recording," *Conf. IEEE Eng. Med. Biol. Soc.*, pp. 4479–4482, 2016.

[16] K. D. Wise, "Silicon microsystems for neuroscience and neural prostheses," *IEEE Eng. Med. Biol. Mag.*, vol. 24, no. 5, pp. 22–29, Sep. 2005.

[17] T. Hayashi, "An innovative bonding technique for optical chips using solder bumps that eliminate chip positioning adjustments," *IEEE Trans. components, hybrids, Manuf. Technol.*, vol. 15, no. 2, pp. 225–230, 1992.

[18] Q. Tan and Y. Lee, "Soldering Technology for Optoelectronic Packaging," *1996 Electron. Components Technol. Conf.*, pp. 26–36, 1996.

[19] V. C. R. Boudreau, M. Tabasky, C. Armiento, A. Bellows and and P. H. R. Morrison, M. Urban, R. Sargent, A. Negri, "Fluxless Die Bonding for Optoelectronics," *Electron. Components Technol. Conf. Proceedings., 43rd*, pp. 485–490, 1993.

[20] E. Wolak, C. Mitchell, T. Crum, O. Romero, J. Gloyd, D. Liu, S. Cutillas, S.-K. Park, K. Johnson, X. Jin, H. Li, T. Towe, I. Chyr, R. Miller, A. Meissner, D. Lenarduzzi, and J. Harrison, "Advances in high-power laser diode packaging," in *Photonics Packaging, Integration, and Interconnects IX*, 2009, vol. 7221, p. 72210U.

[21] V. Gradinaru, F. Zhang, C. Ramakrishnan, J. Mattis, R. Prakash, I. Diester, I. Goshen, K. R. Thompson, and K. Deisseroth, "Molecular and Cellular Approaches for Diversifying and Extending Optogenetics," *Cell*, vol. 141, no. 1, pp. 154–165, 2010.

[22] J. Mattis, K. M. Tye, E. a Ferenczi, C. Ramakrishnan, D. J. O'Shea, R. Prakash, L. a Gunaydin, M. Hyun, L. E. Fenno, V. Gradinaru, O. Yizhar, and K. Deisseroth, "Principles for applying optogenetic tools derived from direct comparative analysis of microbial opsins," *Nat. Methods*, vol. 9, no. 2, pp. 159–172, 2011.

Chapter 6

Understanding Failure Mechanisms for Implantable Neural Probes

6.1 Introduction

In last few decades, implantable microelectrode technologies have supported advanced neuroscience research towards functional mapping of the neural circuitry, paving way for an encouraging future for clinical neural implants [1], [2]. But despite promising results during acute recordings, implantable neural probes often fail to function reliably in clinically relevant chronic settings [3]–[5]. While chronic viability is imperative for both clinical uses and animal experiments, achieving one is a major technological challenge due to the chronic foreign body response to the implant (**Figure 6-1**).

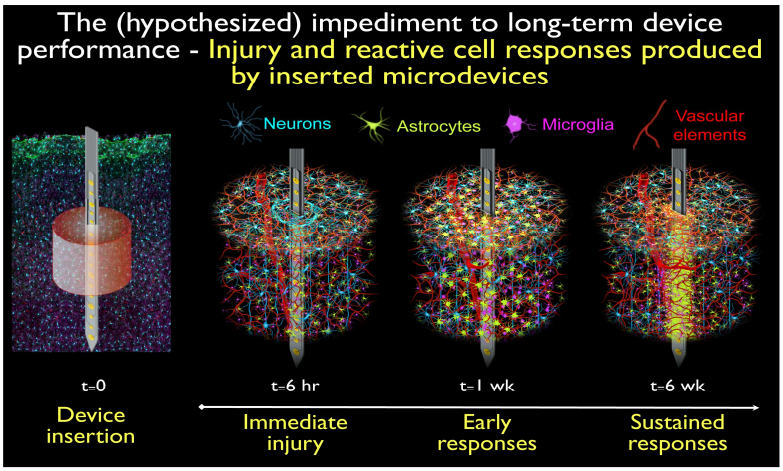

Figure 6-1. Diagrammatic representation of typical inflammatory foreign body tissue response developed around an implant over a period of weeks [Center for Neural Communication Technology, U of M].

6.2 Potential design strategies to mitigate local tissue response

Though foreign body reactions are inevitable and the neural recording quality typically degrades over time, several design strategies could be implemented to mitigate the tissue damage over time and enhance the lifetime of electrodes. Neural probes with lattice structures can help to reduce surface area to minimize protein adsorption, which can lead to downstream immunoreactions [6], [7] (**Figure 6-2a-b**). It has been shown that the local tissue reaction intensities are proportional to the implanted device size [8]–[11]. Other studies have demonstrated that flexible material probes can help to reduce tissue damage caused by the relative micro-motion between brain and implanted devices [12], [13] (**Figure 6-2c-d**).

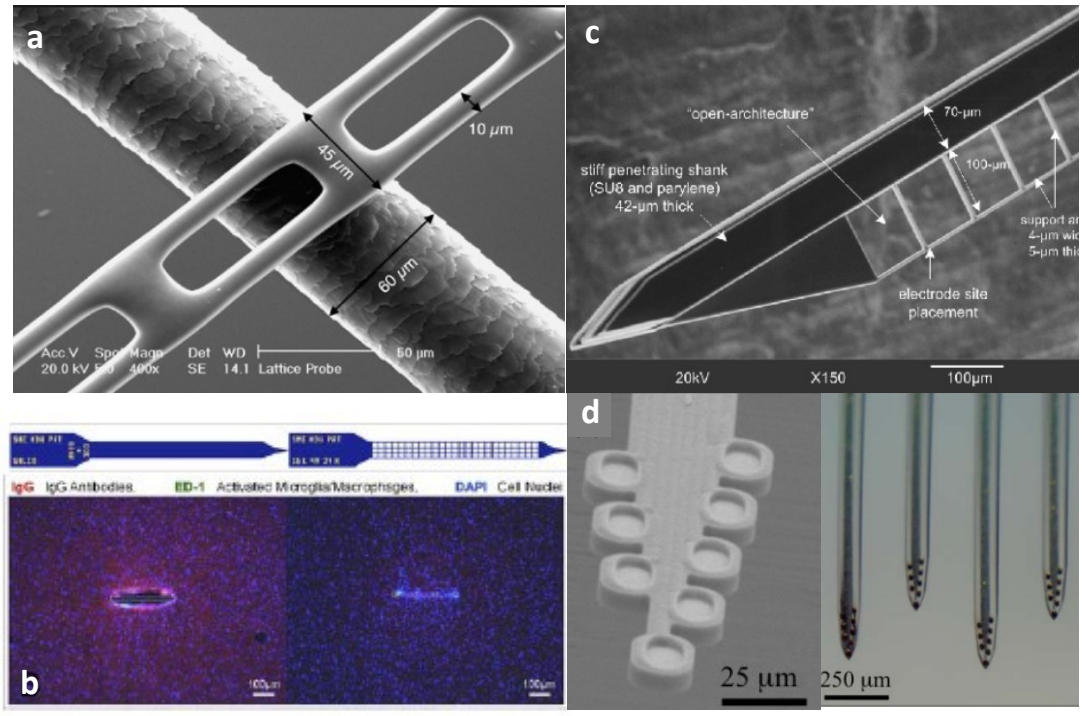

Figure 6-2. Neural probes built at Michigan with modified probe geometries and flexible materials to reduce tissue reactions near the recording electrodes for chronic applications. (a, b) Lattice probes[6], [7] (c, d) Polymer probes [10], [14].

A more recent study from Michigan reported the use of bio-dissolvable silk

substrates for the design of flexible parylene neural implants (**Figure 6-2d**) [14]. The silk is used to provide temporary mechanical stiffness to parylene-C probes during insertion and is supposed to eventually get dissolved in the enzymatic tissue environment. The work validated successful insertion of 4-shank, 64-sites probes reporting robust spiking activity post 6-weeks of implantation in rodents. However, it provided limited evidence of biocompatibility of silk fibroin in brain tissue. In order to investigate this further, we defined the following study to compare the immunohistological response of brain to silk-backed polymer probes as compared to silicon probes of same dimensions and structure [15].

We fabricated single shank silicon probes (**Figure 6-3a**) with exact same dimensions as the silk-backed parylene implants (**Figure 6-3b**) [14]. Each probe type was implanted in one of the cerebral hemispheres (one probe type in one hemisphere) of the same adult Long Evans rat (n=2). Both the devices were implanted in the same animal to reduce variability of tissue response from animal to animal.

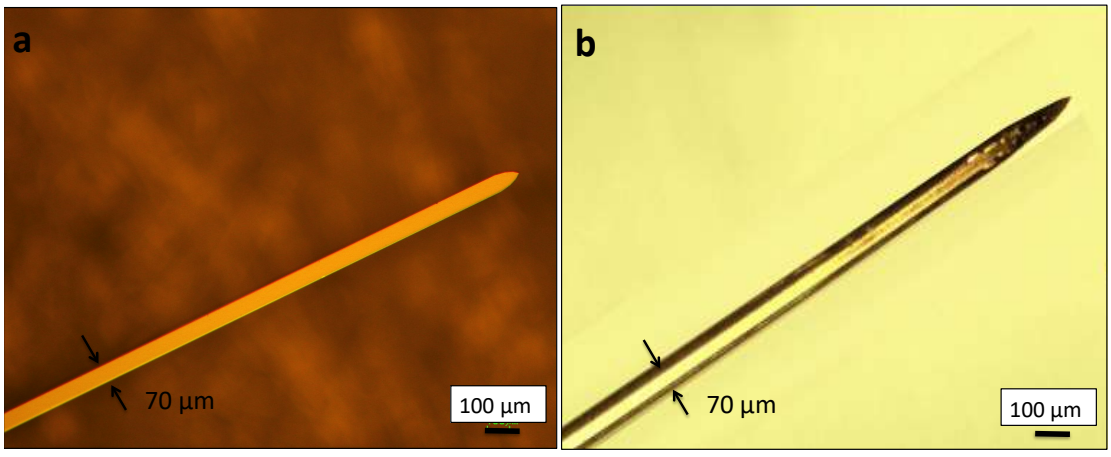

Figure 6-3. Microscope images of fabricated (a) silicon probe and (b) silk-backed polymer probe used for comparative study of foreign body response to both types of probes.

After 12 weeks, the brain samples with the embedded probes were extracted

(without explanting the probes from the tissue) and prepared for histological analysis. The details of histology protocol are listed in **Appendix E**. The cell markers used for this study were anti-GFAP (Glial Fibrillary Acidic Protein) and anti-NeuN (Neuronal Nuclei) (**Table 6.1**). All sections were also counterstained with DAPI to mark all the cell nuclei. Six transverse tissue sections along the length of the probes (2 mm) were randomly chosen for image analysis around each probe tract. The distribution of cell biomarkers around different types of probes was compared. **Figure 6-4** shows the representative images from a control tissue site (no implant), a silk-coated probe site, and a silicon probe site, respectively, at 12-weeks post-implantation period [15].

Table 6.1. Primary antibodies used for staining major cell types in immunohistological of brain tissue.

Antibody/Stain	**Antigen**	**Cell Type(s)**
GFAP	Glial fibrillary acidic proteins	Astrocytes
EDI	Lysosomal glycoprotein	Microglia, macrophages
NeuN	Neuronal nuclei	Neurons
Neurofilament-160	Medium neurofilament polypeptide	Neurons
EBA	Endothelial membrane	Vasculature
Hoechst/DAPI	Nuclear Acid	All cell nuclei

The confocal image of the control tissue site showed the presence of healthy neuronal cell nuclei with normal astrocyte (GFAP+) distributions. The cell response around silicon was consistent with the histology results of other comparable types of chronic microelectrode implants [9], [25-26]**,** showing a high density GFAP+ immunoreactive zone within 50-μm-radius around the implant. Qualitatively, GFAP+ fluorescence around the silk-coated probe appeared much less intense than that

around the silicon probe.

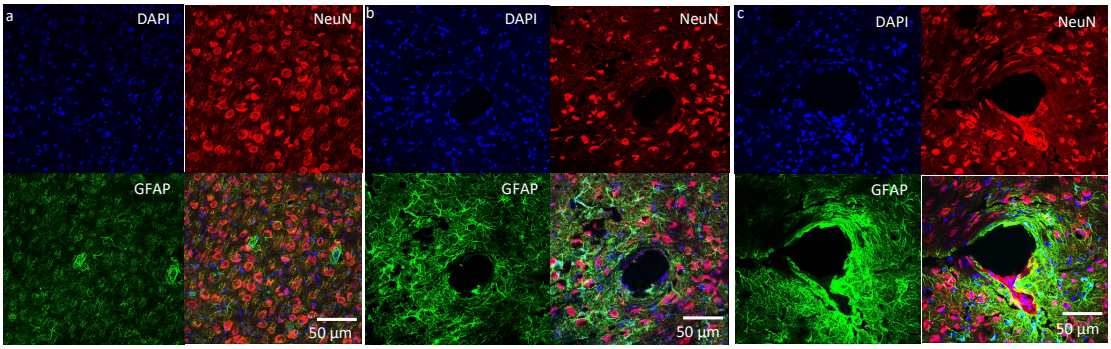

Figure 6-4. Histology results showing 12-week post-implantation immunoreactivity response: (a) healthy cortical tissue; (b) silk-backed parylene probe; (c) silicon probe. These representative 40X confocal immuno-fluorescent images from the same tissue section qualitatively depict a more reactive tissue response (GFAP (green), NeUN (red) and DAPI (blue)) around the silicon probe as compared to the silk-backed parylene probe.

However, further studies are required to understand if the reduced tissue immune response is repeatable, and if so is the response a function of reduced material density of the implant as reported by others; or is it a function of the a smaller, more flexible foreign body. It is still inconclusive whether the new design has significantly improved the reliability of recording. Such comparison may require extensive studies under carefully controlled experiments, as there are often multiple design parameters, insertion methods, and even differences among animals that can affect the recording quality. Nonetheless, the preliminary histology results presented in this study look encouraging as they provide for the first-time *in vivo* evidence of biocompatibility of silk-coated implants in the central nervous system.

6.3 Prediction of neural interface failure using Bi-directional optrode

Efforts have sought to understand the mechanisms leading to a failure of recordings with time using quantitative histology [16], [17] as is also reported above.

Unfortunately, histological assessment can only be performed once per animal, and cannot be scaled to on-line measurements, slowing the process of understanding these complex failure mechanisms. On the other hand, impedance spectroscopy provides an online readout, but gives almost no insight into the cellular morphologies of degradation [18], [19]. Finally, cortical imaging of acute microgliosis around an implanted neural probe has been demonstrated using transparent windows positioned in the cranium [20]. Tissue features can be imaged to depths of 300-500 μm, but are unable to image deeper structures such as pyramidal cell bodies [21]–[23].

6.3.1 Rationale and approach

The focus of this work is to develop a bi-directional Optrode (optical electrode), which can transmit light through excitation apertures into neural tissue and collect light perturbed by the tissue, as a means of obtaining a real-time histological snapshot of the tissue properties [24]. In contrast to neural optoelectrodes used for optogenetic studies, where spatially targeted light delivery enables neural activation and silencing, this work seeks to develop optical source and collection waveguides co-located within a neural probe, which enables measurement of broad-wavelength tissue spectral characteristics (**Figure 6-5**).

It is well known that the spectral content of the optical absorption coefficient provides tissue oxygenation and bruising information [25]–[28]. As such, changes in optical absorption may provide information about micro-hemorrhaging resulting from probe micro-motion or about the dynamics of glial encapsulation due to the chronic presence of the implant. Similarly, the optical scattering coefficient can be used to determine morphometric information (i.e. particle size, density) about tissue micro-

environment. It is hypothesized that optical transmission and diffuse reflectance may also provide a sensitive and an early predictor of changes in microglial and astrocytic accumulation.

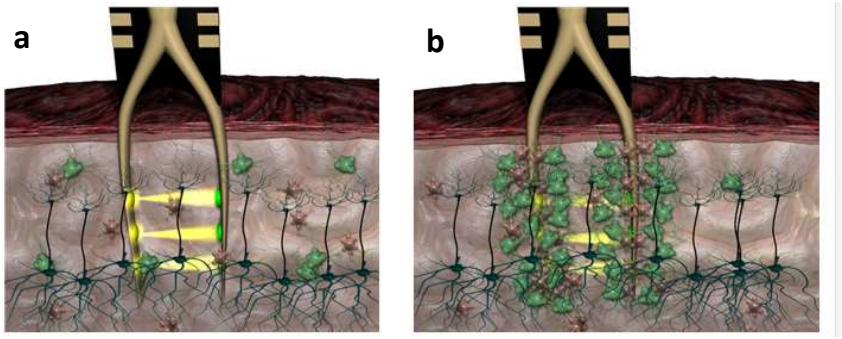

Figure 6-5. Diagrammatic representation of changes in optical transmission between shanks of an optrode implanted in brain cortex. a) Transmission of light from source to collector apertures via brain tissue. b) Reduced transmission of light between source and collector due to increased tissue absorption and scattering resulting from glial encapsulation around the shanks.

6.3.2 Preliminary studies

The proof of concept for optrode design was tested in liquid tissue phantoms. The phantoms were created from 1 μm polystyrene spheres (Bangs Laboratories) and India ink. The size of spheres and concentrations were simulated (using Mie calculator) to create phantoms with different absorption and scattering coefficients representative of different stages of a glial sheath in neural interface failure. These optical properties represent a range of scattering around published values for grey matter [26], [29], [30].

For the preliminary experiments, phantom tissue scattering coefficient was varied from 1 to 125 mm^{-1} and phantom absorption coefficient was varied from 0.01 to 0.5 mm^{-1} **(Figure 6-6)**. An optical transmission change greater than 40 dB was observed across optical scattering range. However, only 1 dB optical change was

measured due to absorption. The results are summarized in **Figure 6-7.**

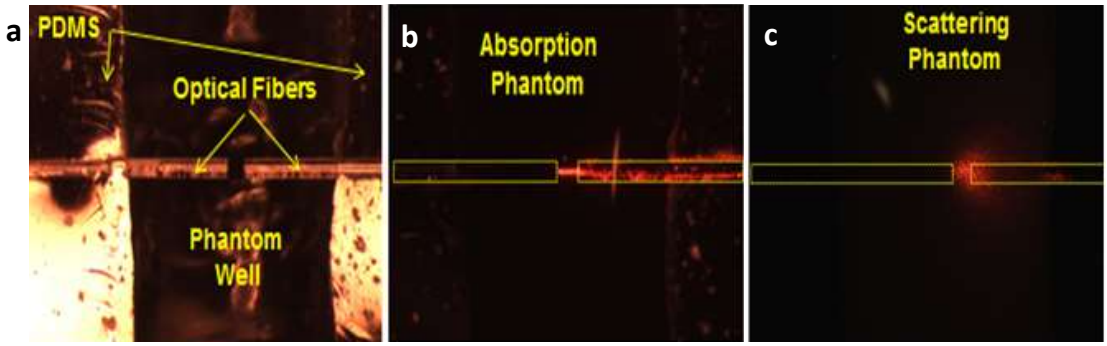

Figure 6-6. Optical source and collection fibers aligned end to end within liquid phantom well with a 104um gap in between them. (a) PDMS mold was used to maintain a good alignment between 25/125 um optical fibers across the well. Optical transmission loss was measured for different values of absorption (a) and scattering (b) coefficients. [Draper Laboratory].

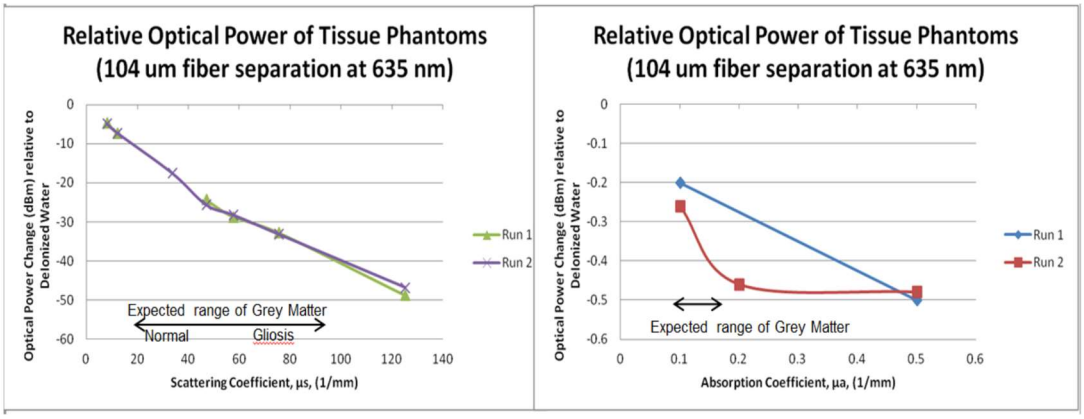

Figure 6-7. Optical transmission as a function of scattering and absorption coefficients. Results demonstrate a clear optical signal reduction over the range of scattering coefficients of brain, from normal to glial tissue.

6.3.3 Design and fabrication

Summing up the observations from preliminary experiments, it was evident that a reduction in optical transmission through the neural tissue due to increased absorption and scattering may be a measure of the distribution of tissue state. To detect this decrease in light intensity, we need at least one source and collector, deep inside the tissue to be studied. The reduction between the light intensity emitted by

the source and collected by a collector, called attenuation, can be calibrated to estimate the extent of neural firing or tissue damage. If an input power P1, from the optrode source site results in an attenuated output power P2 at the optrode collector site, the attenuation or power loss, α, can be calculated by the following equation, $\alpha\ (dB) = 10 \log10\ (P1/P2)$.

The implantable optrodes were designed to maximize the optical collection efficiency (determined by the cross-sectional area of the waveguide) against the tissue insertion damage from a greater shank thickness. Two contiguous shanks have a 25 μm square waveguide embedded in them and feature a 45° mirror to direct the light beam in a right angle with minimal losses. The waveguide facets are positioned on the inner edges of the shanks so that they face one another. Light is then coupled through one shank aperture, passes through the tissue between the shanks, and collected by the adjacent shank aperture. A third waveguide calibration-loop is embedded in the main body of the probe, which enables the source to be coupled to the detector via the neural probe, without interacting with the tissue. The calibration loop provides a fixed optical path, which provides a baseline measure of source intensity, detector drift, or coupling changes between recording sessions. Tissue measurements are hence normalized to the calibration loop for each session.

Optrodes were fabricated based upon the optimized processes developed for Michigan silicon probes (**Figure 6-8a)** [31]. Cr/Au metal was patterned using liftoff to define electrode sites, traces, and bond-pads. A 10 μm layer of Polydimethylsiloxane (PDMS, Sylgard 184, Dow Corning) was spun-on to insulate the electrodes and serve as the waveguide under-cladding. Oxygen plasma was used

to activate the PDMS surface as an adhesion promoter. An epoxy-based photoresist, SU8-3025 (MicroChem, Newton MA), was spin-coated to form a 25 µm layer, and subsequently exposed and developed to define the waveguides structures.

A resist mask was created to lift off a 0.5 µm layer of sputtered aluminum, to create a mirror for the waveguide corner reflectors. A 35 µm layer of PDMS was then spun-on to cover the SU8 waveguides and serve as the upper cladding. A mask was applied using a 1 µm aluminum hard mask and 18 µm of AZ9260 photoresist (Microchemicals, GMBH). Reactive ion etching (RIE) using SF_6/O_2 was used to etch through the 40 µm layer of PDMS [17]. A handle wafer was attached to the top side of the wafer, and photo resist was patterned on the backside of the wafer within 1-2 µm of tolerance to etch the silicon substrate using a STS-DRIE system to isolate the devices at die scale. Finally, devices were released acetone-IPA soak (**Figure 6-8b)** [24].

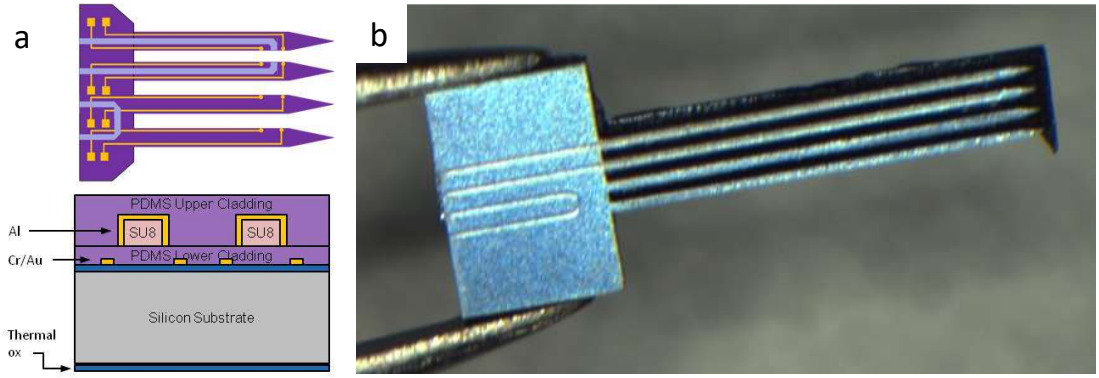

Figure 6-8. Fabricated Optrode showing built-in waveguides in contiguous shanks and a U-shape calibration waveguide. Adjacent shanks are 125 µm apart and 10 mm long. a) Schematic. b) Released device [24]

6.3.4 Assembly and integration

A printed circuit board (PCB) was used as a substrate to bond Optrodes,

Omnetics nano-strip connector, and detachable optical fiber mechanical transfer (MT) connector. The four-fiber MT connector was aligned to the Optrode apertures using dual XYZ translation stages and goniometers. The calibration waveguide was used to determine peak coupling during the alignment process. A fully assembled hybrid Optrode with MT connector and electrode is shown in (**Figure 6-9**).

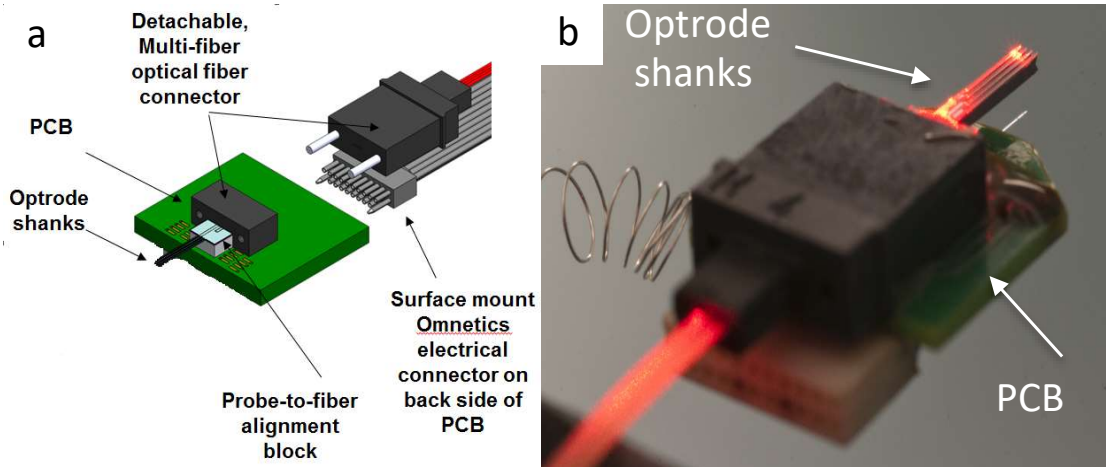

Figure 6-9. a) Diagrammatic representation of Bi-directional optrode design model showing its different components. b) Assembled four-shank optrode with lighted optical sites. The long coiled lead is for grounding the circuit to a skull screw [24].

6.3.5 *In vitro* results

Tissue liquid phantoms were prepared using various concentrations of 1 μm polystyrene spheres (Bangs Laboratories) in water, calculated to have scattering coefficients from 10-200/mm [29]. A 20W white light optical source (Ocean Optics, HL-2000-HP-FHSA) was connected to the source optical fiber. The collection fiber was coupled to a monochromator (Princeton Instruments, 2300i) for spectroscopic collection and a ten-second integration time was used given that the source-fiber coupling and fiber coupling losses result in only tens of micro-watts of optical power reaching the source aperture. **Figure 6-10** shows the spectral change in measured

optical transmission by an Optrode through the various tissue phantoms.

Monte-Carlo multi-layer [32] was used to optimize the waveguide aperture diameter and optical collection efficiency. For a tissue scattering coefficient of μs = 20 mm^{-1} (normal grey matter), the optical transmission between 26 μm apertures separated by 100 μm was 51%. An increase in μs to 50 mm^{-1} (estimated gliosis) resulted in a 19% transmission. Assuming a 50 μW optical source power at the excitation aperture, μW-scale sensitivity is desirable to provide a 1000x margin with a silicon detector and amplifier noise floor. A larger aperture separation may be more sensitive to tissue changes, but would result in signals more difficult to detect.

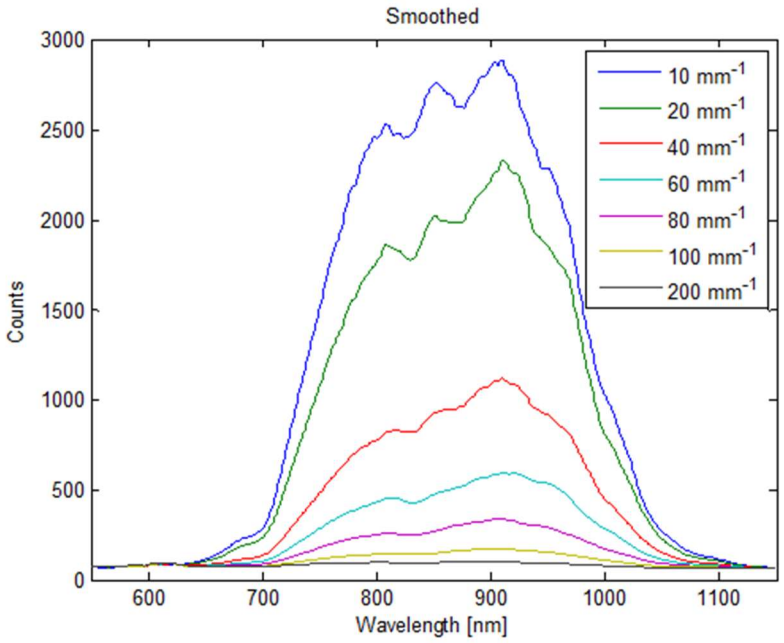

Figure 6-10. Optrode transmission spectra of tissue simulating phantoms of various optical scattering coefficients mimicking a range of grey matter properties [24].

6.3.6 Pilot *in vivo* results

Animal procedures were administered according to the University of Michigan Institutional Animal Care and Use Committee. The Optrodes were implanted 2 mm

deep into the primary somatosensory cortex adult Long Evan Rats in both acute and chronic (4 weeks) preparations.

For optical measurements, a 2.5 mW and 635 nm, fiber-coupled laser source (S1FC635, Thorlabs) was coupled into a fiber pigtail. Fiber cladding mode-scrambling was achieved using sequential high-bend radius turns in the fibers. The laser amplitude was modulated with a 500 Hz sine wave generator, which was detected using a photodiode (FDS100, Thorlabs) and adjustable selectable precision amplifier (FEMTO Gmbh, DLPCA-200). The photodiode was sampled with an A/D converter module (NI 6909, National Instruments). The amplifier gain for the tissue sample was typically 10^9 and for the calibration loop 10^7. Dark measurements were captured at each amplifier gain setting. Tissue data was captured using a 10 second capture for the tissue followed by the calibration loop. To ensure temporal stability, a subsequent capture was performed where the sample and calibration loop were sequentially interleaved for 500 ms windows in a repeated fashion. A one-sided FFT was integrated from DC to 10 Hz and 495-505 Hz to determine the energy within the 500 Hz modulation band. An optical transmission ratio was computed using the following equation, $\text{Optical integral ratio} = \frac{(\text{PSD}_{500\,\text{Hz}}-\text{Gai}\ )_{\text{TISSUE}}}{(\text{PSD}_{500\,\text{Hz}}-\text{Ga}\ \ )_{\text{CALIBRATION}}}$ to normalize the measured tissue with the calibration loop and the respective gain settings.

Before chronic studies, acute measurements were performed to validate the optrode function *in vivo*. An acute neural inflammatory drug, TNF-alpha (5μL of 1μg/μL concentration) was injected to induce immediate tissue inflammation; and simultaneous optical and electrical measurements were taken over several hours of

time period. The data was collected for two acute animals and is as shown in **Figure 6-11**. The results indicated significant optical signal loss from the tissue waveguide as compared to the calibration waveguide over the period of hours post-implantation. A greater optical loss corresponds to more tissue signal attenuation suggesting more glial encapsulation.

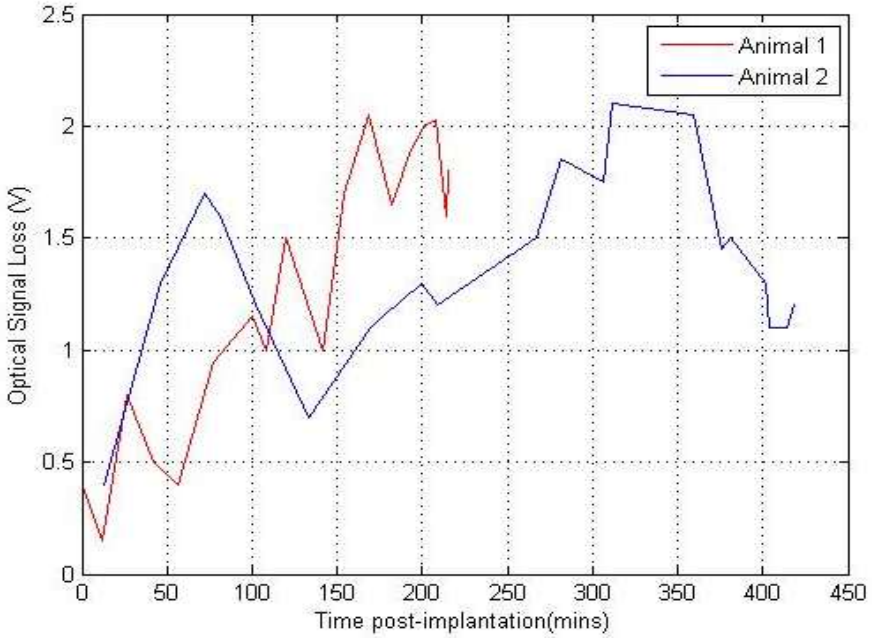

Figure 6-11. Optical Signal Loss (calibration signal minus tissue signal) over time for two acute animals.

For chronic implantations, the procedure mimicked a conventional chronic head mount used for neural probes [16]. **Figure 6-12** shows the measured chronic *in vivo* data at 635 nm. The normalized optical transmission ratio increases over the first few days and begins to fall again, finally settling over weeks after implantation. These changes are expected to arise from variation in tissue absorption and scattering spectra, which are influenced by factors like micro hemorrhaging and tissue oxygenation. The variation in response between different animals could indicate varying extent of tissue injury caused during implantation. Since different

implantation injuries lead to differential post-traumatic bleeding and tissue oxygenation levels, this might result in difference in optical power recorded over time in different animals as could be seen in **Figure 6-12**. The observation from the chronic data could be seen somewhat consistent with the literature suggesting increase in glial post-implantation [16], [18].

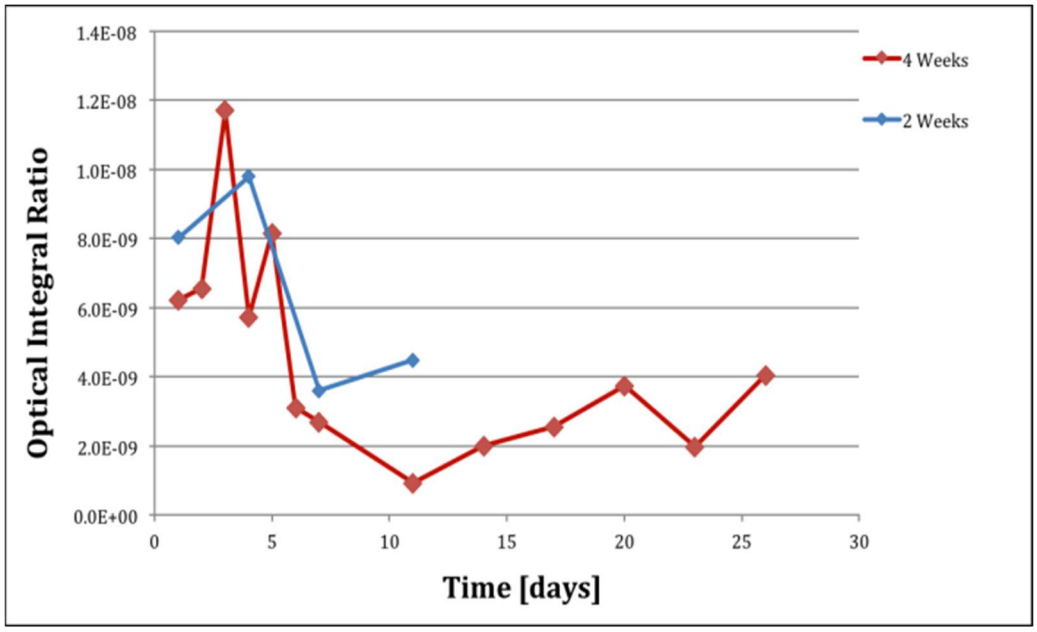

Figure 6-12. Optical integral ratio (at 500 Hz) recorded from animals for 2 weeks and 4 weeks, respectively (measurements taken with 635 nm optical wavelength).

6.3.7 Tissue histology

To examine the association between recorded optical power and tissue immunoreactive responses, animals were perfused post recording periods. Brains from rats were removed and embedded in paraffin blocks to study the tissue reaction post implantation (t = 4 weeks). After sectioning of paraffin blocks with a microtome, immunofluorescent and immunohistochemistry labeling was used to examine neuronal and non-neuronal response around the device. **Table 6.1** lists some primary antibodies and stains that could be used for staining major cell types. We used anti-

IBA1 (Ionized calcium Binding Adaptor molecule 1) to label microglia, GFAP (Glial Fibrillary Acidic Protein) to identify astrocytes, and NeuN (Neuronal Nuclei) to label neurons, and DAPI (4',6-diamidino-2-phenylindole) to stain all cell nuclei. **Figure 6-13** shows the horizontal tissue sections imaged with bright field and confocal microscopy. No neuronal nuclei were observed (**Figure 6-13c)** between the optical shanks of the implant at 4 weeks post implantation, perhaps due to the large size of the optrode compared to conventional silicon-based intracortical microelectrodes [31]. However, we observed many DAPI+ cells (**Figure 6-13d)** at the immediate vicinity of the implant pointing towards a strong glial reaction to the implanted probes. Indeed, we observed an intense IBA-1 and GFAP immunoreactive area within a 100 μm zone surrounding the implant as shown in **Figure 6-13a, b**. The preliminary

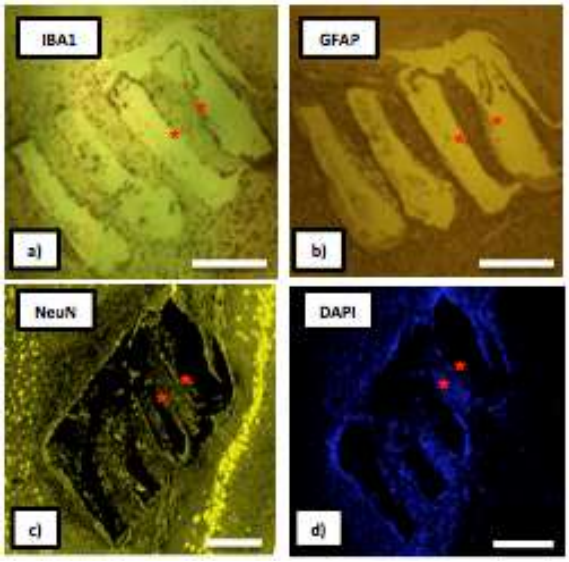

Figure 6-13. Neural tissue response to implanted Optrode after four weeks of implantation. a) IBA-1 labeled microglia, b) GFAP labeled astrocytes, c) NeuN labeled neurons and d) DAPI labeled cell nuclei. Asterisk sign depicts location of optical apertures on Optrode shanks. (Scale = 250 μm).

tissue histology results are consistent with comparable types of chronic microelectrode implants showing intense GFAP and IBA-1 immunoreactive response

with reduced NeuN density surrounding the implants [16], [33]. This increase in cell inflammation and total cell density around the Optrode is expected to be the reason for fall in optical transmission ratio over time as observed in **Figure 6-12**. Further studies are required to investigate detailed association between relevant optical tissue properties with histological details.

6.4 Conclusion

In the first half of the chapter, we presented a pilot immunohistology study to compare the brain tissue response induced by a silicon probe and a mechanically more flexible silk-backed polymer probe in chronic animals [15]. The study provides the first *in vivo* evidence of biocompatibility of silk fibroin in the central nervous system with minimum tissue damage and encourages further exploration of incorporating silk-based delivery systems for brain-machine interfaces. Many other studies have also reported the use of novel flexible materials in bio-interfaces for better tissue compatibility [10], [11], [34], [35]; however flexible materials come with their own set of challenges. First, they are susceptible to water absorption and cracking, making them unsuitable for long-term chronic use. Second, they can absorb significant amount of light at lower wavelengths, an undesirable characteristic for implantable light guides. Therefore, while flexible materials form a promising option for biocompatible brain interfaces, their application for reliable chronic use needs to be further explored.

In the second half of this chapter, we introduced a new optrode technology for spectroscopic analysis of neural tissue damage in real-time and discuss its possible potential as compared to other current state-of-art techniques [24]. We demonstrated

Table 6.2. Comparison of state-of-art tissue assessment techniques with bi-directional optrode.

Feature	**Histology**	**Impedance Spectroscopy**	***In vivo* Imaging**	**Optrode Technology**
Nature	Retrospective	Chronic	Chronic	Chronic
Sensitivity	High	Low	Low below 500 µm	High
Specificity	High	Only site specific	High	High
Throughput	Low	Low	Low	High
Data acquisition speed	Very slow (days)	Fast (15-20 mins)	Fast (few mins)	Very high (40 – 60 sec)
Simultaneous spike data recording capability	No	No	No	Yes
Development stage	Established	Established	Both old and new technologies present	Early stage
Cost	Low	Moderate	Low-Moderate	High

proof-of-concept, design, fabrication and verification of a novel bi-directional optrode for real time tissue spectroscopy. This pilot study demonstrates acquisition of *in vivo* optical spectroscopic data from rat's cerebral cortex, overcoming many early experimental challenges. The results indicate significant variation in optrode's optical power output post device implantation period, suggesting possible changes in tissue optical spectroscopic characteristics following a traumatic brain injury. However, the feasibility of the technique needs further investigation and extensive validation in animal models. The acquisition of more spectral information from the tissue with detailed quantification of recorded optical data is needed to provide more insight into how tissue spectral components can be directly linked down to known tissue responses. For future studies, additional animal work is necessary to validate the

ability of an optrode to detect morphological changes in the tissue micro-environment around an electrode and to correlate this with impedance spectroscopy. More histological studies are also needed to extensively study the histological changes associated with neural tissue, pre-and post a neural trauma. Once fully proven and developed, the proposed optrode platform can potentially surpass all state-of-art techniques for tissue assessment in determining the progression of glial scarring around the implants in real-time (**Table 6.2**).

References

[1] J. P. Donoghue, “Bridging the Brain to the World: A Perspective on Neural Interface Systems,” *Neuron*, vol. 60, no. 3. pp. 511–521, 2008.

[2] M. A. L. Nicolelis, “Brain-machine Interfaces to Restore Motor Function and Probe Neural Circuits,” *Nat. Rev. Neurosci.*, vol. 4, no. May, pp. 417–422, 2003.

[3] S. Suner, M. R. Fellows, C. Vargas-Irwin, G. K. Nakata, and J. P. Donoghue, “Reliability of signals from a chronically implanted, silicon-based electrode array in non-human primate primary motor cortex,” *IEEE Trans. Neural Syst. Rehabil. Eng.*, vol. 13, no. 4, pp. 524–541, 2005.

[4] X. Liu, D. B. McCreery, R. R. Carter, L. A. Bullara, T. G. H. Yuen, and W. F. Agnew, “Stability of the interface between neural tissue and chronically implanted intracortical microelectrodes,” *IEEE Trans. Rehabil. Eng.*, vol. 7, no. 3, pp. 315–326, 1999.

[5] W. M. Grill, S. E. Norman, and R. V. Bellamkonda, “Implanted Neural Interfaces: Biochallenges and Engineered Solutions,” *Annu. Rev. Biomed. Eng.*, vol. 11, no. 1, pp. 1–24, 2009.

[6] G. Perlin, “A fully-implantable integrated front-end for neural recording microsystems,” Ph.D. dissertation, University of Michigan, Ann Arbor, 2008.

[7] E. Merriam, “A Three-dimensional bidirectional interface for neural mapping,” Ph.D. dissertation, University of Michigan, Ann Arbor, 2010.

[8] P. R. Patel, H. Zhang, M. T. Robbins, J. B. Nofar, S. P. Marshall, M. J. Kobylarek, T. D. Y. Kozai, N. A. Kotov, and C. A. Chestek, “Chronic in vivo stability assessment of carbon fiber microelectrode arrays,” *J. Neural Eng.*, vol. 13, no. 6, p. 66002, 2016.

[9] T. D. Y. Kozai, N. B. Langhals, P. R. Patel, X. Deng, H. Zhang, K. L. Smith, J. Lahann, N. A. Kotov, and D. R. Kipke, “Ultrasmall implantable composite microelectrodes with bioactive surfaces for chronic neural interfaces.,” *Nat. Mater.*, vol. 11, no. 12, pp. 1065–73, 2012.

[10] J. P. Seymour and D. R. Kipke, “Fabrication of polymer neural probes with sub-cellular features for reduced tissue encapsulation,” *Annu. Int. Conf. IEEE Eng. Med. Biol. - Proc.*, vol. 1, pp. 4606–4609, Jan. 2006.

[11] J. E. Sanders and J. R. Rochefort, “Fibrous encapsulation of single polymer microfibers depends on their vertical dimension in subcutaneous tissue.,” *J. Biomed. Mater. Res. A*, vol. 67, no. 4, pp. 1181–1187, 2003.

[12] K. C. Cheung, P. Renaud, H. Tanila, and K. Djupsund, “Flexible polyimide

microelectrode array for in vivo recordings and current source density analysis," *Biosens. Bioelectron.*, vol. 22, no. 8, pp. 1783–1790, 2007.

[13] Y. T. Kim, R. W. Hitchcock, M. J. Bridge, and P. A. Tresco, "Chronic response of adult rat brain tissue to implants anchored to the skull," *Biomaterials*, vol. 25, no. 12, pp. 2229–2237, 2004.

[14] F. Wu, L. W. Tien, F. Chen, J. D. Berke, D. L. Kaplan, and E. Yoon, "Silk-backed structural optimization of high-density flexible intracortical neural probes," *J. Microelectromechanical Syst.*, vol. 24, no. 1, pp. 62–69, 2015.

[15] K. Kampasi, B. Gross, J. Seymour, F. Wu, E. Yoon, and G. Poe, "Biocompatibility of dissolvable silk fibroin in central nervous system," in *BMES Midwest Biomedical Engineering Conference*, 2014.

[16] B. D. Winslow and P. A. Tresco, "Quantitative analysis of the tissue response to chronically implanted microwire electrodes in rat cortex," *Biomaterials*, vol. 31, no. 7, pp. 1558–1567, Mar. 2010.

[17] R. Biran, D. C. Martin, and P. A. Tresco, "Neuronal cell loss accompanies the brain tissue response to chronically implanted silicon microelectrode arrays," *Exp. Neurol.*, vol. 195, no. 1, pp. 115–126, Sep. 2005.

[18] J. C. Williams, J. A. Hippensteel, J. Dilgen, W. Shain, and D. R. Kipke, "Complex impedance spectroscopy for monitoring tissue responses to inserted neural implants," *J. Neural Eng*, vol. 4, pp. 410–423, 2007.

[19] E. S. Kappenman and S. J. Luck, "The effects of electrode impedance on data quality and statistical significance in ERP recordings," *Psychophysiology*, vol. 47, no. 5, pp. 888–904, 2010.

[20] T. D. Y. Kozai, A. L. Vazquez, C. L. Weaver, S.-G. Kim, and X. T. Cui, "Two-Photon Microscopy Reveals Immediate Microglial Reaction To Implantation of Microelectrode Through Extension of Processes," *J. Neural Eng.*, vol. 9, no. 6, p. 66001, 2012.

[21] M. Oheim, E. Beaurepaire, E. Chaigneau, J. Mertz, and S. Charpak, "Two-photon microscopy in brain tissue: Parameters influencing the imaging depth," *J. Neurosci. Methods*, vol. 111, no. 1, pp. 29–37, 2001.

[22] F. Helmchen and W. Denk, "Deep tissue two-photon microscopy," *Nat. Methods*, vol. 2, no. 12, pp. 932–940, 2005.

[23] T. H. Chia and M. J. Levene, "Microprisms for in vivo multilayer cortical imaging.," *J. Neurophysiol.*, vol. 102, no. 2, pp. 1310–1314, 2009.

[24] B. L. McLaughlin, K. Kampasi, G. E. Perlin, J. Leblanc, A. K. H. Achyuta, P. Kumar, G. Cook, C. Segura, V. Mittal, and D. Kipke, "Bi-directional Optrode for

quantitative prediction of neural interface failure," in *International IEEE/EMBS Conference on Neural Engineering, NER*, 2013, pp. 915–918.

[25] S. L. Jacques, "Optical properties of biological tissues: a review.," *Phys. Med. Biol.*, vol. 58, no. 11, pp. R37-61, 2013.

[26] P. van der Z. ; M. E. ; D. T. Delpy, "Optical properties of brain tissue," *Proc. SPIE Phot. Migr. Imaging Random Media Tissues*, vol. 1888, pp. 454–465, 1993.

[27] A. J. Welch and M. J. C. Van Gemert, *Optical-thermal response of laser-irradiated tissue*. 2011.

[28] X. Wang, Y. Pang, G. Ku, X. Xie, G. Stoica, L. L. V Wang, J. Gamelin, A. Maurudis, A. Aguirre, F. Huang, P. Guo, L. L. V Wang, Q. Zhu, J. Xia, C. Huang, K. Maslov, M. a Anastasio, and L. L. V Wang, "Noninvasive laser-induced photoacoustic tomography for structural and functional in vivo imaging of the brain.," *Opt. Lett.*, vol. 38, no. 13, pp. 3140–3, 2013.

[29] B. W. Pogue and M. S. Patterson, "Review of tissue simulating phantoms for optical spectroscopy, imaging and dosimetry," *J. Biomed. Opt.*, vol. 11, no. 4, pp. 41102-41102–16, 2006.

[30] A. N. Yaroslavsky, P. C. Schulze, I. V Yaroslavsky, R. Schober, F. Ulrich, and H.-J. Schwarzmaier, "Optical properties of selected native and coagulated human brain tissues in vitro in the visible and near infrared spectral range," *Phys. Med. Biol.*, vol. 47, no. 12, p. 305, 2002.

[31] K. D. Wise, A. M. Sodagar, Y. Yao, M. N. Gulari, G. E. Perlin, and K. Najafi, "Microelectrodes, microelectronics, and implantable neural microsystems," *Proc. IEEE*, vol. 96, no. 7, pp. 1184–1202, Jul. 2008.

[32] L. Wang, S. L. Jacques, and L. Zheng, "MCML-Monte Carlo modeling of light transport in multi-layered tissues," *Comput. Methods Programs Biomed.*, vol. 47, no. 2, pp. 131–146, 1995.

[33] V. S. Polikov, P. A. Tresco, and W. M. Reichert, "Response of brain tissue to chronically implanted neural electrodes.," *J. Neurosci. Methods*, vol. 148, no. 1, pp. 1–18, Oct. 2005.

[34] Y. Wang, D. D. Rudym, A. Walsh, L. Abrahamsen, H. J. Kim, H. S. Kim, C. Kirker-Head, and D. L. Kaplan, "In vivo degradation of three-dimensional silk fibroin scaffolds," *Biomaterials*, vol. 29, no. 24–25, pp. 3415–3428, 2008.

[35] T. Kim, J. G. McCall, Y. H. Jung, X. Huang, E. R. Siuda, Y. Li, J. Song, Y. M. Song, H. A. Pao, R.-H. Kim, C. Lu, S. D. Lee, I.-S. Song, G. Shin, R. Al-Hasani, S. Kim, M. P. Tan, Y. Huang, F. G. Omenetto, J. A. Rogers, and M. R. Bruchas, "Injectable, Cellular-Scale Optoelectronics with Applications for Wireless Optogenetics," *Science (80-.).*, vol. 340, no. 6129, pp. 211–216, Apr. 2013.

Chapter 7

Conclusion and Future Direction

7.1 Summary

In this work, we present design solutions towards development of next-generation implantable Michigan probes. Our novel multicolor optoelectrode technology provides independent activation and/or inhibition of simultaneously monitored neurons by illuminating different wavelengths at a given stimulation site and synchronously stimulating multiple optical sites in various combinations. It also offers a compact design solution that can effectively stimulate and record neural spikes with less than 100 μV stimulation-locked transients on the recording channels while maintaining the optical and thermal design merits of an implantable neural optoelectrode.

In particular, in Chapter 3, we presented for the first time, a neural optoelectrode with multicolor stimulation capability at a single light port. We implemented the optical design using ILD chips, GRIN lenses and monolithically integrated waveguide mixers. We conducted in-depth optical analysis and thermal analysis of the single-shank optoelectrode with one waveguide light port and eight electrical recording sites. The optical efficiency and alignment tolerances of optical assembly were thoroughly simulated in Zemax to maximize optical system efficiency and achieve 10 to 3000 mW/mm^2 of irradiance at the light port. The Comsol

Multiphysics bio-heat model demonstrated safe device operation for up to several tens of seconds, which is more than adequate for optogenetic applications.

In Chapter 4 and 5, we implemented electrical shielding and grounding strategies to reduce the electro-magnetic interference noise within permissible levels of 30-100 μV, which is a major design challenge for opto-electronic devices with on-board light sources. We supported our results with lumped circuit model analysis in Cadence SPICE simulator, and *in vitro* and *in vivo* verification. In chapter 5, we showed the implementation of a compact, low-noise, system-level opto-electronic packaging for four-shank optoelectrodes. We demonstrated why ILD coupled GRIN designs are efficient and favorable for implantable optoelectrodes in terms of desired optical, thermal, noise characteristics. Using a combination of high-density extracellular recordings and precise multisite/multicolor closed-loop optical stimulation, we were able to achieve independent activation of two cell types in densely populated CA1 of hippocampus of awake mice. Our principal *in vivo* findings are as follows. 1) We were able to induce light-mediated spiking response in a group of pyramidal cells and PV interneurons with two different light colors at a precise spatial location. 2) We detected monosynaptic pyramidal-PV interneuron pairs with pyramidal cells making excitatory synapses with PV interneurons. 3) We also detected a potential inhibitory synapse from a PV interneuron to a pyramidal cell in a presumably closed loop circuit.

Finally, in chapter 6, we discussed failure mechanisms for implantable neural probes and presented potential techniques to mitigate *in vivo* tissue damage around implants. We provided a comparative assessment of currently available tools for

tissue damage assessment and also proposed a novel bi-directional optrode platform that can be used as an optical diagnostic readout for predicting the extent of tissue damage *in vivo.*

In conclusion, we presented technological advancements to enable engineering of next-generation of implantable neural interfaces. Our ILD-GRIN optoelectrode technology finally paves the way for "advanced optogenetics" which may provide first-time insights into understanding how different types of synapses or pathways interact within a local circuit to support brain computation. By offering multicolor photo-stimulation at same spatial location, independently and simultaneously, ILD-GRIN optoelectrodes allow precise spatial and temporal manipulation of spike timing in awake animals. This allows for generation of unique spatiotemporal activity patterns in intact brain, which are critical to moving forward with neural circuit dissection, a popular and critical avenue of systems neuroscience.

7.2 Future direction and challenges

The most fundamental impact of optogenetics, even on human health, does not arise from direct introduction of opsins into human tissue but rather from use as a research tool to obtain insights into complex tissue function. Advances in multi-opsin optogenetic experiments will help us to move toward a circuit-engineering approach, in which devastating symptoms of disease could be understood from specific spatiotemporal patterns of aberrant circuit activity relating to specific neuronal populations. The multicolor optoelectrode technology presented in this work can be expanded for various optogenetic circuit control applications that can combine a vast range of currently available opsins. The most obvious technology expansion being the

increase in the density of stimulation and recording sites per shank or increase in number of shanks of the optoelectrode. With ever-growing semiconductor industry, as the bare laser chips become available in more wavelengths (450 nm, 520 nm etc.) in near future; our technology can be extended to provide more than two wavelengths for a multi-opsin experiment. Multiple-shank probes with multi-optical/electrode sites can be fabricated easily using the same fabrication process flow. For more compact designs, the waveguide widths can be reduced to route more than one waveguide on the same shank with multiple emission points per shank. Waveguides could also be patterned over the interconnection lines to optimize shank space. To overcome packaging limitations for scaling beyond a certain channel number in two-dimension, innovative solutions to stack up two-dimensional assemblies vertically for design of waveguide arrays can also be explored. Integrating such high-density designs with higher power ILDs and/or enhancing the waveguide film characteristics can compensate for the propagation loss through thinner waveguides. Interconnection width and pitch can be decreased using electron-beam lithography techniques. These modifications will allow for narrower shank widths with more waveguide ports for every set of recording sites, and also provide sufficient waveguide light power for cell activation and/or silencing. The geometry and surface of waveguide apertures can be modified to create various light diffusion profiles for specific target applications. The light diffusion could be made more lambertian for local illumination or more directional to target deeper tissue depths. Packaging modifications can also include integration of multichannel custom-made bench driving or on-board ILD driving with wireless circuit control. On the neuroscience side, this technology can be

implemented widely to perform combinatorial neural interrogation experiments. One of the critical applications could be in memory analysis in hippocampus. The neural basis of memory is of key scientific and clinical importance, but it is yet unknown how memories are formed and maintained. By creating unique spatiotemporal spiking patterns using precise multicolor light delivery, our technology can help to find the importance of precise spike timing for information processing in the brain. The ultimate aim is to solve critical questions in cognitive neuroscience, allowing researchers to finally understand mysteries of neurological disorders like Alzheimer's and Parkinson's.

Optogenetic tools have changed the way neuroscience is conducted leading to rapid advances in the associated enabling technologies. Yet, much work remains to take neuroscience forward. Major areas of optogenetic tool advancement include advancing the genomic expansion of optogenetic tools for multi-opsin experiments, refining the molecular engineering for optimized functionality and developing light and genetic targeting strategies for various biological systems and animal models. Engineering optogenetic light sensors for higher quantum efficiency and greater light sensitivity would be of substantial value because it would enable the use of lower irradiances for targeting a given tissue volume or depth. Engineering these known or new tools for narrowed and shifted action spectra would enable cleaner separation of control channels with less crosstalk. Technological advance towards high-speed targets and causal control of intact neural circuit function also needs to be sustained. There is a pressing need for improved scale, density and specificity to make significant breakthroughs in the field. Continuous and parallel advancements in field

of micro-/nano-technologies and microsystems packaging will help to inch closer towards this goal. Expansion of tools to contain combination of modalities like electrical, optical and neurochemical sensing can also provide more insights into circuit function. Altogether, these requisites will keep pushing the discovery of molecular biology and technology alike in coming years. In parallel, consistent efforts need to be realized towards the development of reliable and scalable neurotechnology for long-term research and clinical use. Novel and scalable probe designs with modified architecture, better probe geometries, flexible biocompatible materials could be explored to move forward in this direction.

Appendix A

Grating designs for light coupling from different source types

Circular grating design

When a circular grating design is coupled to 465 nm fiber source (in perpendicular plane), 1D simulation results indicate 16% total coupling efficiency from the perpendicular source to the lab waveguide. However, the same design yields very low efficiency (<1%) for lambertian sources like LEDs. Design equation used: $-\frac{\eta_o}{\lambda}\sin\theta + \frac{\eta_w}{\lambda} = \frac{1}{\Lambda}$, where η_o= 1.45, η_w= 2, λ = wavelength, Λ = Grating period.

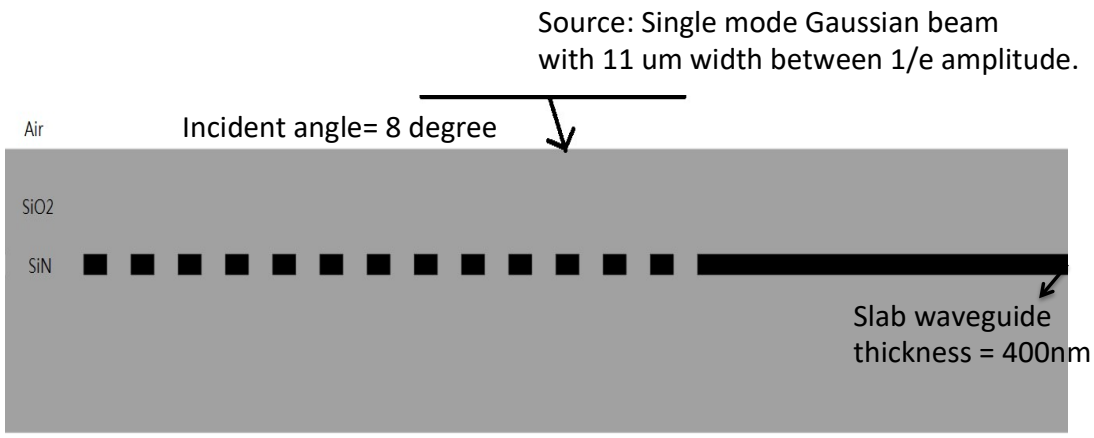

Figure A-1. Cross-section of circular grating coupled to a slab waveguide.

Circular scaled grating design

A circular grating design with scaled grating periods was also tested for coupling with 465 nm LEDs. Equation of dipole light source: $\cos\left(\text{atan}\left(\frac{x}{L_h}\right)\right) * e^{-i*k(x)*x}$; $k(x) = 2\pi\frac{c}{\lambda} * \sin(\text{atan}(\frac{x}{L_h}))$. Using equation:

$-\frac{\eta_o}{\lambda}\sin\theta + \frac{\eta_w}{\lambda} = \frac{1}{\Lambda}, n_o = 1.45, n_w = 2, \lambda = 465nm$

If r is the distance from center of the grating, then defining grating structure (pseudocode): Simulation lattice dimension: $L_h = 6.4\ \mu m,\ L_w = 50\ \mu m,\ n_{cladding} = 1.45,\ n_{waveguide} = 2.0, Cladding\ thickness = 2\ \mu m, Waveguide\ thickness = 400\ nm;\ r(0) = 0.29\ Make\ block\ size$ $\frac{1}{2*(3.44086 \quad .11828*\sin(\text{atan}(\frac{r(n)}{L_h})))}$.

$$r(n+1) = r(n) + \frac{1}{3.44086 - 3.11828 * \sin(\text{atan}(\frac{r(n)}{L_h}))}$$

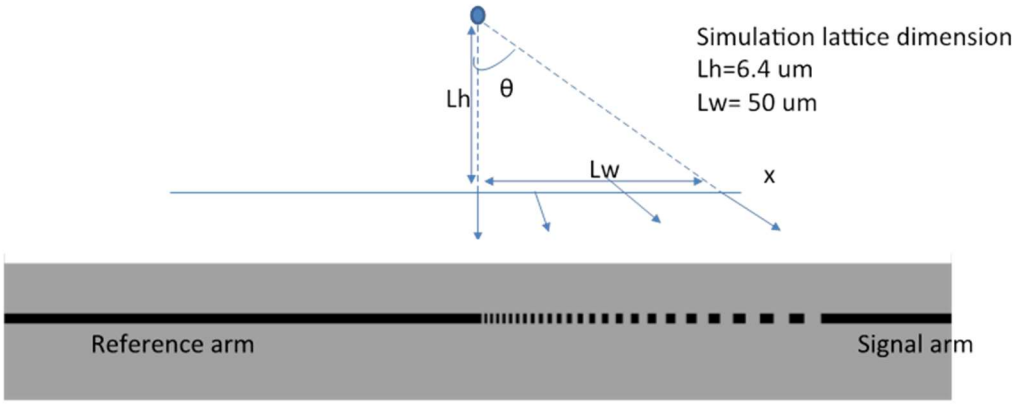

Figure A-2. Cross-section of circular scaled grating coupled to a slab waveguide.

The modified grating design yielded almost no improvement when coupling to LEDs (simulated θ=67.5°). The same design yielded 4.6% efficiency when coupled to a 465nm laser source (simulated θ=20°).

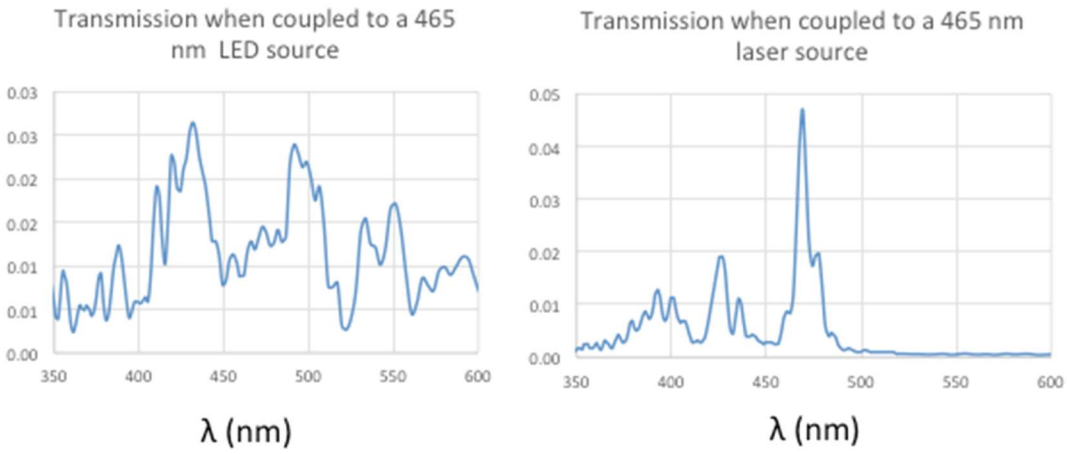

Figure A-3. Transmission spectra of the slab waveguide output when an LED and an LD source are coupled to a circular scaled grating.

Radial grating design with Bragg reflector

Radial grating design

Etch depth h ~400nm; Slab thickness >4um (or same with the waveguide size); Cladding thickness >2um; Grating radius = LED distance * tan (70).

$$\frac{m\lambda}{d} = cos\emptyset(n_{slab}sin\theta_c + n_{mediam}\theta_i) \ldots\ldots\ldots (1)$$

where θ_c is the critical angle of total internal reflection at the interface of cladding SiO2 and N4Si3. n_{mediam}=1 (air), m is diffraction order, here we use m=1. d is the periods length of grating and λ=wavelength at 635nm.

$$\theta_c = sin^{-1}\left(\frac{n_{cladding}}{n_{slab}}\right) \ldots\ldots\ldots\ldots (2)$$

Combine (1) and (2), for radial grating θ_i= 0; $\frac{\lambda}{d} = n_{cladding} * cos\emptyset$

$$= 1.45 * cos\emptyset$$

Bragg reflector design

$$\mathrm{d1} = \frac{\lambda}{4n_{slab}} = 79.375\ (\mathrm{nm}) \quad \text{and} \quad \mathrm{d2} = \frac{\lambda}{4n_{air}} = 158.75\ (\mathrm{nm});$$ d1 is the thickness of N4Si3 layer and d2 is the thickness of air layer. For Normal incident

$$\text{Reflectivity} = 1 - 4\left(\frac{n_{air}}{n_{cladding}}\right)^{2p}\left(\frac{n_{air}}{{n_{cladding}}^2}\right) = 1 - (0.5)^{2p}$$

With grating periods number p=5, reflectivity is ~99.9%

Spot concentration taper

Since the mechanism of taper is simply the total internal reflection, the smother the convergence angle lead to a better transmission.

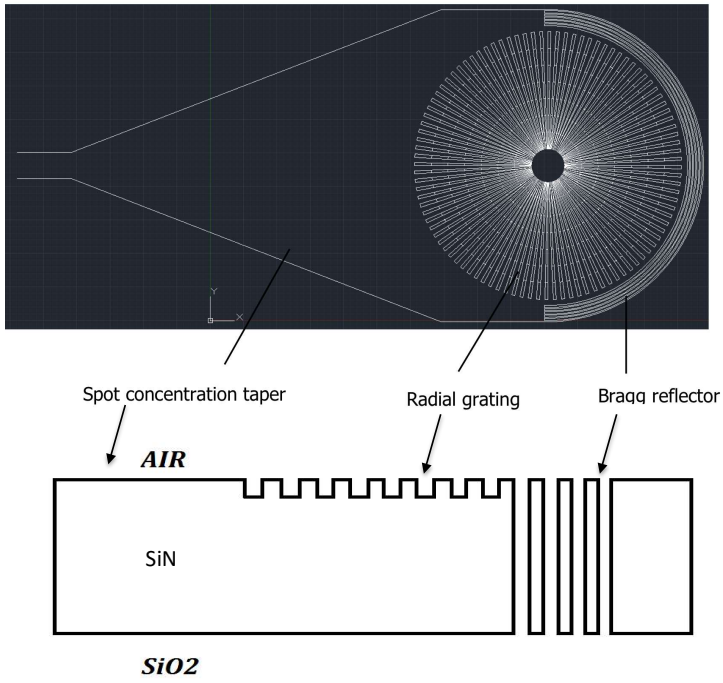

Figure A-4. Top view and side view of a radial grating design with Bragg reflector to couple light from a light source.

FDTD simulation results show 0.45% optical efficiency for an LED source (simulated θ=67.5^{o}) and 30-50% optical efficiency for a laser source (simulated θ=30^{o}).

Appendix B

Electrophysiological procedures for acute animals

All animal handling procedures were approved by the New York University Animal Care and Facilities committee, and all animal handling procedures were carried out in accordance with the approved guidelines.

Four male mice (26-42 g, 6-18-month-old) were used in this study. To express ChR2 and eArch3 in pyramidal cells, two mice (B6.Cg-Tg(Camk2a-cre)T29-1Stl/J, Jackson labs #005359) were injected with a Cre-dependent virus mix (AAV5-EF1a-DIO-hChR2(H134R)-EYFP and AAV5-EF1a-DIO-eArch3.0-EYFP, University of North Carolina viral core; viral titer estimated at 4x1012 IU/ml). During virus injection, a 0.2 mm craniotomy was made at PA -1.6/ML 1.1, and 7 injections of 55 nl were made at 0.2 mm intervals from DV, 1.8 mm to 0.6 mm, to target the right dorsal hippocampus6. One PV::ChR2 mouse (offspring of B6;129P2-Pvalbtm2.1(cre)Arbr/J female, Jackson Labs #008069; cross-bred with B6;129S-Gt(ROSA)26Sortm32(CAG-COP4*H134R/EYFP)Hze/J male, Jackson labs #012569, Ai32) expressed ChR2 in parvalbumin-immunoreactive (PV) cells. Finally, one wild-type mouse (control; C57L/6J, Jackson Labs) was used.

Five weeks after virus injection, the animals were anesthetized (urethane, 1.5 g/kg) and prepared for acute recordings46. The waveguide probe was inserted at PA -1.6/ML 1.1 and gradually lowered to a depth of 600 μm. Subsequent probe

movements were done in 50 or 100 μm increments over 15 min intervals until the CA1 pyramidal cell layer was approached, recognized by the appearance of multiple high-amplitude units and spontaneous ripple events6,46,47. Extracellular activity was filtered (0.3-10,000 Hz), amplified (400x; RHA2132, Intan), digitized (14 bit, 20 kHz digitization; KJE-1001, AmpliPex), and continuously stored on disk. For offline analysis, spike waveforms were extracted from the wide-band recorded signals and sorted into individual units46. Briefly, waveforms were linearly detrended, projected onto a common basis obtained by principal component analysis of the data, and sorted automatically followed by manual adjustment. Only well-isolated units (amplitude >50 μV; L-ratio <0.05; interspike interval index <0.2) were used. Subsequently each unit was tagged as excitatory/inhibitory [based on peaks/troughs in the short-time (±5 ms) pairwise cross correlation; $P < 0.001$, convolution test] and/or classified as putative PYR or INT (based on a Gaussian-mixture model; $P < 0.05$;46). We recorded a total of 77 well isolated cells from CA1 of 4 anesthetized mice in 5 sessions. Of these, 64 were PYR and 13 were INT.

Baseline neuronal activity was recorded for at least 15 minutes, followed by photo stimulation (405 nm: 50 ms light pulses; 635 nm: 200 ms pulses) via a programmable DSP (25 kHz; RX8, Tucker-Davis Technologies) driving a custom-made multi-channel current source24. Five current levels were used per ILD, spanning the range from threshold to maximal operating level (405 nm: 15-35 mA; 635 nm: 30-45 mA). Following photo stimulation, a second baseline period was recorded before the probe was moved to another target.

Appendix C

ILD driver specifications for ILD-GRIN optoelectrodes

Critical design requirements:

1. Voltage range on driver output channels: 0-7V

2. Current range on driver output channels: 0-60 mA

3. Constant current operating mode with at least 0.01mA current resolution control on all channels.

4. Common cathode driver configuration for all channels.

5. Independent control on all 8 output channels with 0-60 mA current on each channel.

Recommended design requirements:

1. Highly stable with low noise: from 100nA-1uA (RMS @ 0.1Hz to 10Hz).

2. Soft start protection with a slow start period of atleast 10us

3. ESD/relay switch protection on all ports.

Additional design requirements (if building a custom-made multichannel laser driver):

1. Linear transfer function between input modulating voltage to output current on all output channels, independent of the battery/supply voltage.

2. Battery supply of not more than 7-10V.

3. Device interlock/complete shutdown switch.

4. 50 μs rise time on all channels with capability to drive arbitrary waveforms (pulse, sine etc.) up to 0.1 Hz-1kHz frequency range. The input-output delay for a square pulse input should not be more than 100 μs (fast switching requirement as per optogenetic applications). This means:

Time stamp of pulse at output port minus time stamp of pulse at input port = Pulse delay from input to output port (50 μs) + pulse rise time (50 μs).

Appendix D

Electrophysiological procedures for awake animals

All animal procedures were approved by the New York University Animal care and Facilities committee. PV-Cre mice (B6;129P2-Pvalbtm1(cre)Arbr/J ; JAX Labs, Maine) were injected in dorsal CA1 (coordinate, in mm from bregma: -1.75 posterior, 2.0 mm left) with two AAVs, encoding Cre dependent ChrimsonR (AAV5-hSyn-FLEX-ChrimsonR-tdTomato) and CaMKII promoter driven ChR2 (AAV5-CaMKIIa-hChR2(H134R)-EYFP), resulting in expression of ChrimsonR in PV+ interneurons and ChR2 in pyramidal neurons (Viruses were sourced from the University of North Carolina Vector Core[61]). Animals were additionally implanted with a titanium head plate[62] and stainless steel ground wire places above the cerebellum. Mice were habituated to head fixation over the course of 1 week. After habituation, mice were head-fixed, and the electrode was lowered to dorsal CA1. Baseline recording was obtained, after which stimulation with 405 and 635 nm light was made at different intensities and durations. Neural data was acquired at 20 kHz using an Intan RHD2000 recording system. Spikes were detected and automatically sorted using the Kilosort algorithm[63] followed by manual curation using Klusters[64]. Analysis was performed in MATLAB using custom scripts.

Appendix E

Immunohistology protocol

Following completion of experiments, the animals are transcardially perfused with 4% paraformaldehyde in 1xPBS. Following perfusion, the brain is extracted with probes intact and then soaked in paraformaldehyde for an additional 24-48 hours. After this period, the tissue sample is sectioned transversely into 20 μm thick slices on a cryostat. Each slice is then circled with a PAP pen to create a hydrophobic barrier, reducing the need for more reagents and to minimize spills. Slices are then rinsed with 1xPBS for 10 minutes and then blocked with 10% goat serum for one hour at room temperature. Next, samples are incubated with primary antibody in 0.3% Triton X-100 and 3% goat serum in 1xPBS overnight in a covered chamber. The next day, the slices undergo three 10-minute washes with 1xPBS. Slices are then incubated with secondary antibody (diluted according to manufacturer's recommendations) in 0.2% Triton and 5% goat or bovine serum in 1xPBS at room temperature for two hours. After two hours, the samples are washed twice with 1xPBS with each wash lasting 10 minutes. To counterstain for cell bodies, Hoechst 33342 is diluted 1:500 in 1xPBS and applied for 5 minutes. This is followed by two more 1xPBS washes, each at 10 minutes. Samples are then mounted on slides and cover slipped using Prolong Gold. For quantification of spatial signal intensity, digital images were collected using a Olympus DP-71 digital camera (Roper

Scientific; Trenton, NJ) attached to a Nikon E800 microscope (at Microscopy and Image Analysis Laboratory (MIL), University of Michigan) using Image Pro 4.5 software (Media Cybernetics; Silver Spring, MD). The study presented in Chapter 6 was imaged with a Confocal Microscope (Leica Inverted SP5X Confocal Microscope with 2-Photon FLIM) under 40x magnification. A list of antibodies used, their source, and targeted cell type is listed in **Table 6.1**.